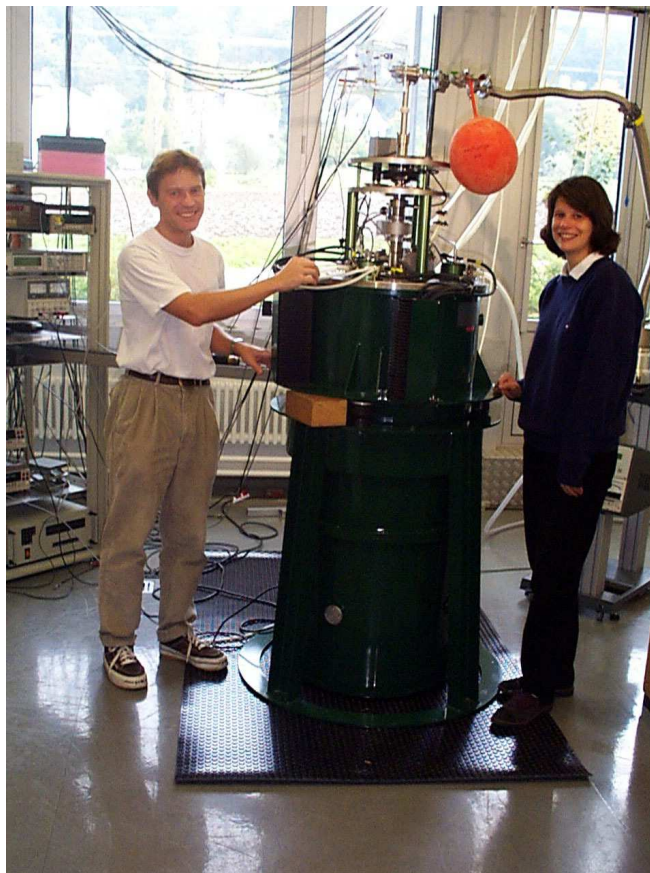




WISSENSCHAFTLICHER JAHRESBERICHT April 1999 - April 2000



PHYSIK-INSTITUT
DER UNIVERSITÄT ZÜRICH



WISSENSCHAFTLICHER JAHRESBERICHT
April 1999 - April 2000

The picture on the cover shows Susanne Zech-Döttinger and Andreas Schilling of the Superconductivity and Magnetism group at the 8 T cryo-magnet

Sekretariat	01 635 5721	secret@physik.unizh.ch
Prof. C. Amsler	01 635 5784 022 767 2914	amsler@cern.ch
Prof. R. Engfer	01 635 5720	engfer@physik.unizh.ch
Prof. H.-W. Fink	01 635 5801	fink@physik.unizh.ch
Prof. H. Keller	01 635 5748	keller@physik.unizh.ch
Prof. P.F. Meier	01 635 4016	meier@physik.unizh.ch
Prof. J. Osterwalder	01 635 5827	osterwal@physik.unizh.ch
Prof. U.D. Straumann	01 635 5768	strauman@physik.unizh.ch
Prof. P. Truöl	01 635 5777	truoel@physik.unizh.ch

Begleitwort

Mit seinen sieben Professuren deckt das Physik-Institut ein breites, national und international vernetztes Forschungsspektrum ab, das von den Eigenschaften biologischer Makromoleküle bis zu jenen der elementaren Bestandteile des Universums in seiner Frühphase reicht. In den beiden etwa gleich starken Hauptbereichen, Physik der kondensierten Materie und Physik fundamentaler Systeme, finden sich Gruppen in der Bio-, der Oberflächen-, der Festkörper- und der Elementarteilchenphysik.

Zwei langjährige Angehörige des Physik-Instituts, die Professoren Detlef Brinkmann und Walter Kündig sind 1999 zurückgetreten. Mit ihren Nachfolgern, den Professoren Hans-Werner Fink und Ulrich Straumann zieht einerseits das neue, interdisziplinäre Forschungsgebiet Biophysik in das Institut ein bzw. wird andererseits das Engagement in der Teilchenphysik bei höchsten Energien deutlich verstärkt.

In Prof. Brinkmann's Labor wurden verschiedene, u.a. tomographische Methoden der nuklearen, magnetischen Resonanz (NMR) angewendet um elektronische Eigenschaften speziell von solchen Substanzen zu untersuchen, von denen man sich vielfältige technische Anwendung verspricht wie Superionenleiter und Hochtemperatursupraleiter. Ein tieferes, auch theoretisches Verständnis der letzteren Substanzen zu finden, bleibt ein aktives, mit diversen selbstentwickelten Methoden und Instrumenten konkurrenzloser Empfindlichkeit vorangebrachtes Thema der Forschungsgruppe von Prof. H. Keller.

Die Funktionen biologischer Systeme besser zu verstehen, z.B. den Elektronentransfer in DNA Molekülen ist das Ziel der im Aufbau befindlichen Biophysik-Gruppe von Prof. H.-W. Fink, zu deren Gunsten die NMR-Aktivitäten aufgegeben wurden. Die von Prof. Fink neu entwickelte, weltweit noch einzigartige Messtechnik der Holographie mit langsamen Elektronen erlaubt es Biomoleküle mit hoher räumlicher Auflösung abzubilden. Mit dieser Methode konnte dann gezeigt werden, dass DNA Moleküle den elektrischen Strom leiten, sich also physikalisch gesehen wie quasi eindimensionale Quantendrähte mit speziellen Eigenschaften bezüglich des Transports von Elektronen verhalten. Eines der zukünftigen Ziele kann daher sein, solche molekularen Drähte aus Biopolymeren für die Herstellung von elektrischen Netzwerken, möglicherweise auch mit Schaltfunktionen, zu nutzen.

In Prof. J. Osterwalder's Gruppe werden insbesondere physikalische und chemische Eigenschaften von nanostrukturierten Oberflächen untersucht. Aufklärung der elektronischen Struktur von Grenzschichten, z.B. bei Metall-Isolator-Metall Tunnelkontakten kann bei der Evaluation neuer Konzepte für Magnetspeicher und Spin-Computer eine grosse Rolle spielen.

Die in dem Bereich der Physik der kondensierten Materie arbeitenden Gruppen werden häufig unterstützt durch die theoretischen Modellrechnungen der Gruppe von Prof. P.F. Meier, die ihr Knowhow in der computergestützten Physik auch Instituten der medizinischen Fakultät und anderen ausseruniversitären Interessenten zur Verfügung stellt.

Gestützt durch den hohen technischen Standard der Werkstätten können die an den europäischen Beschleunigerzentren CERN, Genf (Profs. C. Amsler und U. Straumann) und DESY, Hamburg (Profs. U. Straumann und P. Truöl) arbeitenden Teilchenphysikgruppen technologisch anspruchsvolle Instrumententeile entwickeln und herstellen, was sie zu geschätzten Partnern in den internationalen Kollaborationen macht. Die zunehmende Strahlenergie und -intensität erlaubt es die Struktur der Materie und ihrer Bausteine mit immer besserer räumlicher Auflösung zu untersuchen, und damit auch ihre Entwicklung bis zu immer früheren Zeiten hin zurückzuverfolgen. Dies bedingt allerdings auch eine zunehmende Komplexität der Instrumente, deren Anforderungen bezüglich Geschwindigkeit der Datenaufnahme, Datenmenge und -übertragungsdichte, Integrationsdichte der elektronischen Komponenten, mechanische Konstruktion etc. jene erhältlicher kommerzieller Systeme in der Regel weit überschrei-

ten, und deren Herstellung und Betrieb eigentlichen Pioniercharakter aufweist.

Mit Präzisionsexperimenten bei niederen Energien am PSI, Villigen (Prof. R. Engfer), deren besonderes Ziel es ist, den Gültigkeitsbereich fundamentaler Symmetrieeigenschaften und Erhaltungssätze einzugrenzen, wird das Messprogramm bei höchsten Energien ideal ergänzt. Prof. Kündig's Aktivitäten sind mit Ausnahme des Präzisionsexperiments zur Messung der Gravitationskonstanten abgeschlossen. Letzteres wird unter Prof. Straumann's Leitung weitergeführt.

Der wissenschaftliche Jahresbericht¹ ist in englischer Sprache abgefasst. Dies erleichtert die Kommunikation mit den Kollegen, mit denen wir in internationalen Kollaborationen zusammenarbeiten, und erlaubt es, Teile dieses Berichts den forschungsfördernden Instanzen und ihren Gutachtern als Rechenschaftsbericht vorzulegen.

Zürich, im April 2000

Prof. Dr. Peter Truöl

A handwritten signature in black ink, reading "P. Truöl". The signature is written in a cursive style with a long horizontal stroke at the top.

¹Der Jahresbericht ist auch über das Internet einsehbar: <http://www.physik.unizh.ch/jb/>

Contents

Physics of Fundamental Interactions and Particles	1
1 Measurement of the Gravitational Constant G	1
2 Measurement of the Neutrino Magnetic Moment at the Bugey Nuclear Reactor	4
3 Search for μ-e Conversion with SINDRUM II	7
3.1 Search for conversion on gold: final result from 1997 run	8
3.2 Search for conversion on lead: first results from 1998 run	9
3.3 Results from 1999	9
3.4 Intentions for 2000: gold versus titanium	11
4 Rare Kaon Decays	12
5 Meson Spectroscopy at LEAR with the Crystal Barrel	15
5.1 Proton-antiproton annihilation into 6γ and 7γ	15
5.2 Antiproton-deuteron annihilation into ΛK^0 and $\Sigma^0 K^0$	16
6 Production and Spectroscopy of Antihydrogen	19
6.1 Production of antihydrogen	19
6.2 Annihilation detector	20
6.2.1 Silicon microstrip detector	21
6.2.2 CsI Crystals	22
6.2.3 Electronics	23
7 Particle Physics at DESY/HERA (H1)	25
7.1 Electron proton collisions at 300 GeV center of mass energy	25
7.2 Summary of activities	26
7.3 Construction of the new CIP	27
7.3.1 Mechanics	27
7.3.2 Electronics	28
7.4 Results from recent analyses	29
7.4.1 Determination of the gluon density and the strong coupling constant α_s	29
7.4.2 Photo- and electroproduction of charm quarks	33
8 Particle Physics at DESY/HERA (HERA-B)	38
8.1 Microstrip gas chamber development for the inner tracker	38
8.1.1 The status of the inner tracker	38
8.1.2 MSGC tests at PSI	40
8.2 Status of the HERA-B Experiment	41
8.2.1 Comparison with other B projects	41
8.2.2 The detector	42
8.2.3 The trigger system	43

9	High-precision CP-violation Physics at LHCb	45
9.1	CP – Violation and Physics of <i>B</i> Mesons	45
9.1.1	CP violation within the standard model and beyond	45
9.1.2	Present experimental activities	46
9.1.3	Second generation <i>B</i> physics program	47
9.2	The design of a <i>B</i> experiment at LHC	48
9.3	<i>B</i> physics at LHC	50
9.4	The inner tracking detector of LHCb	51
9.4.1	Preparatory studies for the HERA-B inner tracking	52
9.4.2	Extended investigations for LHCb	53
9.4.3	Triple GEM	53
9.4.4	Triple GEM operation in high intensity hadronic beams	55
9.4.5	Conclusions and outlook	56
10	Particle Physics at LHC/CMS	59
10.1	Lorentz-angle in irradiated silicon	59
10.2	Sensor developments	60
	 Condensed Matter Physics	 63
11	Superconductivity and Magnetism	63
11.1	Introduction	63
11.2	Studies of oxygen isotope effects	63
11.2.1	Oxygen isotope effects in manganites	63
11.2.2	Oxygen isotope effects in cuprates	65
11.3	NMR/NQR studies of charge fluctuations in cuprates	69
11.4	Detection of small thermal effects in transition-metal oxides	70
11.4.1	Lower critical point of the vortex-lattice melting line in $\text{YBa}_2\text{Cu}_3\text{O}_{7-\delta}$	71
11.4.2	Investigations on other transition-metal oxides	71
11.5	Critical phenomena in the cuprates	72
11.6	Studies of superconductors with low-energy muons	73
11.7	Medical engineering	74
12	Surface Physics	77
12.1	Surface states on vicinal Cu(111) surfaces	78
12.2	Surface states and surface phonons: H/Mo(110)	79
12.3	Monolayer hexagonal boron nitride film on Ni(111): Thin film geometries from substrate photoelectron diffraction	80
12.4	Influence of an atomic grating on a Fermi surface	81
12.5	Towards well defined metal-insulator-metal junctions	82
12.6	Electronic structure of K doped C_{60} monolayers on Ag(100)	83
12.7	Near-node photoelectron holography	84
12.8	Angle-scanned two-photon photoemission on Cu(111)	84
12.9	Spin-resolved Fermi surface mapping	86
13	Physics of Biological Systems	88

14 Computer Assisted Physics	90
14.1 Electronic structure of high- T_c materials: hyperfine interactions	90
14.2 Electronic structure of high- T_c materials: influence of dopants	92
14.3 Time series analysis of sleep EEG	93
Infrastructure and Publications	96
15 Mechanical Workshop	96
16 Electronics	98
17 Publications	99
17.1 Research group of Prof. C. Amsler	99
17.2 Research group of Prof. R. Engfer	101
17.3 Research group of Prof. H. Keller	101
17.4 Research group of Prof. P. F. Meier	108
17.5 Research group of Prof. J. Osterwalder	109
17.6 Research group of Prof. U. Straumann	112
17.7 Research group of Prof. P. Truöl	113

1 Measurement of the Gravitational Constant G

S. Schlamminger, E. Holzschuh, and W. Kündig

The gravitational constant G is defined by Newton's law of gravity. Although known for a long time, it is still the least accurately measured fundamental constant of nature. In 1987, the CODATA² committee recommended a value with an uncertainty of 128 ppm [1], largely based on the measurement of Luther and Towler [2]. In the meantime some new measurements have been published with rather discrepant results and recently, the same committee has increased the uncertainty for G to 1500 ppm [3]. There is clearly a need for more accurate and reliable measurements.

The goal of our experiment is a measurement of G with an uncertainty of order 10 ppm. The experiment uses a beam balance to measure gravitational forces and has become feasible thanks to recent progress in the construction of beam balances with extremely high sensitivity. The principle of the experiment will be explained below.

All major parts of the experiment are set up and are functioning. A first result for G with an uncertainty of 230 ppm has been published [4]. A detailed description of the experiment may be found in the dissertation of F. Nolting [5], who obtained a slightly improved value,

$$G = (6.6749 \pm 0.0014) \times 10^{-11} \text{ m}^3\text{kg}^{-1}\text{s}^{-2} \quad (\text{relative uncertainty } 220 \text{ ppm}).$$

These early results were completely dominated by systematic uncertainties.

During the past year we were mainly occupied with upgrades and improvements of the experiment. These improvements, which will be briefly described in this annual report, were primarily aiming at an increased stability of the experiment. Progress has also been made in achieving higher resolution and lower noise of the balance.

The experiment is located in a 4.8 m deep pit at the Paul Scherrer Institute. A schematic view is shown in Fig. 1.1. The essential components of the set-up are a single-pan beam balance, two test masses and two large field masses. The test masses (1 kg each) are suspended with thin tungsten wires and alternately connected to the balance. The difference of their weights is measured with high precision and taken as the signal. The balance and the test

²The Committee on Data for Science and Technology of the International Council of Scientific Unions

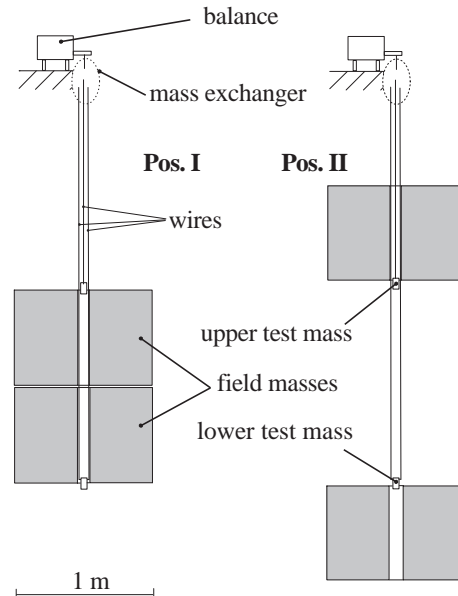


Figure 1.1: *Schematic view of the experiment to measure the gravitational constant. See main text for explanation.*

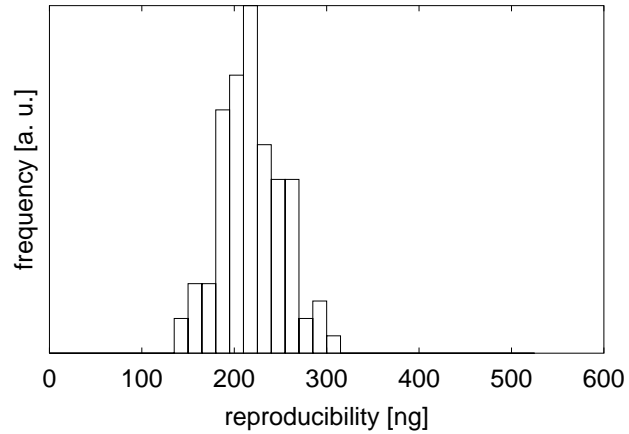


Figure 1.2: *Histogram of the reproducibility of the balance.*

masses are inside a vacuum system. The field masses are cylindrical in shape and have a central bore such that the test masses can pass through. By moving the field masses between the two positions shown, their gravitational force on the test masses changes the signal. From the difference of the signal for the two states and from known values for the masses, densities, and distances, the gravitational constant G can be computed.

There are several features which make this measurement principle very promising. The test masses are placed at positions where the gravitational force of the field masses has local extrema. Therefore the relative positions of the masses are quite uncritical. The value of G is computed from a double difference and many disturbing forces and drift effects should cancel in the result. The field masses are vessels made of stainless steel with a volume of 500 l each. Presently, they are filled with mercury because of its high density. Previously, a measurement with water filled vessels has also been performed [4].

The balance was supplied by Mettler Toledo. The commercial version has a large measuring range, unnecessary for our purpose. To increase the resolution and to reduce noise, the range was reduced to a value of 4 g. The replacement of some mechanical parts has been mentioned in the last year's annual report. Various modifications of the internal software of the balance were necessary mainly because the balance was designed for a resolution of 1 μ g, much too coarse for our experiment.

The present performance of the balance is illustrated in Fig.1.2. Shown is a histogram of the reproducibility which is defined here as the standard deviation of 22 measured test mass differences. The measuring time for one difference, including two exchanges of the test masses, is 11 min. The average value is 220 ng.

The weights of the test masses are measured alternately by connecting one mass at a time to the balance. A special mechanical device is used being labeled mass exchanger in Fig.1.1. During the past year we have redesigned and partly rebuilt this device in order to minimize the variations in the total load on the balance during the exchange of the test masses. Load changes may result in mechanical stress energy stored in the structure of the balance which will be released subsequently on a long time scale leading to additional noise. The new device was installed very recently. A first test indicates that we can exchange the 1 kg test masses while keeping the load change on the balance below 0.1 g.

The balance is affected by changes of the temperature, causing drifts of the balance's reading. To a large part this effect can be attributed to a drift of the zero point. The calibration of the balance changes little with temperature. Originally, it was therefore believed that temperature induced drifts would cancel in the double difference. However, we had to conclude that this is not the case with the required precision. For this reason an elaborate

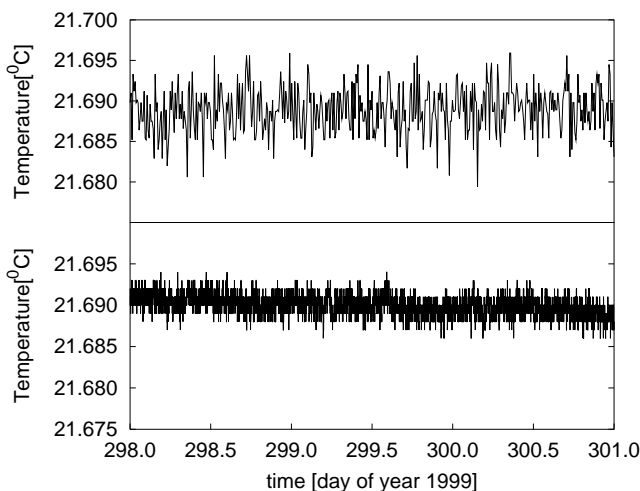


Figure 1.3: *Temperature in the thermally isolated box as measured with two independent thermometers.*

temperature stabilization was installed in 1999.

The system consists of three stages. A new air-conditioning was installed in the barrack housing the balance and the electronics. The cooling power is measured and continuously controlled. Typically, the temperature in the barrack is constant to within 0.1 K. The balance is located in a vacuum chamber which is surrounded by a thermally isolated wooden box. The temperature inside the box is controlled by a second air-conditioner. The temperature sensor for the controller was made of platinum wire wound around the chamber. It averages in space but has a fast response in time. The stability of the temperature inside the box is illustrated in Fig. 1.3 showing measurements with two independent thermometers. The last stage is passive. It is simply a heavy copper case housing the balance inside the vacuum chamber. The case acts like a low-pass filter with a time constant of several days thus averaging fluctuations of the vacuum chamber's temperature. The complete system requires at least a week to reach equilibrium. We have therefore at present no long-term measurements of the balance's temperature but are confident that we can reach a stability of order one milli-Kelvin.

There might be external influences to the experiment which are beyond our control. Tilt of the ground may be an example. We have therefore installed highly sensitive tilt meters with a resolution of $0.1\mu\text{rad}$ (0.02arc seconds). We have seen some effects, but so far these seem to have been induced by a changing temperature.

We thank the PSI for its hospitality and Mettler Toledo for the precision balance and the calibration of various standard weights. We are grateful to metrotec engineering for the help modifying and tuning the balance. The experiment was supported by the Swiss National Science Foundation, the Dr. Tomalla Foundation, and the Scientific Research Foundation of the University of Zürich.

References

- [1] E.R. Cohen and B.N. Taylor, Rev. Mod. Phys. 59, 1121 (1987).
- [2] G.G. Luther and W.R. Towler, Phys. Rev. Lett. 48, 121 (1982).
- [3] R.J. Mohr and B.N. Taylor, Rev. Mod. Phys. 72, No.2 (2000).
- [4] J. Schurr, F. Nolting, and W. Kündig, Phys. Rev. Lett. 80, 1142 (1998).
- [5] F. Nolting, Dissertation, Uni. Zürich 1998.

2 Measurement of the Neutrino Magnetic Moment at the Bugey Nuclear Reactor

C. Amsler, M. Heinzemann, O. Link and H. Pruyss

in collaboration with:

Institut des Sciences Nucléaires (Grenoble), Université de Neuchâtel, Università di Padova

(MUNU Collaboration)

The MUNU experiment is studying $\bar{\nu}_e e^-$ elastic scattering at the Bugey nuclear power plant by detecting the recoil electron in a CF_4 time projection chamber (TPC), in which both the angle and the energy of the recoil electron are measured. The typical electron energy is 1 MeV or smaller. The TPC is surrounded by an anticompton shield (AC) made of liquid scintillator. The aim of the project is to measure the neutrino magnetic moment with a sensitivity of $3 \times 10^{-11} \mu_B$. Previous laboratory experiments have led to an upper limit of $1.8 \times 10^{-10} \mu_B$ at 90% confidence level [1]). Details on the apparatus can be found in previous annual reports and in ref. [2].

In 1999 our group designed, installed and tested the general purpose trigger (based on the LRS 2366 ULM Gate Array) which we developed to remotely adjust the coincidences and timing for the various triggers (neutrinos, radioactive sources, muons) [3]. The triggers are more complicated than expected due to the fact that CF_4 was found to scintillate, so that the photomultipliers of the AC see the light from the avalanche in the TPC which traverses the acrylic vessel. This veto signal can be suppressed by using the long time delay between the photomultiplier signals and the arrival of the electron cloud at the anode.

In addition, the light of the avalanche from electrons generates asymmetric pulse heights in the forward and backward photomultipliers, since the anode plane is much closer to the forward photomultiplier array. Unlike electrons, spurious events due to mini-discharges at the TPC anode plane lead to a much smaller asymmetry because the short and high pulses of the avalanche saturates all photomultipliers. These background events are now removed within 0.1 ms by the online trigger. This improvement of the data acquisition system allows a strong reduction of the raw event rate written to tape, which is now around 0.17 Hz.

Further efforts towards a nearly automatic data acquisition system were also invested. A typical run lasts for about 5 hours and is occasionally interrupted by hardware failure. The new system now automatically resets the system and restarts the measurement. The experiment can be monitored remotely, e.g. from CERN. This increases significantly the live time of the experiment, as the access and the permanent presence of personnel on site, especially during nights and week-ends, is regulated at a commercial nuclear reactor.

The anticompton vetoes more than 99 % of the photon induced background. We have, however, observed much more background than expected. This background turned out to be produced by radon introduced in the gas by the oxisorb filters. Activity measurements confirmed that the zeolites in the oxisorbs contained much higher quantities of uranium than foreseen. We have replaced the oxisorb filter in winter 1999 by smaller, low background ones. Electronic noise in the readout chain of the TPC has also been drastically reduced and improvements in the gas purification system were made.

The MUNU detector is now operating correctly at a CF_4 pressure of 3 bar. The TPC voltage is -35 kV and the maximum drift time of 71 μs corresponds to a drift velocity of 2.3 cm/ μs . The background was studied during a six weeks reactor shutdown in summer 1999. We collected some 80,000 background events with the neutrino trigger. Between September 1999 and March 2000 we collected some 300,000 events with reactor on.

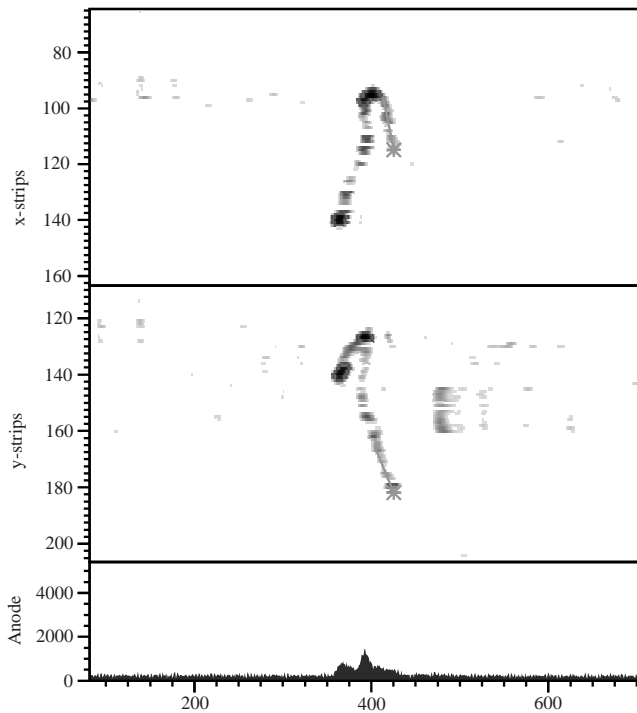


Figure 2.1: A typical neutrino scattering candidate (xz - and yz -projections) and the corresponding pulse height from the anode plane (bottom). The interaction vertex is marked by a star. Note the blob due to the large energy loss at the end of the electron range.

The AC and TPC calibrations were done with traversing cosmic rays and radioactive sources. The energy resolution from the TPC measured with manganese is 7% FWHM at 3 bar and 1 MeV. This corresponds to measurements done at Neuchâtel with X-rays of 60 keV from americium, for which we found 46% FWHM. The typical rate reductions by the online trigger and offline analysis are as follows: without online filtering the detector records about 15,000 electron events/day, most of which are due to mini-discharges and from tracks crossing the amplification gap around the anode. The online filter and a provisional threshold of 700 keV for the electron energy leaves about 500 events/day, of which about 300 are contained in a fiducial volume of 45 cm radius (the full TPC radius is 50 cm). About 150 electron events are found with no associated low energy photon converted in the AC. These events are scanned by eye and the original direction of the track has to lie inside a cone of given aperture which depends on the electron energy. Furthermore, the neutrino energy calculated from the recoil angle and the electron energy has to be positive.

For neutrino scattering events the electron has to be emitted in the opposite (forward) direction to the reactor core, while background events are uniformly distributed. From the data analyzed so far we obtain a very preliminary 32.6 ± 1.7 events/day in the forward direction and 28.6 ± 1.6 events/day in the backward direction. This then leads to a net excess of neutrino induced events of 4.0 ± 2.4 events/day while simulations assuming the standard model predict 1.3/day with the present rather strong software cuts. A typical event in the forward cone is depicted in fig. 2.1.

Figure 2.2 shows the vertex distributions for reactor on and reactor off for a sample collected in 1999. The corresponding energy distributions of the recoil electron, normalized to the same running time, is also shown. Although not very significant, the observed slow increase of the energy distribution at low energy with reactor on was expected and is therefore encouraging.

However, above 1 MeV the background is still an order of magnitude higher than forecasted in the proposal. Note that the current upper limit on the neutrino magnetic moment [1] is derived from an experiment which has a background over signal ratio of 100:1.

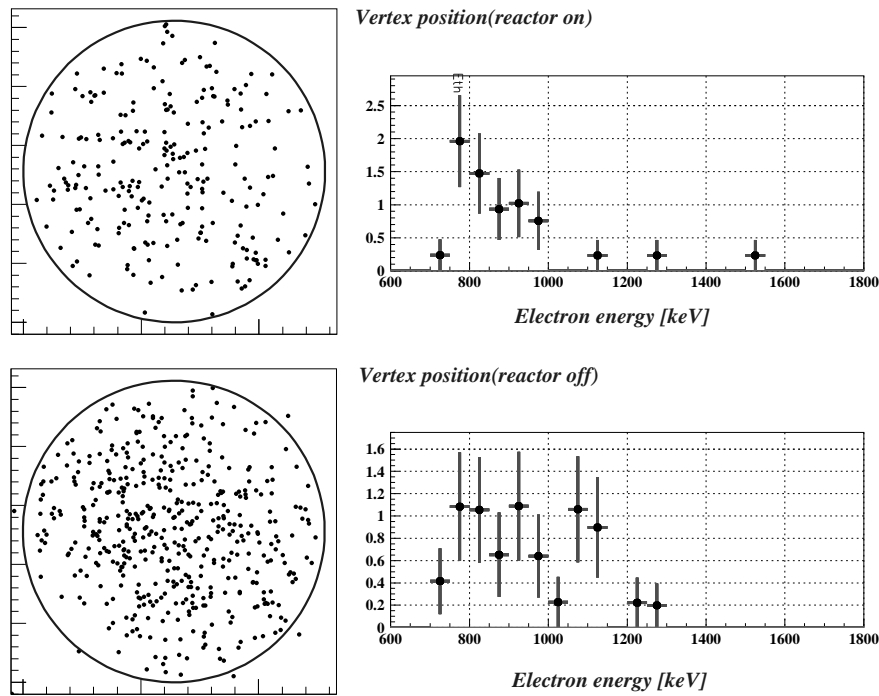
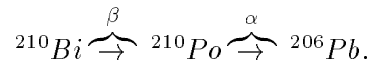


Figure 2.2: Vertex distribution for forward emitted electrons with reactor on (top) and reactor off (bottom). The data taking time with reactor off was much longer. The recoil energy distribution per unit time is shown on the right for reactor on and off. The threshold for electrons was set to 700 keV.

The high background in our experiment has been traced to the probable presence of ^{210}Pb (from the decay chain of ^{222}Rn) implanted on the high voltage cathode surface. This nuclide decays to



The α emission from the daughter decay can be observed directly with the photomultipliers. One measures the time delay between the light pulse generated by the scintillation of CF_4 and the light pulse from the avalanche at the anode. The energy deposits from α 's indeed occur near the cathode, at the maximum drift time. The same method cannot be applied for electrons since the light from CF_4 is too weak to be seen by the photomultipliers. However, we see a clear peak of electrons coming from the cathode end of the TPC, presumably due to the decay of ^{210}Bi .

We have therefore decided to open the detector in April 2000 and to clean (etch) or replace the high voltage cathode. Data taking should then resume in May and continue until the end of 2001 at which time the original goal of the project will hopefully be achieved.

References

- [1] A. I. Derbin et al., JETP Lett. 57 (1993) 768
- [2] C. Amsler et al., Nucl. Instr. Meth. in Phys. Res. A 396 (1997) 115
- [3] O. Link, Diplomarbeit, Universität Zürich (1999)

3 Search for μ -e Conversion with SINDRUM II

R. Engfer, E.A. Hermes, T. Kozlowski, G. Kurz,
F. Riepenhausen, A. van der Schaaf and P. Wintz

in collaboration with:

III. Phys. Institut der RWTH Aachen and PSI Villigen.

SINDRUM II Collaboration

Various observations on solar and atmospheric neutrinos indicate that neutrino states oscillate (much like neutral kaons) which means that lepton flavor is not a conserved quantity. Since in the standard model neutrino masses are set to zero "by hand", the model would need some minor modifications only. Since this mechanism of lepton flavor violation (LFV) does not lead to any observable effects in LFV decay modes involving charged leptons, their observation would require a much more fundamental extension to the model, such as supersymmetry (between fermions and bosons) and/or grand-unification (of the various gauge couplings).

The SINDRUM II project [1] aims at testing the conservation of lepton flavor by a search for μe conversion in muonic atoms. The process would lead to the emission of mono-energetic electrons with a momentum (depending on the muon binding energy) around 100 MeV/c. It is our goal to reach a sensitivity beyond 10^{-13} for the branching ratio relative to nuclear muon capture. SINDRUM II is a solenoidal magnetic spectrometer with 40% solid angle and 1% momentum resolution.

As discussed in last years annual report a new dedicated beamline was brought into operation towards the end of 1998. The major new element is a 9 m long superconducting magnet. Only very recently, after a series of modifications, reliable operation of this PMC magnet was obtained at its design value of 1.5 T.

One of the main difficulties of the experiment is potential background induced by pions contaminating the beam. Radiative pion capture (RPC), followed by e^+e^- pair production, is a source of electrons and positrons in the interesting momentum range around 100 MeV/c. The process leads to identical kinematical distributions for electrons and positrons with momenta reaching beyond the muon endpoint. Two different processes should be distinguished:

- RPC in the moderator

A large number of pions stop inside the degrader at the PMC entrance. Electrons and positrons from RPC may reach the setup and scatter off the target into the acceptance of the spectrometer. Our simulation shows that at a PMC field of 0.72 T roughly one out of 10^7 pion stops in the moderator result in an electron reaching the target with an energy above 90 MeV. This background differs from the signal both in momentum and in angular distribution.

- RPC in the target

A tiny number of pions may reach the target. RPC leads to a background that is isotropic and can be distinguished from the events of interest only by their different momentum distribution. In order to keep the probability to observe an RPC electron in a 5 MeV/c interval around 100 MeV/c below 0.3 at most 3×10^4 pions may reach the target. Assuming a measuring time of 100 days this corresponds to a tolerable rate of one pion every five minutes.

In 1998 it had become clear that the planned mode of operation, injecting a 90 MeV/c π^- beam into the PMC and separating the decay muons from the surviving pions with the help

of a beam blocker, could not be used because of a very heavy load on the SINDRUM tracking detectors caused by beam electrons scattering off the target. In this situation it was decided to use muons from the pion cloud around the pion production target and suppress the pion background with the help of the moderator at the PMC entrance. At the momenta of interest muons have a mean range in matter which is about twice longer than the pion range. The remaining purpose of the PMC magnet is to efficiently couple the spectrometer magnet to the π E5 exit and to reduce the pion contamination of the beam by an additional 2-3 orders of magnitude by doubling the distance between the production target and the experimental setup.

3.1 Search for conversion on gold: final result from 1997 run

Already in 1997, at a reduced PMC field of ≈ 0.3 T, measurements had been done using a 26 MeV/c cloud μ^- beam on a gold target. Although the data proved to be very clean (no background from pions or scattered electrons) the stop rate was a disappointing $0.5 \times 10^6 \mu^- s^{-1}$. The resulting momentum distribution (see Fig.3.1) shows no events in the μe

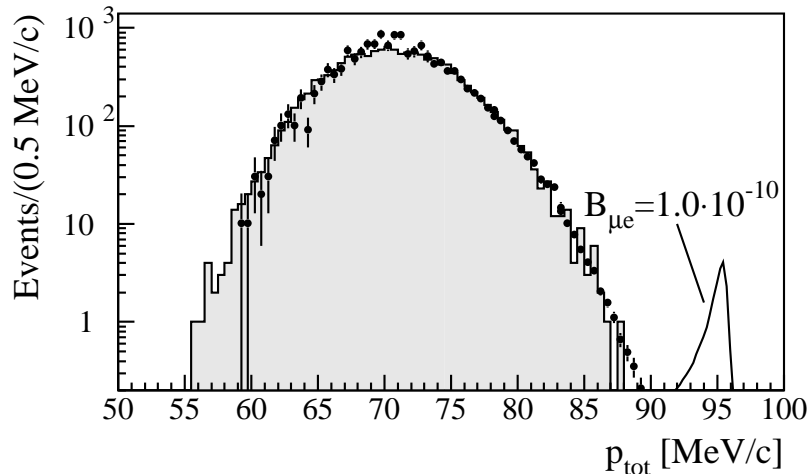


Figure 3.1: *Momentum distributions of electrons emitted in the decay of muonic gold: (i) full histogram: measured data, (ii) data points: simulated data for decay in orbit $\mu^- \text{Au} \rightarrow e^- \nu \bar{\nu} \text{Au}$, (iii) peak around 95 MeV/c (i.e. muon rest mass reduced by ≈ 10 MeV atomic binding energy): simulated μe data. The steep drop in intensity towards lower momenta reflects the p_{\perp} threshold imposed by the spectrometer field.*

signal region and can be attributed, both in shape and in magnitude, to muon decay in orbit. The analysis [2] has resulted in:

$$B_{\mu e}^{\text{Au}} < 1.9 \times 10^{-11} \quad (90\% \text{ C.L.}),$$

which improves over the best previous limit on a heavy target (our own result on lead [3]) by a factor 2.4.

In order to increase the stop rate beyond $10^7 s^{-1}$ the beam momentum has to be raised. At the other hand beam-related background may set in. As will become clear below we are still in the process of optimizing the various parameters that affect stop rate and pion contamination.

3.2 Search for conversion on lead: first results from 1998 run

In 1998 the beam was tuned to 75 MeV/c and data were taken on lead. The target had the shape of a tube with a length of 60 cm, a diameter of 70 mm and a wall thickness of 0.5 mm. By using an additional moderator at the position of the first focus inside the ASC magnet (*double-degrader method*), the electron load could be reduced to an acceptable level with a μ^- stop rate around $0.6 \times 10^7 s^{-1}$. Figure 3.2 shows the distribution of the polar angle,

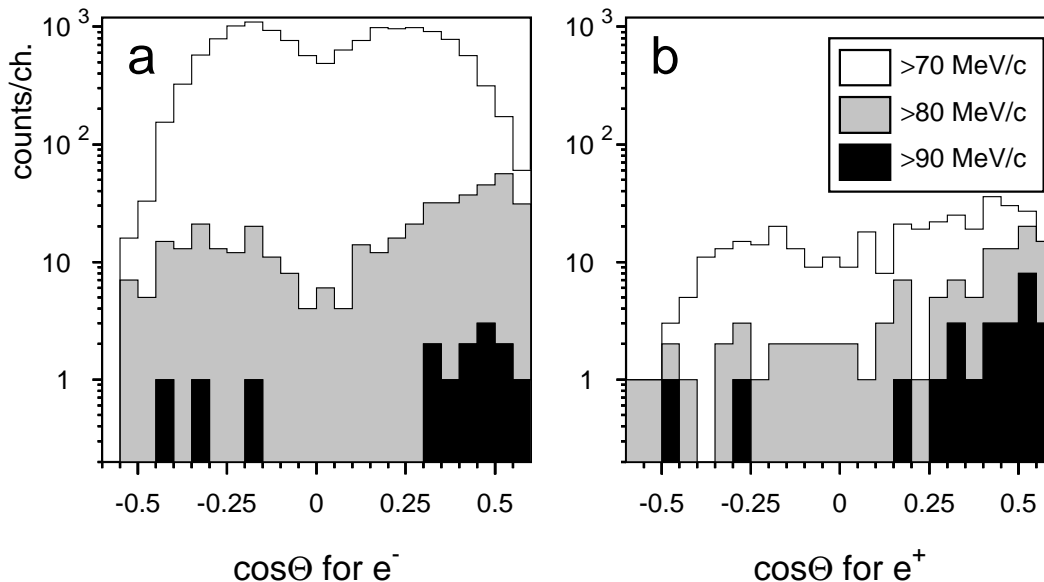


Figure 3.2: *Distributions of $\cos\theta$, with θ the emission angle relative to the beam direction, for various momentum thresholds. The loss in acceptance around zero ($\theta = 90^\circ$) is explained by energy loss in the target before the endcap trigger counters could have been reached. For momenta above 80-85 MeV/c there appear pronounced peaks in forward direction with roughly equal yields for both charges. See the text for a discussion.*

both for electrons and positrons, at various lower thresholds on the momentum of the decay particle. For relatively low thresholds the distributions are symmetric about 0, as should be expected for e^- from μ decay in orbit and e^+ from radiative μ^- capture followed by $\gamma \rightarrow e^+e^-$ pair production. For momenta above ≈ 80 MeV/c one notices enhancements in the forward direction ($\cos\theta$ around 0.5) of roughly equal strength for both charges. These events are attributed to radiative pion capture in the moderator at the PMC entrance. A few electron and positron events are found in the backward hemisphere. Presently we are still studying their nature. The most likely explanation would be radiative pion capture in the target. In this case $\approx 10^5$ pions would have reached the target, corresponding to a pion contamination of 10^{-8} in the target stops.

3.3 Results from 1999

In 1999 a systematic study of the rate of cloud muons at different beam momenta was performed. Table 3.1 shows the values measured at the exit of the PMC, which show a steeper momentum dependence than expected.

Based on these results we installed an 8 mm CH_2 degrader inside the collimator at the PMC entrance and selected a beam momentum of 50 MeV/c. The rate observed at the center of the spectrometer was $2 \times 10^7 \mu^- / \text{mA.s}$, 70% of which could be stopped in a titanium

Table 3.1: *Particle yields at $\pi E5$*

beam momentum MeV/c	μ^- yield at PMC exit		π^- yield at PMC entrance	π/μ ratio calculated [4]
	measured $10^6/\text{mA.s}$	calculated [4] $10^6/\text{mA.s}$	calculated [4] $10^6/\text{mA.s}$	
28	2.6 ^a	4	0.03	0.008
35	7.7	6.5	0.3	0.05
40	13	8	1	0.13
45	19	10	3	0.3
55	36	15	23	1.5
65	54	28	90	3.2

^athis value may have suffered from an additional 0.5 mm mylar foil in the last bending magnet

target of length 50 cm, radius 15 mm and total weight 60 g. During several weeks data were taken at 50 MeV/c beam momentum. These data were scanned on-line and found free of π background. In an attempt to raise the stop rate beyond $2 \times 10^7 s^{-1}$ we increased the beam momentum. However, as can be seen in Fig.3.3 we did not succeed to keep the pion background under control. Unfortunately, we only realized this after the measurements were finished. The main problem is that it is not obvious how to monitor a pion stop rate around one per minute among $10^7 \mu^- s^{-1}$.

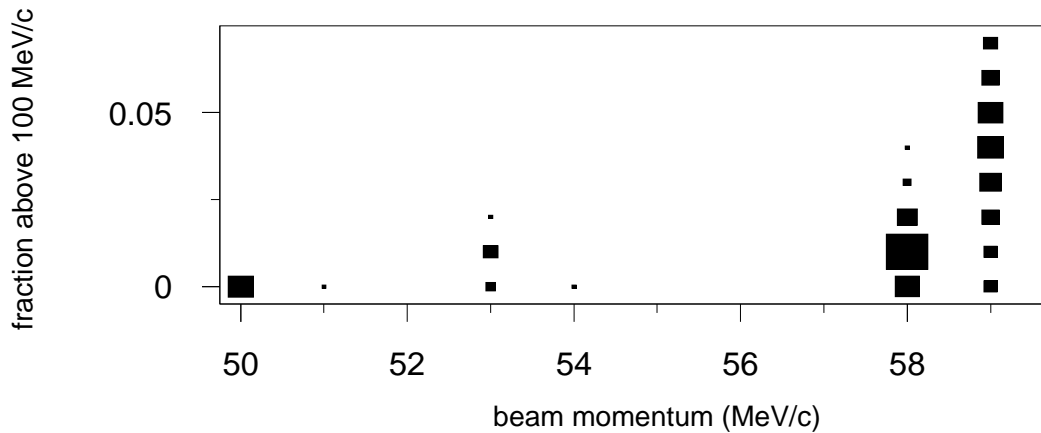


Figure 3.3: *Result of the analysis of the ≈ 2000 subsets of the 1999 data. In the spectra the region above 100 MeV/c is completely dominated by π^- induced background. Except for the $\approx 10\%$ data taken at 50 MeV/c all distributions show significant background contributions.*

The rate of pions reaching the target is equal to the product of the rate of π^- entering the PMC collimator, the probability to penetrate through the moderator and the probability to survive over the distance between moderator and target. As can be seen from Table 3.1 the π^- rate is $O(10^7) s^{-1}$ at the entrance of the PMC. Simulation shows that the survival probability is $O(3 \times 10^{-4})$. This means that *only one out of 10^6 pions may cross the moderator*. For the momenta of interest the muon range is about twice the pion range. Pions of 60 MeV/c have the same range as muons of 50 MeV/c. From these considerations one finds that *the 50 MeV/c beam may contain at most a 10^{-6} component with momenta above 60 MeV/c*.

3.4 Intentions for 2000: gold versus titanium

Presently we are designing better diagnostic tools to handle the high-momentum tails in the beam. Fortunately, there are many parameters (slits, magnet settings) to affect those tails. We plan to make a systematic study, before starting a ≈ 4 months measurement on gold.

In 1999 we achieved a μ^- stop rate of $2 \times 10^7 s^{-1}$. Given the shorter production target and assuming we will sacrifice $\approx 30\%$ beam intensity in favor of a reduced pion contamination we may have to live with a stop rate of $\approx 10^7 \mu^- s^{-1}$ this year. Assuming efficiencies as in 1997, when a $0.5 \times 10^6 s^{-1}$ stop rate during two weeks resulted in a 2×10^{-11} upper limit [2], we would be able to reach a limit of 2×10^{-13} in ten weeks (no background - no signal). In this situation we decided to take only data on one target and choose gold for the following reasons:

- From a theoretical point of view conversion on gold is up to 3 times more likely than conversion on titanium [5].
- A future experiment, such as MECO, using pulsed beam to fight the beam-related background would not be able to measure a heavy element with less than 100 ns life time. The lifetime of muonic gold is 73 ns.
- On gold we can raise the sensitivity by two orders of magnitude, on titanium the improvement would only be a factor three as compared to our own measurement [6].

References

- [1] PSI proposal R-87.03
- [2] *Suche nach der Myon-Elektron-Konversion in Gold*, F. Riepenhausen, PhD thesis, Zürich University, 1999.
- [3] SINDRUM II Collaboration, W. Honecker *et al.*, Phys.Rev.Lett. **76** (1996), 200.
- [4] PSI Users' Guide, *Accelerator Facilities*, (1994) 32.
- [5] T.S. Kosmas, Z. Ren and A. Faessler, Nucl.Phys. **A665** (2000) 183, and references therein.
- [6] P. Wintz, Proceedings of the 29th International Conference on High Energy Physics, ed. A. Astbury, D. Axen, J. Robinson, World Scientific, Singapore (1999).

4 Rare Kaon Decays

A.Sher and P.Truöl

in collaboration with:

Paul-Scherrer-Institut, CH-5234 Villigen (J.Egger, W.D.Herold, H.Kaspar, and H.Weyer), Brookhaven National Laboratory, Upton, NY-11973, USA, University of New Mexico, Albuquerque, NM-87131, USA, University of Pittsburgh, Pittsburgh, PA-15260, USA, Yale University, New Haven, CT-06511, USA, Institute for Nuclear Research, Academy of Sciences, 117 312 Moscow, Russia

Experiment E-865 at Brookhaven AGS

The final long data taking run for experiment E865 at the Brookhaven AGS ended on December 31, 1998. Since then the analysis of the data taken in 1996, 1997 and 1998 with a broad band charged particle spectrometer equipped with a particle identification system on rare K^+ decays in-flight into multilepton final states has progressed and been finalised for some channels.

The flavour changing neutral current decays $K^+ \rightarrow \pi^+ e^+ e^-$ ($K_{\pi ee}$) and $K^+ \rightarrow \pi^+ \mu^+ \mu^-$ ($K_{\pi \mu \mu}$) are known to be dominated in the Standard Model by long-distance effects involving one-photon exchange. Our published results for these decays not only include precise branching ratios

$$\begin{aligned} B(K_{\pi ee}) &= (2.94 \pm 0.05(\text{stat}) \pm 0.13(\text{syst}) \pm 0.05(\text{theor})) \times 10^{-7} & [1] \\ B(K_{\pi \mu \mu}) &= (9.22 \pm 0.60 \pm 0.49) \times 10^{-8} & [2] \end{aligned} ,$$

but also establish firmly the vector nature of the interaction, and resolve the discrepancy of the older data with $\epsilon\mu$ universality. Furthermore the form factor parameters ($f_V(z) = a + bz + w^{\pi\pi}(z)$, $z = M_{ee}^2/m_K^2$) have been determined with $a = -0.587 \pm 0.010$ and $b = -0.655 \pm 0.044$, a result which points to a small but important contribution from the pion loop term $w^{\pi\pi}$ calculated in next-to-leading order chiral perturbation theory.

Table 4.1: *Upper limits for lepton number violating decays established by experiment E865. For each mode the change in electron number L_e , muon number L_μ and total lepton number L are listed.*

Decay mode	ΔL_e	ΔL_μ	ΔL	Branching ratio	Data	Ref.
$K^+ \rightarrow \pi^+ \mu^+ e^-$	1	-1	0	$< 3.9 \cdot 10^{-11}$	$K_{\pi \mu e}$ (1996)	[3, 4]
				$< 2.1 \cdot 10^{-10}$	$K_{\pi \mu e}$ (1995)	[5, 6]
				$< 2.0 \cdot 10^{-10}$		[7]
				$< 2.8 \cdot 10^{-11}$	Combined	
$K^+ \rightarrow \pi^+ e^+ \mu^-$	-1	1	0	$< 7.0 \cdot 10^{-9}$		[9]
$\pi^0 \rightarrow \mu^+ e^-$	1	-1	0	$< 5.1 \cdot 10^{-10}$	K_{e4} (1997)	[8]
				$< 1.7 \cdot 10^{-8}$		[9]
$K^+ \rightarrow \mu^+ e^+ \pi^-$	-1	-1	2	$< 3.8 \cdot 10^{-10}$	$K_{\pi \mu e}$ (1996)	[4]
				$< 7.0 \cdot 10^{-9}$		[9]
$K^+ \rightarrow e^+ e^+ \pi^-$	-2	0	-2	$< 4.9 \cdot 10^{-10}$	K_{e4} (1997)	[8]
				$< 1.0 \cdot 10^{-8}$		[9]
$K^+ \rightarrow \mu^+ \mu^+ \pi^-$	0	-2	-2	$< 6.3 \cdot 10^{-10}$	K_{e4} (1997)	[8]
				$< 1.5 \cdot 10^{-4}$		[9]
				$< 3.0 \cdot 10^{-9}$	$K_{\pi \mu \mu}$ (1997)	[8]

For the lepton flavour conservation violating decay $K^+ \rightarrow \pi^+ \mu^+ e^-$ ($K_{\pi\mu e}$) the analysis of the 1996 data has been completed [3, 4]. It yielded an upper 90% confidence limit for the branching ratio of $3.9 \cdot 10^{-11}$, which combined with our 1995 data [5, 6] and those from earlier experiments [7] reduces to $2.8 \cdot 10^{-11}$ (see Table 4.1). From our 1998 run we expect a sensitivity level below 10^{-11} . The first analysis pass of the 600 tapes with about 2×10^8 events recorded has recently been finished. The second pass will further reduce the sample for the maximum likelihood method signal search. The analysis of these data is subject of the thesis of Aleksej Sher. Figure 4.1 shows the results of such an analysis for the 1996 data [3, 4], from which the quoted limit was extracted.

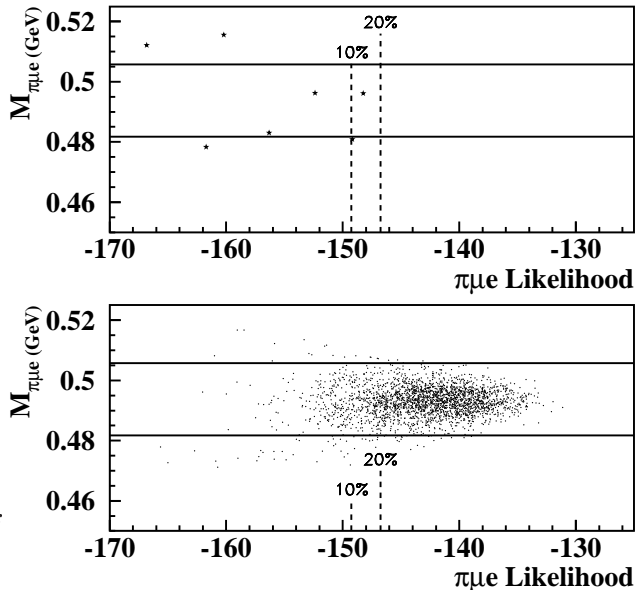


Figure 4.1: Scatter plot of the $\pi\mu e$ log-likelihood function versus the $\pi\mu e$ invariant mass for data (total 1996 sample, top) and Monte Carlo (expected signal, bottom). The horizontal lines indicate the acceptance in $\pi\mu e$ mass, while the dashed vertical lines mark the boundaries for an event having a 10% or 20% probability of being a signal event [3, 4].

As a by-product of our main analysis we have also reduced by at least an order of magnitude the limits on the following decays: $\pi^0 \rightarrow \mu^+ e^-$, $K^+ \rightarrow \mu^+ \mu^+ \pi^-$ ($K_{\mu\mu\pi}$), $K^+ \rightarrow e^+ \mu^+ \pi^-$ ($K_{e\mu\pi}$), $K^+ \rightarrow e^+ e^+ \pi^-$ ($K_{ee\pi}$) and $K^+ \rightarrow \pi^+ e^+ \mu^-$ ($K_{\pi e\mu}$) (see Table 4.1). The limit for the unobserved π^0 -decay was deduced from the $K_{\pi\mu e}$ data [4], for the $K_{\mu\mu\pi}$ decay from the dedicated $K_{\pi\mu\mu}$ trigger run in 1997, while the other three decays could in principle be contained in the K_{e4} sample.

The $K^+ \rightarrow \pi^+ \pi^- e^+ \nu_e$ (K_{e4}) sample was also taken in 1997 with a dedicated trigger. $4.4 \cdot 10^5$ nearly background free (after appropriate cuts) events were recorded for this decay with a measured branching ratio of $3.91 \cdot 10^{-5}$ [9]. These data represent a 14-fold increase in statistics compared to previous experiments [10]. Figure 4.2 shows the reconstructed $\pi\pi$ mass from these data compared to Monte Carlo simulations, one of the many control plots demonstrating our good understanding of the data and the detector. These data were then used to fit to $\pi\pi$ scattering phase shift differences and form factor as a function of $\pi\pi$ mass. A preliminary result of this analysis, without radiative corrections, which was presented at a 1999 conference [11], is shown in Fig. 4.2. In this first analysis the method described by Rosset et al. [10] was used. A more sophisticated treatment based on chiral QCD perturbation theory is in preparation. Since a large number of theoretical calculations within this theoretical frame exist, our final results are eagerly awaited.

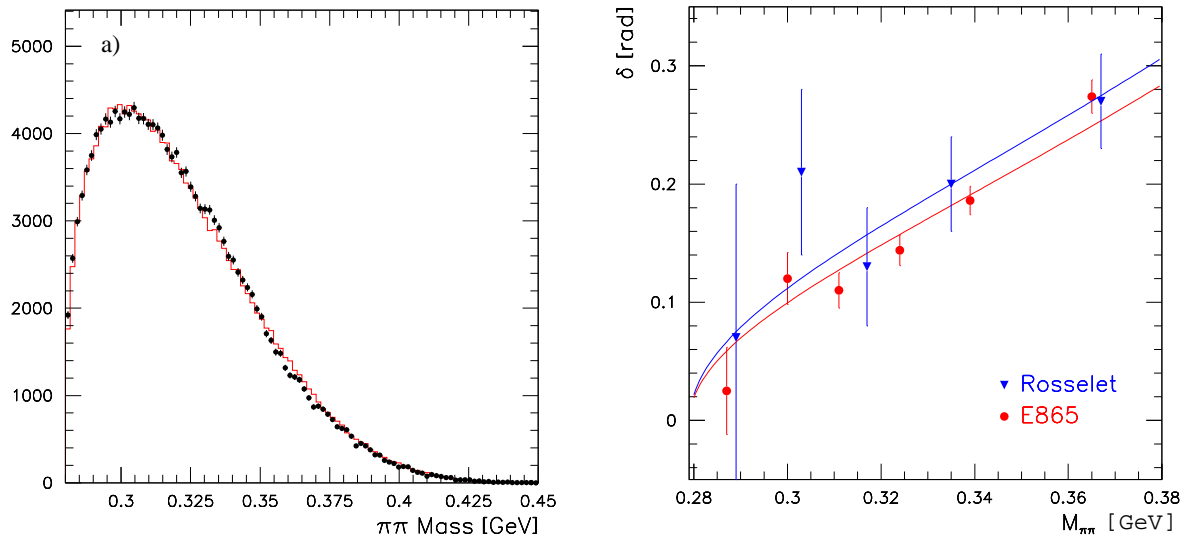


Figure 4.2: a) Reconstructed $\pi\pi$ mass distribution for K_{e4} events. The dots represent the data, the histogram shows the Monte Carlo simulation. b) Dependence of the s -wave phase shift parameter $\delta \equiv \delta_0^0 - \delta_1^1$ on the $\pi\pi$ mass [11]. The triangles are from an older experiment with fewer events, where also the fitting method is described [10].

References

- [1] *A New Measurement of the Properties of the Rare Decay $K^+ \rightarrow \pi^+ e^+ e^-$* , R. Appel et al., Phys.Rev.Lett. **83** (1999), 4482.
- [2] *A New Measurement of the Rare Decay $K^+ \rightarrow \pi^+ \mu^+ \mu^-$* , H. Ma et al., Phys.Rev.Lett. **84** (2000), 2580.
- [3] *An Improved Upper Limit on the Branching Ratio of the Decay $K^+ \rightarrow \pi^+ \mu^+ e^-$* , H. Do, Thesis, Yale University, New Haven (2000).
- [4] *An Improved Limit on the Rate of the Decay $K^+ \rightarrow \pi^+ \mu^+ e^-$* , R. Appel et al., submitted to Physical Review Letters.
- [5] *Experiment E865 at BNL: a search for the decay $K^+ \rightarrow \pi^+ \mu^+ e^-$* , S. Pislak, Thesis, University of Zürich (1997).
- [6] *A search for the decay $K^+ \rightarrow \pi^+ \mu^+ e^-$* , D. Bergman, Thesis, Yale University, New Haven (1997).
- [7] A.M.Lee et al., Phys.Rev.Lett. **64** (1990), 165.
- [8] *Search for Lepton Number Violating Decays*, R. Appel et al., to be submitted to Physical Review Letters.
- [9] *Review of Particle Properties*, C.Caso et al., Eur.Phys.J. **C3** (1998), 1.
- [10] L. Rosselet et al., Phys.Rev. **D15** (1977), 574.
- [11] *A New Measurement of the $K^+ \rightarrow \pi^+ \pi^- e^+ \nu_e$ Decay*, S. Pislak, in *HadAtom 99*, Proc. Workshop on Hadronic Atoms, Bern, October 1999, J. Gasser, A. Rusetsky, and J. Schacher eds., p.25, hep-ph 9911339.

5 Meson Spectroscopy at LEAR with the Crystal Barrel

C. Amsler, P. Giarritta, M. Heinzemann and C. Regenfus

in collaboration with:

Academy of Science (Budapest); Universities of Bochum, Bonn, Hamburg, Karlsruhe, München, Paris VI; CERN; Carnegie Mellon University (Pittsburgh); CRN (Strasbourg); RAL; UC (Berkeley)

(CRYSTAL BARREL COLLABORATION)

During 1999 we finalized the analysis of proton-antiproton annihilation at rest into $\omega\pi^0\pi^0$ and $\omega\eta\pi^0$ (7γ final state) and antiproton-deuteron annihilation into ΛK^0 and $\Sigma^0 K^0$. The analysis of proton-antiproton annihilation in flight into three neutral pseudoscalar mesons at 900 MeV/c (6γ final state) also nears completion. We shall first briefly summarize the final conclusions on the 7γ and our progresses in the 6γ final states. Preliminary results were presented in last year's annual report. We then discuss our analysis of antiproton-deuteron annihilation in somewhat more details.

5.1 Proton-antiproton annihilation into 6γ and 7γ

The annihilation channels $\bar{p}p \rightarrow \omega\eta\pi^0$ and $\omega\pi^0\pi^0$ at rest, leading to 7 detected γ 's ($\eta, \pi^0 \rightarrow \gamma\gamma$ and $\omega \rightarrow \pi^0\gamma$), were analyzed with the full available data samples, giving 34,064 and 136,023 events, respectively, and taking into account the angular distribution of the γ in the ω rest frame [1]. The data were analyzed with the K-matrix formalism which fulfils unitarity for broad overlapping resonances and describes two or more open channels competing in resonance decays. In contrast to earlier work [2] using the Breit-Wigner formalism, a completely satisfactory description of the channel $\omega\pi^0\pi^0$ is now achieved, with contributions from $b_1(1235)\pi^0$, $\omega f_2(1270)$ and $\omega(\pi\pi)_S$, where $(\pi\pi)_S$ is the $\pi\pi$ S-wave that was studied earlier in great details by our collaboration [3].

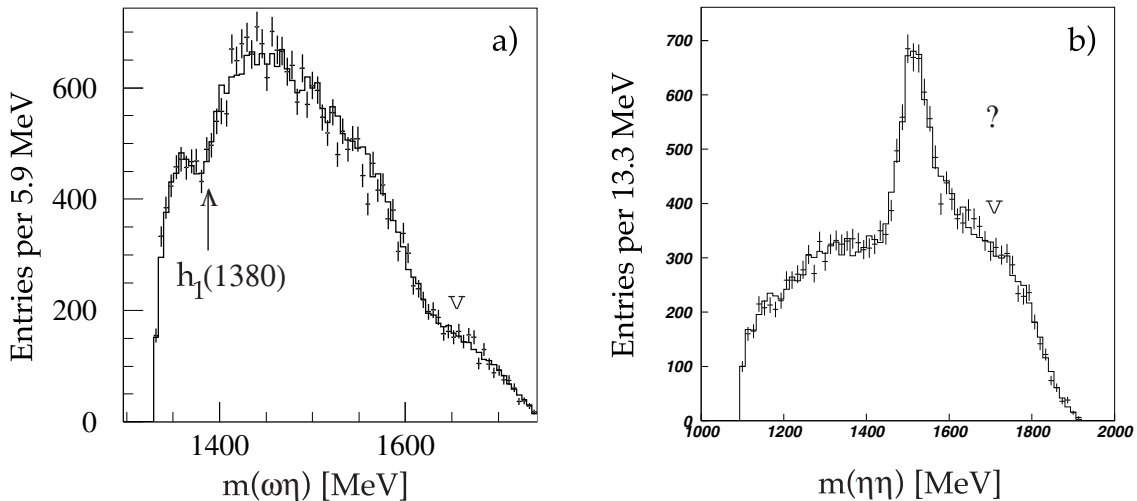


Figure 5.1: a) $\omega\eta$ mass distribution in $\bar{p}p \rightarrow \omega\eta\pi^0$ at rest. The dip at 1380 MeV is due to a 1^{+-} state decaying to $\omega\eta$ near the $K^*\bar{K}$ threshold. The enhancement at 1700 MeV (arrow) is due to a 1^{--} (vector) meson. The histogram shows the K-matrix fit; b) $\eta\eta$ mass distribution in $\eta\eta\pi^0$ at 900 MeV/c. The peak is due to $f_0(1500)/f_2'(1525)$. There is no evidence for $f_0(1710)$ (arrow). The shoulder around 1750 MeV is due to a reflection of $a_0(980) \rightarrow \eta\pi$.

From the channel $\omega\eta\pi^0$ we obtain evidence for two mesons decaying to $\omega\eta$. The present data are the first observations of mesons decaying to $\omega\eta$. A 1^{+-} isoscalar meson is observed at a mass of 1382 ± 2 MeV, with a width of 65 ± 14 MeV. The dip in the distribution (fig.5.1a) is due to the competing decay channel $K^*\bar{K}$ which opens at this mass. It is identified as the $h_1(1380)$, the isospin zero partner of $h_1(1170)$, in which case we determine a singlet-octet mixing angle of $-5.4_{-1.6}^{+2.7^\circ}$ in the $J^{PC} = 1^{+-} q\bar{q}$ nonet. The $h_1(1380)$ was so far poorly established. A weak signal at this mass was reported earlier, albeit in $K^*\bar{K}$ [4, 5]. At 1698 MeV one observes a 111 MeV broad 1^{--} meson (fig.5.1a). Two vector mesons were reported earlier around this mass, $\omega(1600)$ and $\phi(1680)$, decaying to $\rho\pi\pi$ and $\omega\pi$.

The $f_0(1710) \rightarrow \eta\eta$ meson was searched for in $\bar{p}p$ annihilation in flight into $\eta\eta\pi^0$ (6γ final state) at 900 MeV/c [6, 7]. The spin of $f_0(1710)$ was recently established in pp central collisions to be zero. The data from central collisions at 450 GeV point to a dominant $s\bar{s}$ structure and therefore provide a strong evidence for the so far missing $s\bar{s}$ member of the scalar nonet. On the other hand, the $f_0(1500)$ is also observed in central collisions, but not in $\gamma\gamma$. This and the $s\bar{s}$ structure of $f_0(1710)$ add supportive evidence for the glueball nature of $f_0(1500)$ [8]. If $f_0(1710)$ were pure $s\bar{s}$ it should not be produced from the $\bar{p}p$ system which does not contain any s -quark. Figure 5.1b shows the $\eta\eta\pi^0$ mass projection with, indeed, no striking evidence for a state around 1700 MeV. However, the amplitude analysis requires a 300 MeV broad 2^{++} state around 1900 MeV [6]. The analysis of the $3\pi^0$ and $2\pi^0\eta$ channels at 900 MeV/c is in progress.

5.2 Antiproton-deuteron annihilation into ΛK^0 and $\Sigma^0 K^0$

The study of these so-called Pontecorvo reactions with the production of strange baryons is expected to probe quark dynamics. With stopping antiprotons these reactions can only occur by the interaction of the three incoming nucleons, or by final state rescattering.

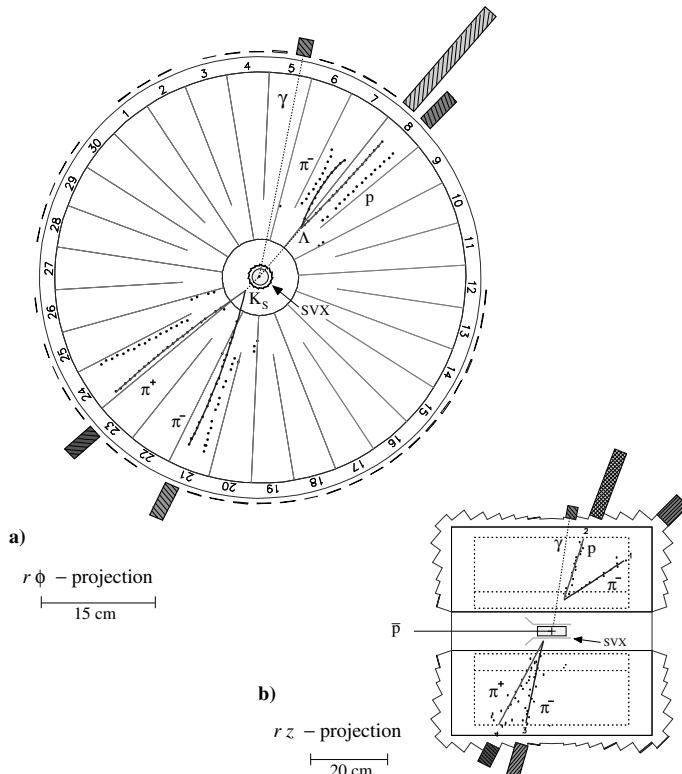


Figure 5.2: A $\bar{p}d \rightarrow \Sigma^0 K_S$ event ($K_S \rightarrow \pi^+\pi^-$, $\Sigma^0 \rightarrow \Lambda\gamma$) seen by the event display; a) transverse view showing the reconstructed tracks in the jet drift chamber (note the left-right ambiguity of hits in the chamber sectors) and the energy deposits in the barrel; b) view along the beam axis. SVX denotes the silicon microstrip detector.

In two-step processes the \bar{p} annihilates on the proton producing a $K^0 \bar{K}^0$ pair. The \bar{K}^0 then interacts with the neutron to generate a Λ or a Σ^0 . In contrast, in fireball processes the \bar{p} interacts simultaneously with the neutron and the proton, generating an ensemble (fireball) of quarks and gluons, which then converts into the observed hadronic final state. For ΛK^0 and $\Sigma^0 K^0$ the two-step mechanism predicts annihilation rates of a few 10^{-7} and 10^{-9} , respectively, while fireball models predict rather similar values in the 10^{-6} range. The ratio of the two branching fractions is considered to be fairly independent of model parameters in both approaches. The large difference of the two-step branching fractions arises from the much larger $KN\Lambda$ coupling, compared to $KN\Sigma^0$. In contrast, the branching ratios for $\Sigma^0 K^0$ and ΛK^0 are equal in the fireball model.

A K^0 and Λ enriched sample of events with antiprotons stopped in a liquid deuterium target was recorded with the Crystal Barrel experiment [9, 10]. This corresponds to about 10^9 annihilations. The Λ and $K^0 \equiv K_S$ have a sufficiently large lifetime to travel several cm before decaying. The silicon microstrip detector surrounding the liquid hydrogen target [11] was therefore used to determine online the charge multiplicity close to the annihilation vertex, while at larger distances the multiplicity was recorded by the jet drift chamber. We studied the final states ΛK_S and $\Sigma^0 K_S$ with $\Sigma^0 \rightarrow \Lambda \gamma$, $\Lambda \rightarrow p \pi^-$, $K_S \rightarrow \pi^+ \pi^-$, and the equivalent final states ΛK_L and $\Sigma^0 K_L$ (with noninteracting and therefore undetected K_L). The trigger recorded data with either one or two secondary vertices, corresponding to a multiplicity increase from 0 to 2 for ΛK_L and $\Sigma^0 K_L$, or from 0 to 4 for ΛK_S and $\Sigma^0 K_S$ events, respectively. These triggers enriched the Pontecorvo channels by roughly two orders of magnitude with respect to a minimum bias experiment. A $\Sigma^0 K_S$ event is shown in fig. 5.2.

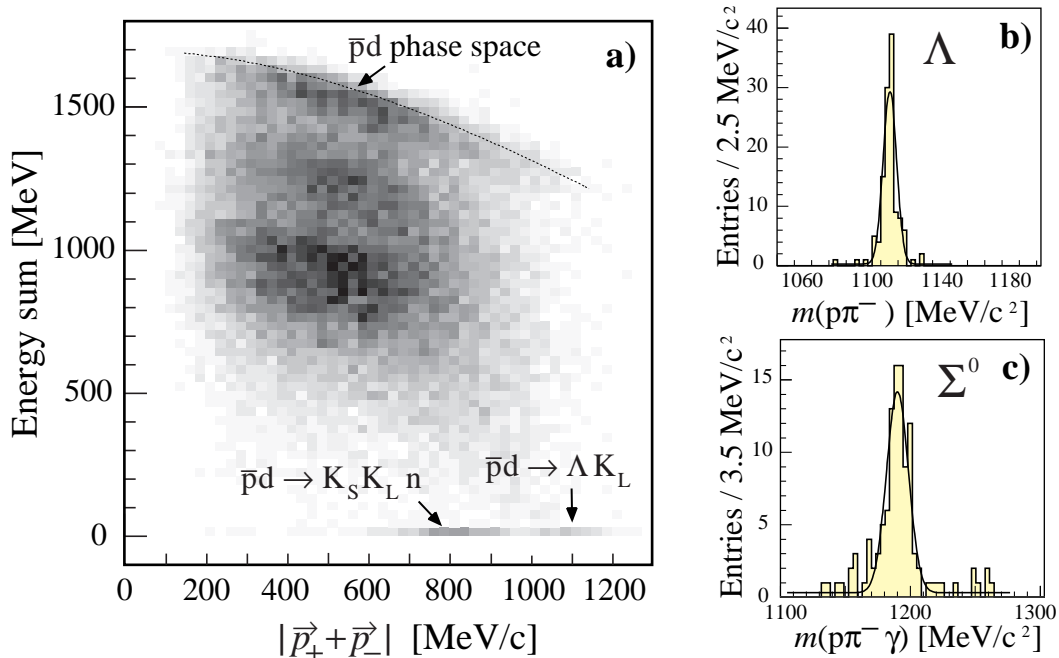


Figure 5.3: a): Total energy measured in the barrel versus total charged particle momentum for the 2-prong sample; b) invariant $p\pi^-$ mass showing the Λ . The fit (curve) gives a Λ mass of $1116 \text{ MeV}/c^2$ and an r.m.s resolution of $4 \text{ MeV}/c^2$; c) invariant $p\pi^-\gamma$ mass for 2-prong events with the $p\pi^-$ mass consistent with Λ decay and an additional single γ , showing the Σ^0 . The fit (curve) gives a Σ^0 mass of $1190 \text{ MeV}/c^2$ and an r.m.s resolution of $8 \text{ MeV}/c^2$. The corresponding tabulated values for the Λ and Σ^0 masses are 1115.7 and $1192.6 \text{ MeV}/c^2$.

Samples of about 10^6 events each were collected with the 2- and 4-prong topological triggers. The majority of events, of the type $K^0\bar{K}^0m\pi^0$ ($m=0,1,2,\dots$) with a low energy undetected neutron, could be rejected offline since the detector had an acceptance close to 4π for photons. The data samples were cleaned up by requiring unambiguous single or double vertex fits for two or four charged particles with opposite charges. Backscattered charged particles from the CsI barrel were eliminated by a cut requiring an upper limit for the opening angles at the vertices. Entries in the crystal barrel, not matching charged particle trajectories, were identified as photons if the energy deposit in the central crystal amounted to more than 13 MeV. Protons were distinguished from pions through their energy losses in the jet drift chamber. Figure 5.3a shows for instance the total energy measured in the CsI barrel as a function of total momentum carried off by the charged particles in the 2-prong sample. The dominant processes (broad bands bottom to top) stem from $\Lambda K^0 m\pi^0$ with K_L missing, K_L detected and $K_S \rightarrow \pi^0\pi^0$. The channel ΛK_L is clearly separated from background. The corresponding plot of barrel energy vs. total momentum carried off by the charged particles and a single photon (channel $\Sigma^0 K_L$) looks similar. Figure 5.3b and c show clear and nearly background free Λ and Σ^0 peaks in the $p\pi^-$ and $\pi^-p\gamma$ invariant mass spectra after all cuts. Full details on the reconstruction procedure can be found in ref. [10].

We obtained 107 ΛK_L and 83 $\Sigma^0 K_L$ events. The corresponding event numbers for ΛK_S and $\Sigma^0 K_S$ were 85 and 61, respectively. The branching ratios for these reactions are consistent for the 2- and 4-prong samples, giving the average $(2.35 \pm 0.45) \times 10^{-6}$ for ΛK^0 and $(2.15 \pm 0.45) \times 10^{-6}$ for ΣK^0 , in good agreement with predictions from the fireball model [12]. These rates exceed by far the values expected from two-step models. The relative rate is close to unity (0.92 ± 0.15) and agrees with calculations from the fireball model. With the present understanding of meson - baryon interaction, this means that the two-step mechanism is inadequate to describe these Pontecorvo reactions. Our results are consistent with the original nucleonic quarks being dissolved in a large bag with baryon number $B=1$.

References

- [1] P. Giarritta, PhD Thesis, Universität Zürich (2000).
- [2] C. Amsler et al., Phys. Lett. B 311 (1993) 362.
- [3] For a review see C. Amsler, Rev. Mod. Phys. 70 (1998) 1293.
- [4] D. Aston et al., Phys. Lett. B 201 (1988) 573.
- [5] A. Abele et al., Phys. Lett. B 415 (1997) 280.
- [6] M. Heinzelmann, PhD Thesis, Universität Zürich, in preparation.
- [7] C. Amsler, Proc. 8th Int. Conf. on Hadron Spectroscopy, Beijing (1999), Nucl. Phys. A (in print).
- [8] C. Amsler, Proc. Workshop on Hadron Spectroscopy, Frascati Physics Series, Vol. XV (1999) p. 609.
- [9] C. Regenfus, Proc. XVth Particles and Nuclei Int. Conf., Uppsala, 1999 (in print).
- [10] A. Abele et al., Phys. Lett. B 469 (1999) 276.
- [11] C. Regenfus, Nucl. Instr. Meth. in Phys. Res. A 386 (1997) 60.
- [12] J. Cugnon and J. Vandermeulen, Phys. Lett. B146 (1984) 16, Phys. Rev. C39 (1989) 181.

6 Production and Spectroscopy of Antihydrogen

C. Amsler, R. Brunner, E.A. Hermes, P. Niederberger, H. Pruyss,
C. Regenfus, P. Riedler, J. Rochet and M. Zwahlen

in collaboration with:

CERN, Massachusetts Institute of Technology, Pennsylvania State University, Universities of Aarhus, Brescia, Genoa, Napoli, Pavia, Pisa, Rome, Stockholm, Tokyo, Wales (Swansea, UK), Institute of Physics (Cetinje, Montenegro), Universidade Federal do Rio de Janeiro

(ATHENA Collaboration)

The goal of the ATHENA (AnTiHydrogEN Apparatus[1]) experiment is to produce antihydrogen atoms at low energies, to capture them in a magnetic trap and to compare by 2 photon laser excitation the 1S - 2S energy difference of antihydrogen with the one for hydrogen, in view of testing CPT invariance at the level of about 1 part in 10^{15} .

In a first phase of the experiment (2000 - 2001) we will study the formation rate of antihydrogen atoms as function of temperatures and densities of the antiproton and positron plasmas. No attempt to capture antihydrogen will be done. A first test run is foreseen for July 2000. In the second phase of the experiment (2002 - 2004) the neutral antihydrogen will be captured in a magnetic trap for precision spectroscopic measurements. The experimental setup for the first phase consists of two main parts:

- a) The apparatus to collect antiprotons and positrons and bring them in close contact to produce antihydrogen. This part is briefly described in the Sec. 6.1.
- b) The annihilation detector that will monitor the number of produced antihydrogen atoms. Our institute has the main responsibility for the design and construction of this detector. The detector elements and electronics are described in more detail in Sec. 6.2.

6.1 Production of antihydrogen

The apparatus to produce antihydrogen is presently being assembled in the AD hall at CERN. It consists of a superconducting solenoid (3 T) with a cold bore to house the antiproton capture trap, the positron storage trap, and the recombination trap.

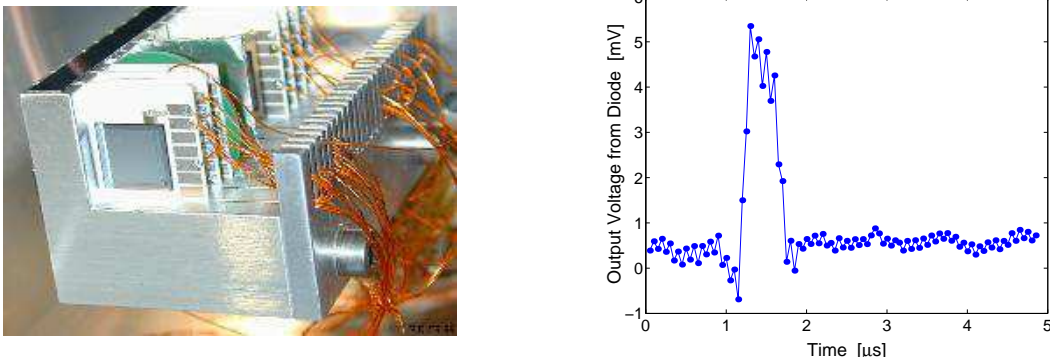


Figure 6.1: *Left: Beam telescope consisting of 6 silicon diodes. The 6 micron thick diodes have an active area of 1 cm^2 ; right: Signal amplitude produced by a bunch of slow antiprotons ($100 \text{ MeV}/c$) going through one of the Si diodes. Note the small noise level, which was not obtained in a clean laboratory environment, but in a noisy accelerator hall!*

Antiprotons were extracted from the Antiproton Decelerator (AD) for the first time in November 1999. We designed a telescope to monitor the beam, consisting of ultra thin

(6 μm) silicon diodes obtained from SINTEF, Norway (fig.6.1). The small signal from a bunch of antiprotons (extracted within 200 ns) could be identified unambiguously by the diodes. Multiple scattering in these thin diodes is negligible, making them ideal to be used as beam counter in the apparatus. Unfortunately, the beam was still too divergent to be transported to the antiproton trap.

The configuration of the electromagnetic field in the antiproton trap is similar to the one for a Penning trap. The antiprotons are confined in the radial direction by the magnetic field of the solenoid and in the axial (z) direction by an electric quadrupole field produced by cylindrical electrodes. The positrons from a strong ^{22}Na source will be accumulated in a similar Penning trap. From these traps the particles will be transported by electrical fields to the recombination trap, which consists of a series of coaxial cylindrical electrodes with alternating electric fields (fig.6.2).

The loading, storage in a Penning trap and dumping of an electron plasma was studied in a test setup, called MINERVA (see ref.[2] for details). The signal amplifiers of the pickup electrodes (Faraday cups) were built in the electronics workshop of our institute. Several voltage dividing and switching schemes were studied. The setup was controlled by a PC running a LabView DAQ program. The results of these tests are now used for ATHENA, where currently the antiproton trap is tested with electrons.

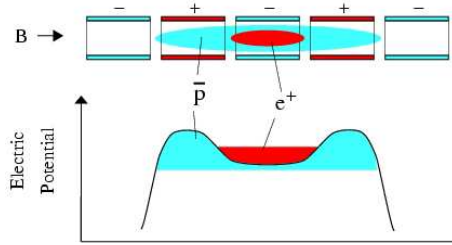


Figure 6.2: *The recombination trap is a nested Penning trap which brings the antiprotons and positrons in close contact for a time sufficiently long to allow the formation of antihydrogen.*

6.2 Annihilation detector

Once antiprotons and positrons have been recombined, the confinement by electric forces ceases, causing the antihydrogen atoms to escape, to hit the trap wall and to annihilate. The unambiguous proof of antihydrogen formation will be obtained by detecting antiproton annihilation products in time coincidence with the two back-to-back 511 keV photons from e^+e^- annihilation.

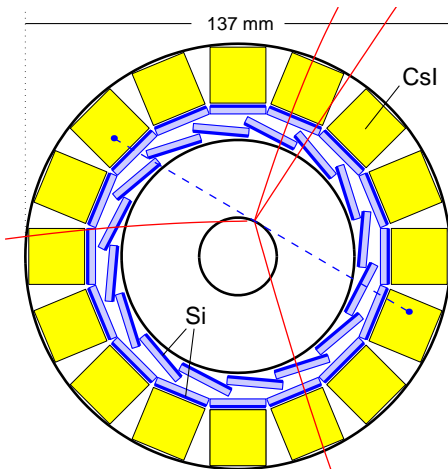


Figure 6.3: *Front view of the ATHENA annihilation detector showing a Monte Carlo simulation of an antihydrogen atom annihilating into pions (solid lines) and into two back-to-back 511 keV photons (dashed lines). The pions are detected in the two layers of silicon microstrip detectors and the 511 keV photons in the CsI crystals. The two fired crystals and the reconstructed annihilation vertex should lie on a straight line, an important requirement to reduce background.*

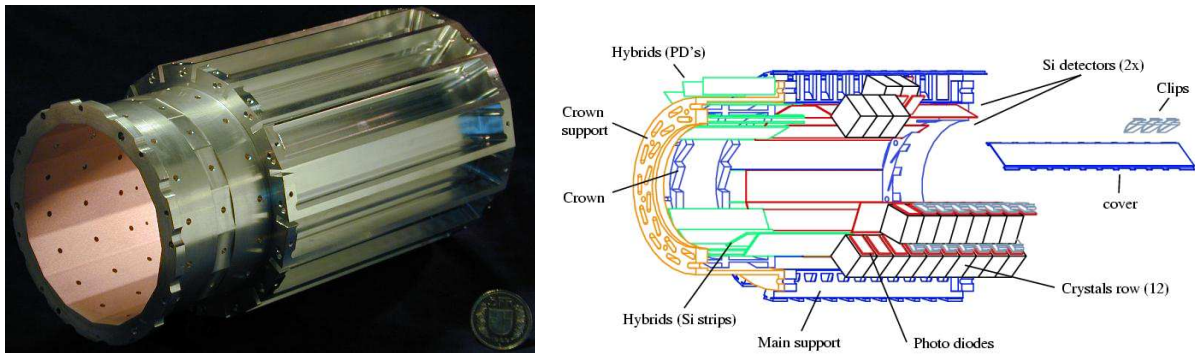


Figure 6.4: *Left: Aluminium support structure of the annihilation detector; right: Cut-away view of the annihilation detector.*

The detector (figs. 6.3 and 6.4) consists of two parts: Two cylindrical layers of 16 silicon microstrip modules each detect the charged pions stemming from an antiproton annihilation on the wall of the recombination trap or with a rest gas atom. The second part, a cylindrical array of 192 pure CsI crystals, will detect the 511 keV photons from e^+e^- annihilation.

The mechanical structure holding the silicon microstrip modules and the CsI crystals (fig. 6.4) was machined from one block of aluminium in the mechanics workshop of our institute. The inner wall of the support structure had to be as thin as possible to minimize multiple scattering and γ conversions. After premachining the inner part of the aluminium block, the final precise shape of the inner surface was achieved by electroerosion at Helefil, France.

Since the recombination trap works at very low temperature (< 1 K) the surrounding annihilation detector cannot operate at room temperature. In 1998 (see the previous annual report) we demonstrated that the silicon microstrips and the amplifiers work at liquid nitrogen temperatures (77 K). The detection of the 511 keV photons with pure CsI crystals at 77 K was also demonstrated with photomultipliers [3]. In 1999 the next step from the prototype to the complete detector design was made. Details are given in the following subsections.

6.2.1 Silicon microstrip detector

The silicon wafers (fig. 6.5) containing the microstrip detector modules were produced by SINTEF, Norway. The wafers also included especially designed UV-sensitive photodiodes to be used for the readout of the CsI crystals (next subsection).

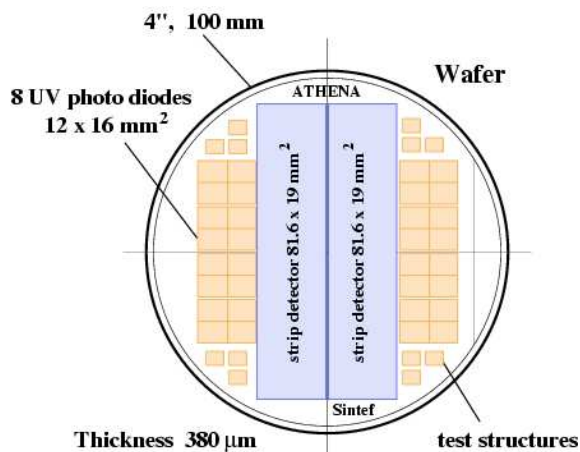


Figure 6.5: *Top: Static tests on the probe station; left: Silicon wafer layout of 2 double sided strip detectors and 8 photo diodes with extremely thin entrance windows (UV-sensitivity).*

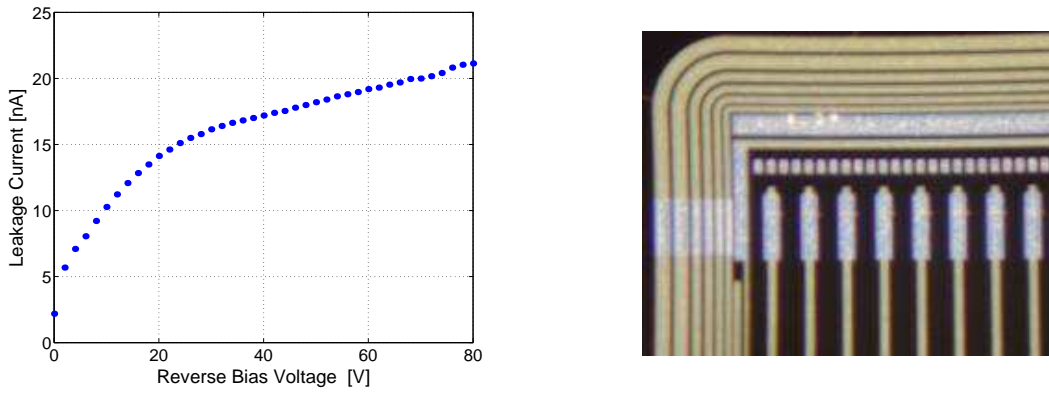


Figure 6.6: *Left: I - V curve of a strip detector measured on a probe station; right: Detail of the front side of the microstrip detector showing the multiple guard ring structure and the bond pads at the end of each readout strip.*

Each strip detector has an active area of $18.1 \times 80.2 \text{ mm}^2$ and a thickness of $380 \mu\text{m}$. The front side is divided into 384 strips with a pitch of $47 \mu\text{m}$ (measurement of the azimuthal angle ϕ), but every third strip only is connected to the readout electronics. The charge collected by the floating strips induces a signal on the readout strips by capacitive coupling. A multiple guard ring structure around the strips (fig. 6.6) ensures low leakage current and a good stability against breakdown. The back side contains 64 pads with a pitch of 1.25 mm. The pads are perpendicular to the strips (measurement of the z coordinate along the detector axis).

Static tests of the silicon microstrip detectors and photodiodes were done using our newly acquired probe station and standard laboratory equipment controlled by a Macintosh computer running a LabView DAQ program (see ref. [4] for details). The performances (leakage current, breakdown stability, functionality of guard rings and depletion voltages) exceeded in general our design expectations.

6.2.2 CsI Crystals

The positron annihilation detector consists of 16 rows of 12 CsI crystals. The crystal dimensions are $13 \times 17.5 \times 17.5 \text{ mm}^3$ giving a total length of 16 cm in z direction. Tests with crystals from various suppliers using different polishing and wrapping methods were done at Pavia [5]. The crystals were directly coupled to Hamamatsu S3590 photodiodes (quantum efficiency 37 %) without grease. From these tests CHRISMATEC was chosen as supplier and 220 crystals were delivered.

For optimum light output we designed a special photodiode optimized for the 350 nm UV light from pure CsI crystals at 77 K. The quantum efficiency is expected to exceed 90 %. To reduce costs the photodiodes were produced on the same wafers as the microstrip detector (see fig. 6.5). Results from test diodes obtained from SINTEF are very promising. For 511 keV photons a resolution of 9.4% was obtained (fig. 6.7). The light output of the crystals produces 28,000 photoelectrons/MeV in the photodiode. This number was obtained from the position of the 511 keV peak in the spectrum and from an absolute calibration of the photodiode using the 22 keV photons from a ^{109}Cd source. It is in agreement with a first estimate obtained from measurements with photomultipliers [3]. As expected, the light output increases with decreasing temperature down to 120 K (fig. 6.7). However, below 120 K it decreases again and at 77 K the light yield is only 55 % of the maximum yield at 120 K. This behaviour is not understood yet. Measurements with Hamamatsu photodiodes and

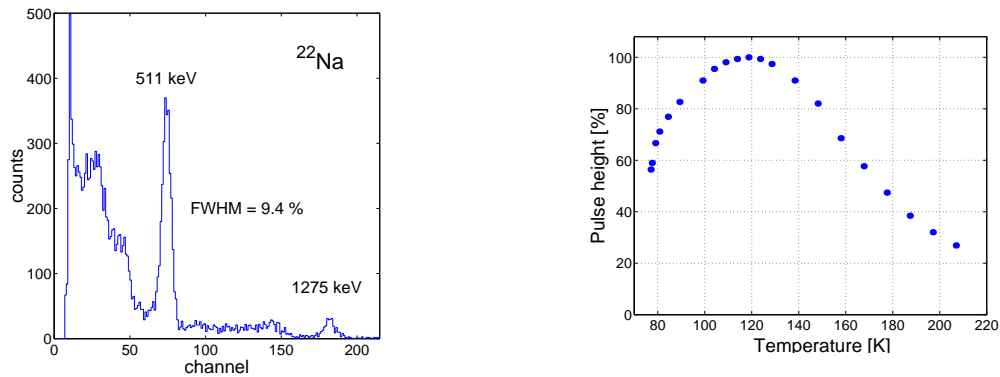


Figure 6.7: Left: Spectrum of a ^{22}Na source measured at 120 K; right: Pulse height of 511 keV γ 's as function of crystal temperature.

photomultipliers show that the light yield does not decrease significantly ($\leq 10\%$) between 120 K and 77 K.

6.2.3 Electronics

To increase the solid angle for detection, two silicon strip modules are connected. The total active length is then 160.4 mm. The backplanes of the modules are glued to a silicon structure which holds at the same time the transmission lines for the 128 pads. A prototype of this fragile structure was successfully cooled down to 77 K without any noticeable deformation. The two modules are connected to the VIKING type (VA2_TA) readout chips [6] mounted with passive electronics on a small ceramic hybrid (see fig. 6.8).

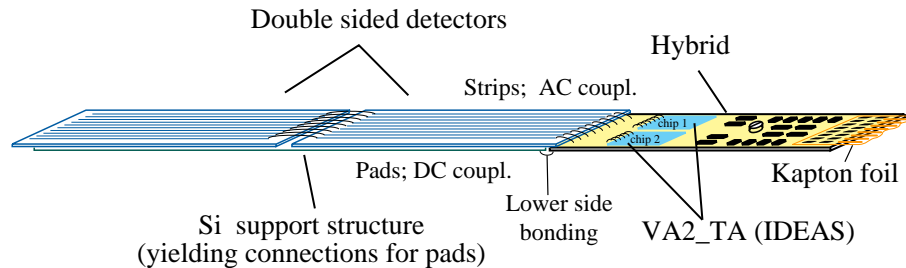


Figure 6.8: A microstrip module consists of two connected detectors with 128 readout strips (total length 160 mm) and 128 pads.

A similar readout system is used for the photodiodes. Photodiodes are segmented into four sections covering a total active area of $12 \times 16 \text{ mm}^2$. The 48 readout lines of a crystal row are connected to one VA2_TA chip on a PCB hybrid.

The self-triggering VA2_TA chip is multiplexing its 128 channels into one analog output line. The two VA2_TA chips on the hybrid of each microstrip module are connected to the outside electronics through only 33 lines which provide e.g. the symmetric analog output of the 256 channels, a symmetric trigger output, bias, digital and analog control signals and supply voltages. Custom designed capton cables connect the 48 hybrids (2×16 for the 2 silicon layers and 16 for the crystals) with the patch panel (fig. 6.9). This circular PCB board works as a passive fan-in for common signals and collects analog signals to the corresponding cable bundles. The patch panel is connected to the outside electronics through 250 coaxial cables

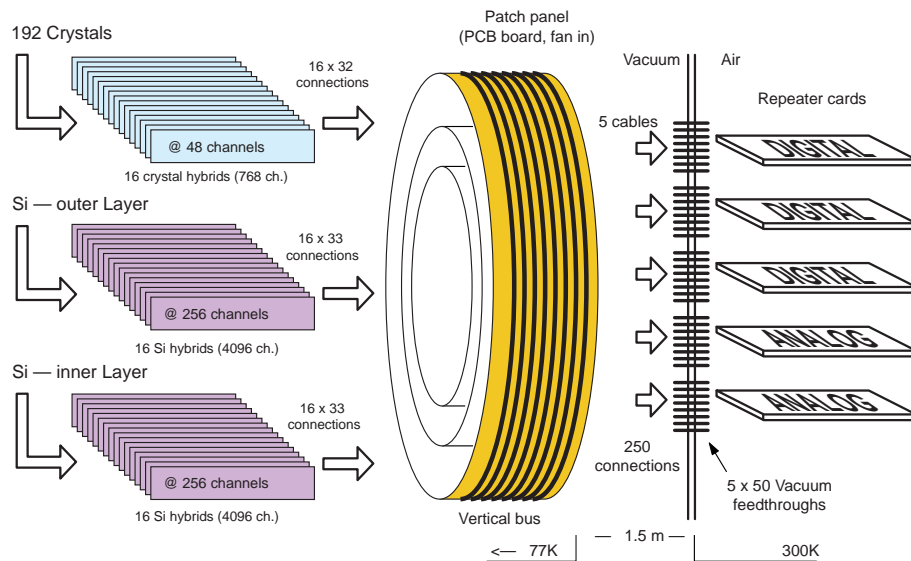


Figure 6.9: *Block diagram of the readout electronics.*

and five vacuum feedthrough connectors (50 pin D-Sub type). We designed this complex system of electronics and cables in vacuum at 77 K by using our previous experience with the similar but much simpler Crystal Barrel silicon microstrip vertex detector [7].

Beyond the vacuum flange the signals are processed by two analog repeater cards which were designed and assembled with the help of the electronics workshop of our institute. The digital repeater cards were designed at Pavia. The analog signals from the repeater cards are digitized by 36 VME FADC modules. The readout system is controlled through a fast VME-PCI link by a PC running a LabView DAQ program. We developed this system for the silicon microstrip beam telescope used in the CMS pixel test experiment (see last year's annual report).

The detector will be assembled and mounted in the ATHENA magnet in spring 2000. A first run with antiprotons and positrons is foreseen next summer.

References

- [1] ATHENA proposal, CERN SPSLC 96-47, see <http://www.cern.ch/athena/>.
- [2] M. Zwahlen, Diplomarbeit, Universität Zürich (2000).
- [3] P. Niederberger, Diplomarbeit, Universität Zürich (1999).
- [4] R. Brunner, Diplomarbeit, Universität Zürich, in preparation.
- [5] A. Rotondi, ATHENA internal note, Feb. 1999.
- [6] O. Toker et al., Nucl. Instr. Meth. A 340 (1994) 572, (the new VA2-TA chip, is produced by IDEAS, see <http://www.ideas.no/>).
- [7] C. Regenfus, Nucl. Instr. Meth. in Phys. Res. A 386 (1997) 60.
C. Regenfus et al., Nucl. Instr. Meth. in Phys. Res. A 412 (1998) 70.

7 Particle Physics at DESY/HERA (H1)

S. Egli (until August 1999), I. Foresti, S. Hengstmann, M. Hildebrandt, N. Keller,
 P. Robmann, F. Sefkow, U. Straumann, P. Truöl,
 S. von Dombrowski (until July 99), R. Wallny and T. Walter

in collaboration with:

Institut für Teilchenphysik der ETH, Zürich (R. Eichler, W. Erdmann, C. Grab, M. Hilgers, H.-C. Kästli, B. List, S. Lüders, and A. Schöning), Paul-Scherrer-Institut, Villigen (S. Egli (since September 1999), K. Gabathuler, J. Gassner, and R. Horisberger), and 34 institutes outside Switzerland

(H1–Collaboration)

7.1 Electron proton collisions at 300 GeV center of mass energy: overall status of the project

During the first part of 1999, until the end of April, the HERA electron/positron-proton storage ring operated with electrons. A total luminosity of 14 pb^{-1} was accumulated. After a short shutdown, during which also minor repairs on the central silicon tracker (CST) were carried out, the preaccelerators were tuned again for positrons and until the end of 1999 a luminosity of 20 pb^{-1} was available for physics analysis. The run continued with positrons after the christmas break and will only end in September 2000. The big shutdown originally planned for May 2000 has been delayed by four months to let the HERA-B experiment take first physics data, and also adapt for delivery delays of various components needed for the upgrade of HERA, the H1- and the Zeus-experiment. As can be projected from the statistics given in Table 7.1 the available event samples at the end of this run should be about three times larger than what is being used in our publications, which include up to 1997 data.

Table 7.1: *Summary of HERA and H1 operation during the last eight years.*

Parameter	e^-p			e^+p				
	1993/4 1998	1999	Sum	1994 -1997	1999	2000 ^[a]	Sum	
Integrated luminosity \mathcal{L}								
HERA produced	[pb^{-1}]	10.6	17.7	28.3	68.5	27.3	25.9	121.7
HERA physics	[pb^{-1}]	9.8	16.8	26.6	64.3	25.7	24.6	114.6
H1 taken	[pb^{-1}]	7.6	15.1	22.7	49.3	22.3	20.7	92.3
H1 physics	[pb^{-1}]	5.7	14.2	19.9	44.2	20.9	19.6	84.7
HERA efficiency	[%]	92	95	94	94	94	95	94
H1 efficiency	[%]	58	85	75	69	82	79	74
Average luminosity	[$(\mu\text{b s})^{-1}$]	2.13	3.77	3.15	3.41	4.21	5.48	4.03
Peak luminosity	[$(\mu\text{b s})^{-1}$]	8.8	12.1	12.1	10.1	12.6	17.9	17.9
Average p current	[mA]	55.4	74.8	67.5	65.6	83.1	82.8	73.2
Average e^\pm current	[mA]	14.4	18.8	17.2	24.0	20.2	23.3	23.0
HERA luminosity runs		521	179	700	1132	244	142	1518
Permanent H1 runs	[10^3]	7.1	2.5	9.6	15.0	3.7	2.7	21.4
Average duration	[min]	17	29	20	21	26	26	22

^[a]: until April 16, 2000

Since the 1998 data sample is small, and analysis of the 1999 run still in progress, it is the pre-1998 data on which the 16 publications ([1]-[16]) of the collaboration are based. The following principal areas are covered:

- neutral and charged electroweak current cross sections, proton structure functions and parton densities at high momentum transfer Q^2 [12],
- search for states outside the standard model [5, 14],
- photon structure [1, 10, 15],
- parton-fragmentation into multijet final states [3, 6, 9, 13],
- electroproduction of exclusive final states [8, 11], and
- production of heavy quark-antiquark states, of open charm and beauty [2, 4, 7, 16].

We will report below on the analyses in the heavy quark sector (Section 7.4.2) and on the QCD analysis of low Q^2 structure functions (Section 7.4.1), two areas, where there is manifest activity of the University of Zürich group.

Besides the physics analysis, our activities deal with the maintenance, monitoring and calibration of the detector components built in Zürich for the central tracker and the first level trigger of H1. Last year the integration of the CST [17] into the central tracker analysis was of particular importance. The relative alignment of the individual detector ladders within the CST as well as the relative alignment of the CST within the central drift chambers has been finalized to such an extent, that secondary vertices can be searched for in heavy flavour physics analysis. In the course of improving the central tracker codes the central inner z -drift chamber (CIZ) has been recalibrated, too, and its resolution considerably improved. Further details are given in Section 7.4.2.

Most of our effort, however was directed towards our contribution to the upgrade program of the H1-detector.

7.2 Summary of activities related to the H1-upgrade

The investigation of rare processes at the limits of the kinematically accessible range at HERA requires a luminosity upgrade of the machine [18]. The most important aspect of this program is the improvement of the focussing properties near the interaction region of the H1 detector. The luminosity is expected to increase by a factor of seven to $L = 7.4 \times 10^{31} \text{ cm}^{-2}\text{s}^{-1}$.

Part of the H1 upgrade plan [19] is the replacement of the existing inner two proportional chambers (CIP) and the inner drift chamber (CIZ) by a new five-layer proportional chamber. The aim of this change is to improve z -vertex triggering and track reconstruction at the trigger level, as well as the rejection of background events. In order to achieve this the number of readout channels both along the z -axis and in azimuthal direction has to be increased. Furthermore implementing five chambers instead of two will provide redundancy and help to resolve ambiguities from the CST. The new CIP will have pad readout in 16 azimuthal sectors. The trigger scheme is based on a projective geometry of the pads along the z -axis, thus requiring a varying number of pads in each layer ranging from 119 to 93 pads for the innermost and outermost layer, respectively. The increased number of readout channels also requires new readout and trigger electronics.

The project is being coordinated by the University of Zürich with ETH Zürich and University of Heidelberg as partners. The ASIC laboratory in Heidelberg develops the amplifier and readout chip CIPix, and the electronics for trigger and data acquisition is a common Heidelberg and Zürich University effort. ETH Zürich is responsible for all components dealing

with the readout of the data at the detector end, and the transport to the electronic trailer via an optical transmission line with drivers and receivers at either end.

The University of Zürich is also responsible for the mechanical design and construction of the multiwire proportional chambers. The high density of readout channels and new front-end electronics made it necessary to build a cylindrical prototype of the chamber closest to the beam for which the space limitations are critical. The construction of this prototype at 1/3 of the full length was finished in July 1999. The construction of the full-length five-layer chambers started in autumn of 1999 and should be completed early 2001 to be ready for the installation in the H1 detector at the end of the HERA shutdown. Further details are given below in Sections 7.3.1 and 7.3.2.

7.3 Construction of the new CIP

7.3.1 Mechanics

The active gap and the length of new CIP will remain unchanged compared to the existing chamber [20] with 6 mm and 2190 mm, respectively. 480 gold plated tungsten wires, 25 μm in diameter, per plane span the full length, but are supported at two points by two glasfiber epoxy rings. The cathode planes are made of Kapton foil coated with graphite on the front (chamber side, surface resistance 500 $[\text{k}\Omega/\text{sq.}]$) and supporting 5 μm thick copper pads on the back side. The pads are between 18 mm (inner chamber) and 23 mm (outer chamber) wide and divide the circumference of the cylinder into 16 ϕ -sectors. Each pad is contacted from the $-z$ side via a coaxial cable embedded into Rohacell cylinders. This is shown in Figure 7.1. The Rohacell/foil sandwiches and the glasfiber epoxy flanges at the end provide the basic strength and structure for the chamber. Cutting and preparing 8500 cables of individual length and soldering them at each end is the most time consuming part of the construction.



Figure 7.1: *Construction of the cathode plane for the innermost chamber of CIP on the steel mandrils. Seen here are the flange at the $-z$ end from which the coaxial cables fan out to the approximately 1500 cathode pads. The cables are embedded into a Rohacell cylinder.*

The whole package requires four cylinders, which have a cathode readout plane on the inside and a cathode/wire plane on the outside, one cylinder with only a cathode readout plane at the outer radius and one cylinder with only a wire plane closest to the beam. The

first two cylinders of this sequence have been completed. Most geometrical details were first successfully tested with an one-third length full diameter prototype (see Figure 7.2). It continues to serve for tests of the on-chamber electronics and the readout chain.



Figure 7.2: *The one-third full length prototype of the new CIP being tested in the laboratory.*

7.3.2 Electronics

The signal readout chain starts on the chamber with the CIPix amplifier chip [21] derived from the HELIX chip [22], which was developed for the HERA-B microstrip gas chambers. The chip contains an integrating preamplifier and shaper for 64 channels, which is followed by a discriminator with a programmable threshold. The digital signals are synchronized with the HERA 10.4 MHz clock and multiplexed fourfold at the output. The analog signal of one channel (programmable) can also be inspected. The programs are loaded via a standard I²C interface. A small series of prototypes from a multiproject wafer was already available for testing. Figure 7.3 shows CIPix signals recorded with a β source in September 1999 on the CIP prototype. The characteristic Landau-distribution of the pulse height and the exponential dependence of its average on chamber voltage has been verified.

In January 2000 the complete readout chain including the optical transmission line with drivers, 40 m cable and receiver was assembled and has been tested. The digital functions of the CIPix chip are sufficiently well understood, such that final submission could be made.

In the electronics trailer the digital signals from the optical transmission line are handled by one receiver card for two ϕ -sectors. A trigger card deals with all five planes of a given ϕ -sector. The signals are transmitted from the receiver card to the trigger card via the CIP backplane (see Figure 7.4), which requires a rather complicated layout, but does not contain active elements. Four ϕ -sectors require one VME crate, the whole system hence four crates.

All the high level functionality of the system resides in the trigger cards, i.e. the track finding algorithms, the reconstruction of the track origin along the beam axis and the z -vertex histogramming. They contain a complete data acquisition system for all digital signals including a 32 bunch crossing deep pipeline, and the control logic for the VME readout, which requires less than 400 μ s. For the first time in a particle physics experiment the whole system is implemented using a new type of FPGA (field programmable gate array, type APEX

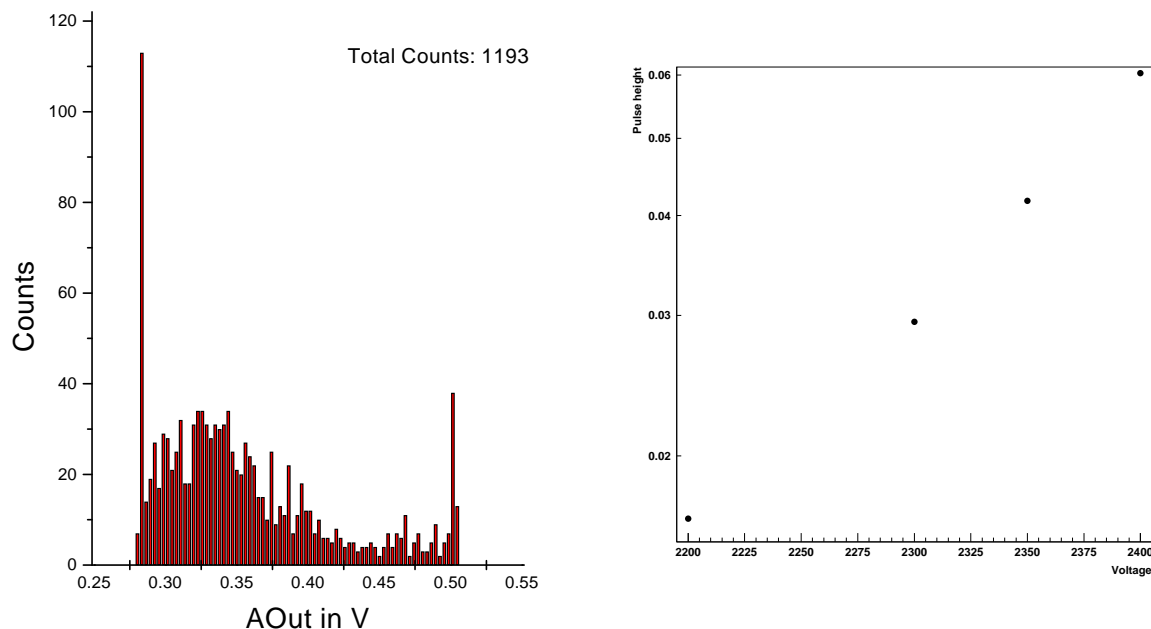


Figure 7.3: *Left: pulse height distribution measured with a $^{106}_{44}\text{Ru}$ (β^- source) and the CIPix amplifier on the chamber prototype. Right: average pulse height in function of chamber voltage.*

20K400 from ALTERA, available since mid 1999). With up to 500 inputs and outputs, and a large amount of configurable memory aside from the usual logical elements, the use of these circuit elements will allow to build rather complex and still fast trigger systems in the future. Since October 1999 a first, reduced prototype has been in use for tests with different trigger algorithms. The first complete prototype is presently being tested in Heidelberg.

The details of the auxiliary electronics for the distribution of the trigger control signals, HERA clock distribution and control of phase stability with respect to this clock, summation of histograms and production of trigger elements have not been fixed, but the development is in progress.

So far most of the development tasks on the trigger project have been the subject of diploma theses at the University of Heidelberg supervised by U. Straumann. The same holds for the integration of the new system into the existing H1 online system, for which commercial VME processors and VME crate interconnects are foreseen.

7.4 Results from recent analyses

7.4.1 Determination of the gluon density and the strong coupling constant α_s

The measurement of inclusive differential cross sections in ep scattering at HERA provides data for the most complete and accurate test of the dynamics of the strong interaction (QCD) in its perturbative regime. The analysis of the data proceeds in two steps: First the cross section is determined in bins of E'_e , the energy of the scattered electron, and θ , the scattering angle in the laboratory system. Then these data points are fitted with the QCD evolution equation [23] as a function of the Bjorken scaling variable x and the invariant momentum transfer Q^2 , resulting in quark and gluon momentum density distributions and the value of the strong coupling constant.

The first step requires detailed understanding of the detector response. Among other con-

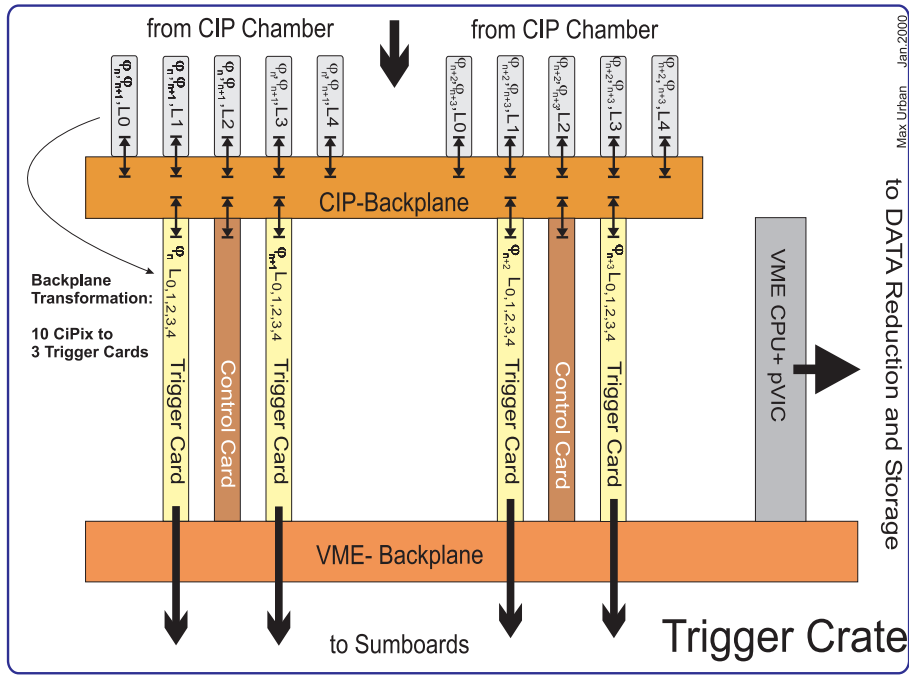


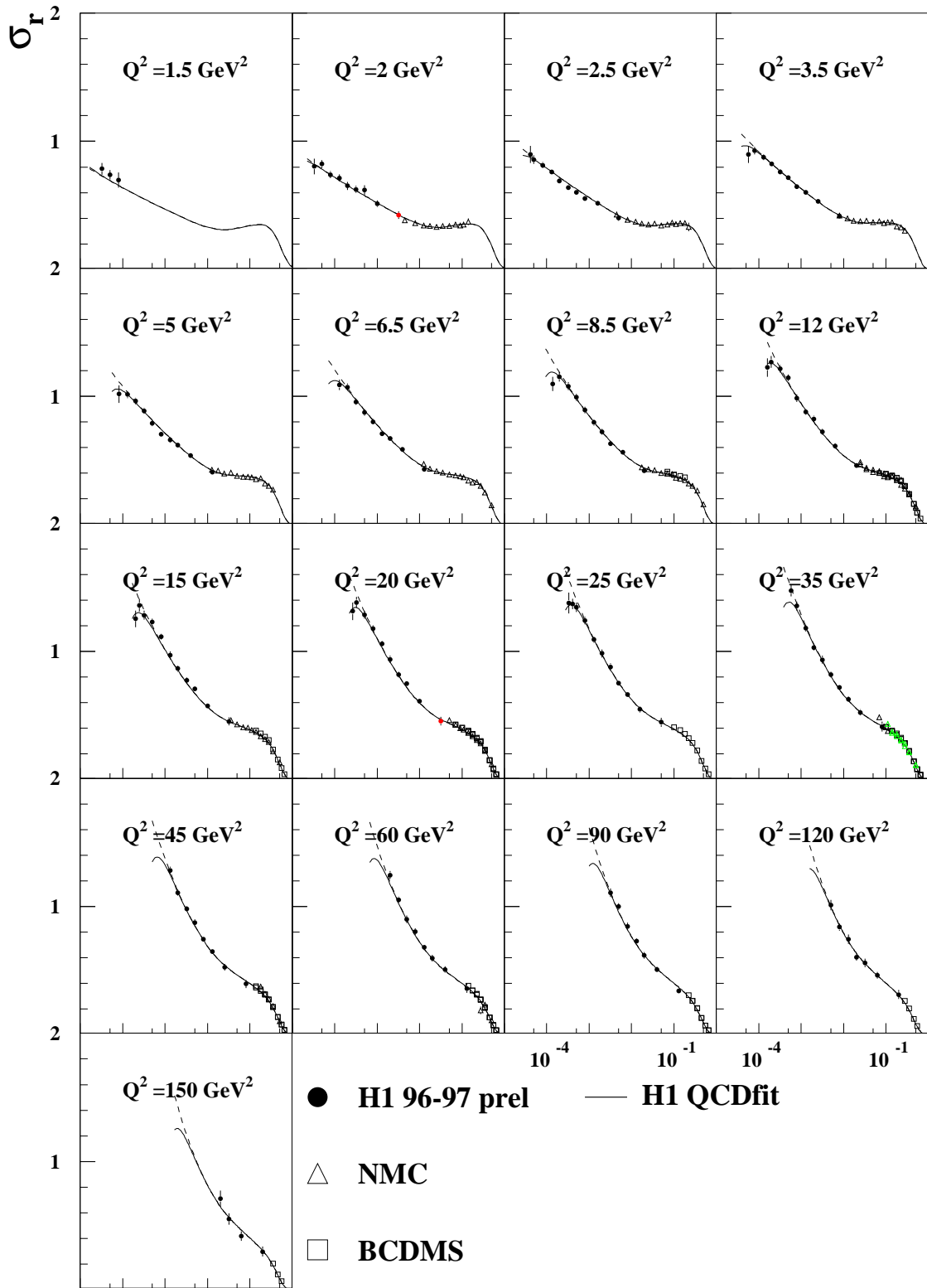
Figure 7.4: Components for trigger and data acquisition contained in a trigger card, which serves four ϕ -sectors. The custom made CIP backplane resides in the lower part of the crate. The receiver cards are connected to the back side, and the control cards to the front side of this plane. The upper part of the crate contains the standard VME-bus for data transfer, control and monitoring.

tributions the energy calibration, and the event vertex determination accuracy and efficiency contribute most to the final systematical uncertainties.

Especially difficult is the region, where the electron is only weakly scattered (θ close to π) and is detected in the backward drift chamber (BDC) and the lead - scintillating fiber calorimeter (SPACAL). Both the energy calibration and the determination of the scattering angle by the BDC is spoiled by the fact, that there is a lot of dead material distributed very inhomogeneously in front of these detectors. The thesis project of R. Wallny contains extensive Monte Carlo simulations and comparison to experimental data, which allowed to determine reliable systematical uncertainties in this area. In his diploma work P. Sievers studied different possibilities to correct the energy response of the SPACAL by making use of the charge measurement from the electron showers in the BDC.

Since data taking at very low Q^2 is difficult, due to the overwhelming rate of electron and proton beam induced background in this domain of low electron energy loss and high θ , 1.8 pb^{-1} of luminosity were taken in a special period in autumn 1997 using a dedicated trigger. R. Wallny was the driving force behind this run. He prepared the special trigger conditions, monitored the data quality and adapted the trigger conditions, if necessary.

The second step consists of a QCD evolution analysis in the variables x , Q^2 , described by the DGLAP equations [23] in next-to-leading order perturbation theory [23]. Since these equations do not describe the gluon and quark distributions ab initio, assumptions at a given scale Q_0^2 about the shape of these distributions as a function of x have to be made. Since the cross section below $x \approx 10^{-2}$ is dominated by electrons scattered off quarks virtually generated from gluons, this domain is specially sensitive to the gluon distribution. The higher x region is mainly sensitive to the valence quark distributions.



X

Figure 7.5: Reduced cross sections σ_r (measured cross section with the trivial kinematical factors divided out) as a function of the Bjorken scaling variable x for different Q^2 . The H1 data are compared to data from fixed target μp scattering [24, 25]. The solid line represents the QCD fit based on the H1 data alone.

In the present analysis also results from NMC [24] and BCDMS [25] are being considered in addition to the H1 data. The analytic form of the parametrisation of the initial parton distributions, the scale Q_0^2 and the coupling constant α_s are varied. Since it is not known, down to what value of Q^2 the perturbative approach of QCD is valid, and since in addition the systematical uncertainties at low Q^2 in all experimental data considered are least well known, all data points below an additional parameter Q_c^2 are not included in the fit. The goal is to find a set of the unphysical parameters Q_0 and Q_c , with which the fit result (the χ^2 distribution) does neither depend on these parameters nor on the experiments included in the fit. Then the fit may give results on the shape of the parton distributions and on the values of α_s .

As an example of such an analysis, Figure 7.5 shows the data points of all three experiment for different Q^2 with the fit superimposed. For the latter only H1 data are used in this case. The fit demonstrates the consistency of the H1 data with those from the other experiments. At very low x and intermediate Q^2 a change in the shape of the cross section can be observed. This is the region, where longitudinally polarized photons start to play a significant role. Figure 7.6 shows the gluon momentum density distributions extracted from this fit for different Q^2 .

It is interesting to note, that in contrast to earlier analyses it was not necessary to use deuteron data to pin down the different valence quark distribution, because the accuracy of the H1 data is now sufficient. The momentum sum for all partons has been required in the fits, the resulting total momentum fraction carried by the gluons is about 46%.

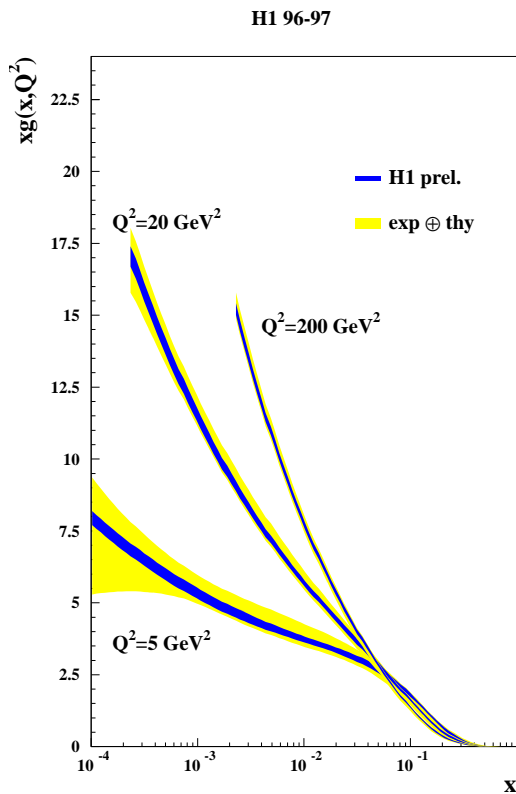


Figure 7.6: *The momentum distribution function of gluons in the proton as observed by ep scattering with different Q^2 , and obtained from the results of the QCD fits to the inclusive electron scattering data. The error bands include statistical errors (dark), and uncertainties due to variations of the parameters Q_0 , Q_c , α_s , the charm mass as well as uncertainties coming from different parametrisation forms of the light parton distributions.*

7.4.2 Photo- and electroproduction of charm quarks

Heavy flavour physics at HERA focuses on aspects related to production dynamics rather than weak decays and mixing angles. Heavy quarks – like jets – reflect the properties of hard sub-processes in ep interactions. Their mass provides the natural scale which allows the application of perturbative methods in QCD and also testing the theory in regions where no other hard scale (like high transverse energy) is present. Furthermore, when probing the structure of matter, heavy quarks single out the gluonic content.

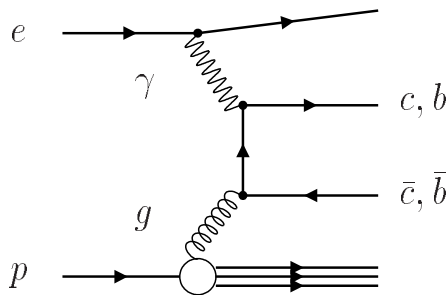


Figure 7.7: *Boson gluon fusion.*

In QCD, c and b production in ep collisions proceed mainly via the boson gluon fusion diagram shown in Figure 7.7. Therefore, charm production has already in the past offered a way to determine the gluon density in the proton. At HERA, this has been performed at low values of the momentum fraction x where the gluon density is steeply rising [2]. The results, which have been reported here earlier, complement the scaling violation analysis of inclusive structure function data [26] and demonstrate the universality of the parton distribution. The concept is also being applied to probe the dynamics of diffractive scattering, mediated via colorless exchange. In a partonic interpretation of the exchanged object (the “Pomeron”) charm production is sensitive to its gluon content. The differential cross section data (thesis S. Hengstmann) still have large, mostly statistical, uncertainties, but they have started to discriminate between different theoretical approaches [27] (see last year’s report).

In all these studies open charm is detected in the “golden” decay channel $D^{*+} \rightarrow D^0 \pi^+$ followed by $D^0 \rightarrow K^- \pi^+$ which has a favorable signal-to-background ratio, but its fragmentation and decay fraction is only 0.7%. Consequently, not only the diffractive results are statistically limited so far, and important aspects of the theoretical picture in next-to-leading order (NLO) QCD could not yet be addressed. In order to probe the theory beyond the tree level and to measure effects which are absent in leading order (LO), like transverse momentum imbalance or acoplanarity of the produced quark-antiquark pair, both charm quarks need to be tagged. In photoproduction, such “double tags” would allow to clarify the mechanisms of so-called resolved contributions which are still under theoretical debate.

Furthermore higher tagging efficiencies are also needed to explore otherwise inaccessible regions of phase space. It has not yet been possible to measure with sufficient precision the charm contribution to the proton structure function F_2 at higher four-momentum transfers Q^2 , where a description in terms of a charm density in the proton – as needed to predict production rates at future colliders – should be adequate. At high Q^2 and p_t , new opportunities will also arise in charged current processes and in the search for new physics.

What holds for charm, is even more true for beauty. Only the inclusive photoproduction cross section could be determined so far [7]; it is about two orders of magnitude smaller than in the charm case, but larger than expected. The measurements to date rely exclusively on the well established signature of semileptonic decays of b hadrons in jets and the higher

transverse momentum p_T^{rel} of the lepton with respect to the jet direction, due to the higher b mass.

The long lifetimes of charm and beauty hadrons which can be measured with micro-vertex detectors provide an independent signature, With its CST the H1-collaboration is for the first time pursuing this direction at HERA.

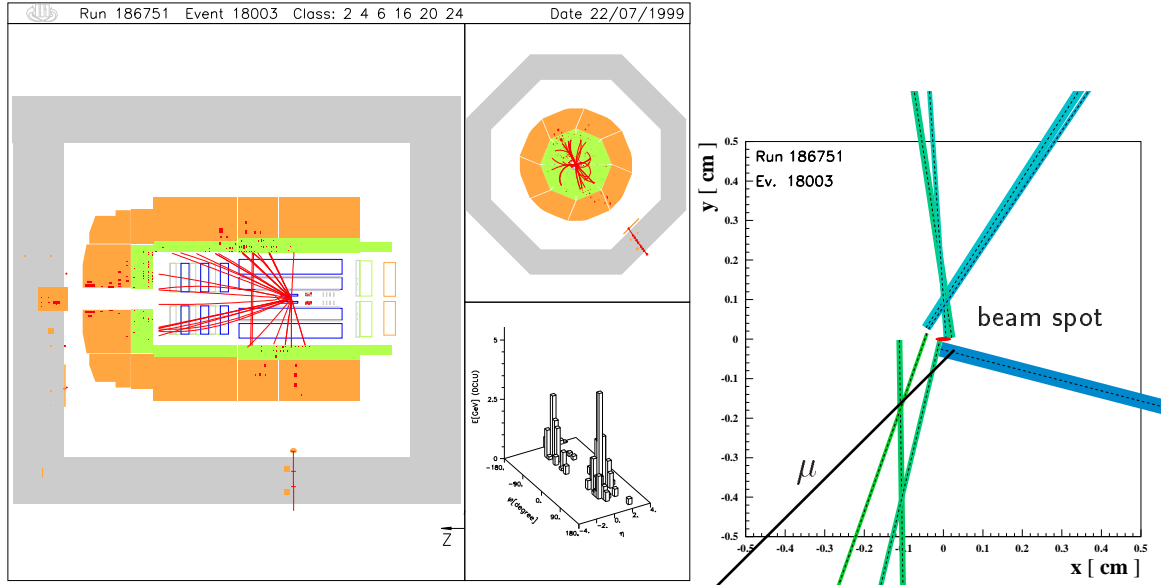


Figure 7.8: A candidate event for beauty production with subsequent semi-muonic decay. In the magnified view perpendicular to the beam (on the right-hand side) the tracks measured in the CST are represented as bands with widths corresponding to their $\pm 1\sigma$ precision.

We show here one example from an on-going study (thesis J. Kroseberg) where charm and beauty quarks are identified by means of their semileptonic decays. An event with two jets and a penetrating track identified as a muon is shown on the left-hand side of Figure 7.8. The muon has a relatively high transverse momentum of $3 \text{ GeV}/c$ with respect to the nearest jet, which is unlikely for muons from charm decays or misidentified hadrons but is expected for decays of b flavoured hadrons, due to their higher mass. In the magnified view perpendicular to the beam (on the right-hand side) the tracks measured in the CST are represented as bands with widths corresponding to their $\pm 1\sigma$ precision. The resolution provided by the CST reveals that the muon track originates from a well separated secondary vertex. The distribution of impact parameters, defined as the distance of closest approach between the muon tracks and the interaction vertex, signed positive when the intercept of the track with the jet axis lies behind the interaction vertex (along the jet direction), and negative otherwise, is plotted in Figure 7.9. Positive impact parameters are a signature of decays of short-lived particles, and the clearly visible asymmetry of the distribution provides a measure of the charm and beauty content of the event sample. This analysis is a pioneering project which could become one of the first physics results obtained with a Silicon vertex detector at HERA. The work therefore presently has an emphasis on technical aspects and involves the development of track reconstruction software and analysis tools.

The lifetime signature is in principle present in every event and has in fact been exploited successfully as heavy quark tag with highest efficiency in many other experiments to-date. The b -enriched sample and the clear event topology of the muon analysis provide an optimal testing ground for such techniques. The extension to the general case including hadronic

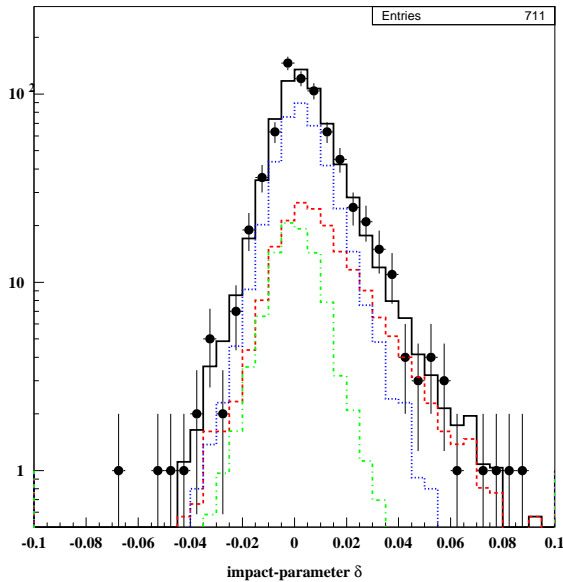


Figure 7.9: *Impact parameter distribution for muon candidate tracks in di-jet events. The histogram is the superposition of Monte Carlo predictions for $b\bar{b}$ production (dashed), $c\bar{c}$ production (dotted), and mis-identified hadrons (dash-dotted).*

decays is presently being studied using Monte Carlo simulations (thesis I. Foresti). A simple and robust method is to combine the information contained in the impact parameters of all tracks with sufficient momentum, and to derive an estimate of secondary vertex activity in the event.

Not relying anymore on exclusive signatures (like a muon) puts additional strain on the tracking precision requirements, because non-Gaussian measurement errors compete with the low signal-to-background ratio. The full potential of the CST can only be realized with optimized performance and consistency of the entire tracking system. Here, the CST, in turn, together with new numerical methods, provides new handles for calibration and alignment of the outer tracking detectors. A collaboration-wide effort has been initiated to lift the tracking performance to the standards of micro-vertexing methods (F. Sefkow acts as a convener of this new group).

For example (thesis S. Hengstmann), it has now become both necessary and possible to achieve higher precision in the central inner z -chamber (CIZ), built at our institute. Optimal track precision in the z direction is important to minimize the wrong assignment of noise hits from the CST z measurement to track candidates. Using a large sample of cosmic events, correction constants have been determined for each single wire. With such a calibration, the hit resolution has already been improved from $800\ \mu\text{m}$ to $500\ \mu\text{m}$. With precise CST tracks as reference, further corrections can be applied, resulting in a further improvement to $360\ \mu\text{m}$, which is now consistent with the intrinsic resolution of the chamber, as determined from hit triplets. Benefits from such progress can be expected in a large variety of physics applications, ranging from the mostly track-based heavy quark analyses to better reconstruction of event kinematics at very high Q^2 .

References

- [1] *Charged Particle Cross Sections in Photoproduction and Extraction of the Gluon Density in the Photon*,
H1-Collaboration, C. Adloff *et al.*, Eur. Phys. J. **C10** (1999), 363.

- [2] *Measurement of D^* Meson Cross Sections at HERA and Determination of the Gluon Density in the Proton*,
H1-Collaboration, C. Adloff *et al.*, Nucl. Phys. **B545** (1999), 21.
- [3] *Measurement of Internal Jet Structure in Di-jet Production in Deep Inelastic Scattering at HERA*,
H1-Collaboration, C. Adloff *et al.*, Nucl. Phys. **B545** (1999), 3.
- [4] *Charmonium Production in Deep Inelastic Scattering at HERA*,
H1-Collaboration, C. Adloff *et al.*, Eur. Phys. J. **C10** (1999), 373.
- [5] *A Search for Leptoquark Bosons and Lepton Flavour Violation in e^+p Collisions at HERA*,
H1-Collaboration, C. Adloff *et al.*, Eur. Phys. J. **C11** (1999), 447.
- [6] *Measurement of Transverse Energy Flow in Deep-Inelastic Scattering at HERA*,
H1-Collaboration, C. Adloff *et al.*, Eur. Phys. J. **C12** (2000), 595.
- [7] *Measurement of Open Beauty Production at HERA*,
H1-Collaboration, C. Adloff *et al.*, Phys. Lett. **B467** (1999), 156.
- [8] *Forward π^0 -Meson Production at HERA*,
H1-Collaboration, C. Adloff *et al.*, Phys. Lett. **B462** (1999), 440.
- [9] *Di-jet Rates in Deep-Inelastic Scattering at HERA*,
H1-Collaboration, C. Adloff *et al.*, Eur. Phys. J. **C13** (2000), 415.
- [10] *Measurement of Di-jet Cross Sections in Low Q^2 and the Extraction of an Effective Parton Density for the Virtual Photon*,
H1-Collaboration, C. Adloff *et al.*, Eur. Phys. J. **C13** (2000), 397.
- [11] *Elastic Electroproduction of ρ Mesons at HERA*,
H1-Collaboration, C. Adloff *et al.*, Eur. Phys. J. **C13** (2000), 371.
- [12] *Measurement of Neutral and Charged Current Cross Sections in Positron-Proton Collisions at Large Momentum Transfer*,
H1-Collaboration, C. Adloff *et al.*, DESY 99 – 107, hep-ex 9908059, Eur. Phys. J. **C** (2000), in print.
- [13] *Investigation of Power Corrections to Event Shape Variables Measured in Deep-Inelastic Scattering*,
H1-Collaboration, C. Adloff *et al.*, DESY 99 – 193, hep-ex 9912052, Eur. Phys. J. **C** (2000), in print.
- [14] *Search for Compositeness, Leptoquarks and Large Extra Dimensions in eq Contact Interactions at HERA*,
H1-Collaboration, C. Adloff *et al.*, DESY 00 – 027, hep-ex 0003002, subm. to Phys. Lett. **B** (2000).
- [15] *Measurement of Di-jet Cross Sections in Photoproduction and Photon Structure*,
H1-Collaboration, C. Adloff *et al.*, DESY 00 – 035, hep-ex 000311, subm. to Phys. Lett. **B** (2000).
- [16] *Elastic Photoproduction of J/Ψ and Y Mesons at HERA*,
H1-Collaboration, C. Adloff *et al.*, DESY 00 – 037, hep-ex 000320, subm. to Phys. Lett. **B** (2000).
- [17] *The H1 Silicon Vertex Detector*,
D. Pitzl, O. Behnke, M. Biddulph, K. Bösiger, R. Eichler, W. Erdmann, K. Gabathuler, J. Gassner, W.J. Haynes, R. Horisberger, M. Kausch, M. Lindström, H. Niggli, G. Noyes, P. Pollet, S. Steiner, S. Streuli, K. Szeker, and P. Truöl, hep-ex 0002044, subm. to Nucl. Instr. Meth. **A** (2000).

- [18] *ep physics beyond 1999*,
H1 note H1-10/97-531, April 1998.
- [19] *H1 high luminosity upgrade 2000: CIP and level-1 vertex trigger*,
M. Cuje *et al.*, H1 note H1-01/98-539, January 1998.
- [20] K. Müller *et al.*, Nucl. Instr. Meth. **A312** (1992) 457.
- [21] CIPix User Manual: http://wwwasic.ihep.uni-heidelberg.de/h1cip/CIPix_manual/CIPix_UserManual.v1_0.html
- [22] HELIX User Manual: <http://wwwasic.ihep.uni-heidelberg.de/~feuersta/projects/Helix/index.html>
- [23] Yu.L. Dokshitzer, Sov. Phys. JETP **46** (1977) 641;
V.N. Gribov, and L.N. Lipatov, Sov. J. Nuc. Phys. **15** (1972) 438 and 675;
G. Altarelli, and G. Parisi, Nucl. Phys. **B126** (1977) 298.
- [24] NMC-Collaboration: M. Arneodo *et al.*, Phys. Lett. **B364** (1996) 107.
- [25] BCDMS-Collaboration: A.C. Benvenuti *et al.*, Phys. Lett. **B223** (1989) 485.
- [26] H1-Collaboration, S. Aid *et al.*, Nucl.Phys. **B470** (1996) 3.
- [27] S. Hengstmann, Nucl. Phys. (Proc. Suppl.) **B79** (1999) 296.

8 Particle Physics at DESY/HERA (HERA-B)

P. Robmann, S. Steiner, O. Steinkamp, U. Straumann, P. Truöl and T. Walter

in collaboration with:

the Universities of Heidelberg and Siegen and 31 further institutes from outside Switzerland

(HERA-B collaboration)

Originally we started to contribute to the development of microstrip gas chambers, which work well in a high-rate hadronic environment, with a short term and a long term objective.

The long range goal was linked to the participation of our institute in the CMS collaboration at LHC. The technical design report for this planned detector foresaw microstrip gas chambers for the central and forward/backward barrel tracker. Various refereeing committees from outside and inside of the collaboration defined milestones for the acceptance of the reference solutions, which were proposed by the participating institutions. These milestones were met satisfactorily, in particular after the analysis of several test runs at PSI in 1999 was completed. Despite this fact it was decided by the tracker institution board in December 1999 and finally approved by the CMS collaboration board in January 2000 to build an all silicon tracker. The basis for this decision was that a single technology gives the highest chance for delivering a working tracker on schedule. Since our institute is already contributing to the silicon based pixel detector of CMS (see CMS section of this annual report), it was decided to end our involvement with the construction of the forward/backward barrel tracker.

The short range goal was linked to the inner tracker of the HERA-B experiment at DESY, where the rate requirements are similar to those expected for CMS. Here we joined groups from Heidelberg and Siegen and helped building this microstrip gas chamber based detector part. After U. Straumann accepted an offer for a full professorship at our institute and left Heidelberg for Zürich, the Zürich group within HERA-B is now stronger and we decided to continue our participation for a few years on a modest level, i. e. with typically one graduate student and two postdocs. O. Steinkamp from U. Straumann's group had coordinating functions within the outer tracker group of HERA-B and is one of the eight run coordinators of this experiment.

We concentrate in our report mainly on the Zürich contributions to the inner tracker and on our independent measurements concerning the microstrip gas chambers used in that set up, but give also, as last year, a short account of the status of the experiment.

8.1 Microstrip gas chamber development for the inner tracker

During the last year we finalized the design for the support structure of the four inner tracker stations inside and before the HERA-B magnet. The complete set was built in our workshop and successfully installed in the detector before the end of 1999. At IMT-Greifensee the production of substrates for other stations and replacement of faulty chambers continued. The main order was completed and some additional spare plates were produced. We controlled their quality with our test setup at the company. In 1999 we further tested detectors at PSI with a set of three chambers instrumented with the complete readout electronics (see last year's report [1] for a description of the detectors).

8.1.1 The status of the inner tracker

In 1999 a major part of the inner tracking system was completed and installed at the HERA-B experiment. The system consists in total of 10 stations with 184 detectors. Our group was

responsible for the design and the construction of the support structure for the four stations in and before the magnet as well as for the necessary infrastructure (gas, electronic patch panels, cabling, etc.). The system contains 40 MSGC-GEM-detectors in total, with four detectors arranged around the beam pipe combined to one active layer (see Fig.8.1). The first station in front of the magnet has four layers and each of the three stations inside the magnet two layers. The support structure was optimized to keep the material budget as low as possible, while still allowing for precise mechanical positioning of the detectors.



Figure 8.1: *Left: view of one half of the first station in front of the magnet. The special arrangement of the different layers allows for an overlap of the detectors. Right: view along the beam pipe in $+z$ direction in the magnet. One can recognize the three stations which are instrumented with MSGC's because of the small cutout for the beam pipe.*

Presently all efforts are directed towards commissioning of the chambers in the experiment under running conditions. Every detector has to be trained over about a week, before it can be operated under nominal working conditions. This phase is very important and has to be done in a very safe way. As the system comes now into operation all the necessary infrastructure (gas-system, the slow control system - which is crucial to guarantee a save operation) has to be finalized, adapted and often also improved over the original design. In early March tracks were already successfully reconstructed from the information of different layers of a given station. In the next step all the inner tracking stations need to be combined in the analysis. These track segments have then to be linked to the other detectors, which then also allows an alignment of the system.

Table 8.1 summarizes how many substrates were produced at IMT in total. At the beginning of last year the production of type 1 substrates from the main order (40 plates, see also last year's report [1]) was completed. Spares of all types were manufactured in 1999 and tested like all previous ones with the dedicated setup we installed at the company for that purpose.

Table 8.1: Various substrates [1] produced and tested at IMT for the HERA-B experiment.

Substrate type	Order				
	main	second	third	fourth	Sum
1	37		7		44
2	136	32	6	10	184
3	58	7			65
total	231	39	13	10	293

8.1.2 MSGC tests at PSI

Our previous tests of detectors at PSI were mainly devoted to study their radiation hardness and the ageing properties. In last years tests we measured the homogeneity of our rather large detectors. Large differences in the pulse height between different anodes will influence the efficiency of the detectors and finally determine the quality of the tracking system of HERA-B. They could be introduced by mechanical tolerances (non-flatness of the GEM-foils, variations in the thickness of the frames, etc.) and gain variations in the electronics (variation from channel to channel - from chip to chip). The setup is shown in Fig. 8.2.

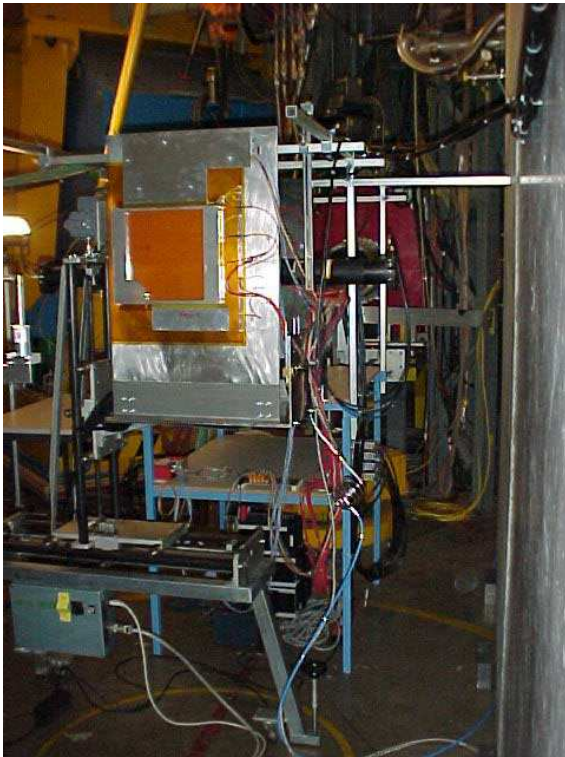


Figure 8.2: *View of the experimental setup used at PSI with the chambers mounted on an x, y -table for beam scans.*

To guarantee, that the radiation does not influence and eventually damage the detector a very low rate pion beam was used during the homogeneity measurement. The beam was horizontally (x -direction) defocused to illuminate the whole detector. To determine the vertical position (y -direction, parallel to the detector strips) of the tracks we used two scintillators. The width of these counters (25 mm) determined the position resolution for our scan in vertical direction. Two standard HERA-B MSGC-GEM-detectors and one further detector where the GEM-foil was stretched in a way to guarantee a more precise flatness

were available for this test. All three detectors were equipped with the complete standard HERA-B readout chain. Figures 8.3 and 8.4 show some typical results from these studies, which will be described in detail in the thesis of T. Walter [2].

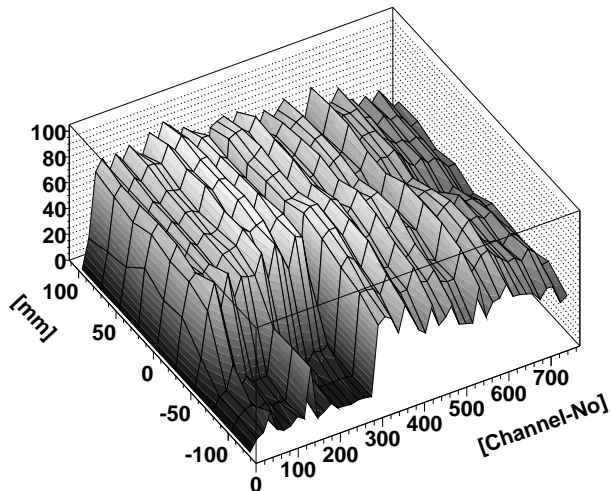


Figure 8.3: *The measured charge distribution of chamber 1 in function of the position. The hole in the lower corner results from the beam pipe cutout.*

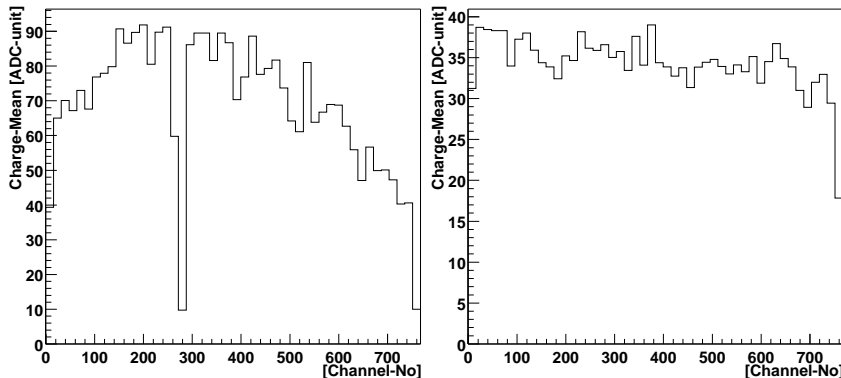


Figure 8.4: *Measured mean charge versus strip number for two different chambers. One channel corresponds to an anode strip. The bins are 20 strips wide.*

8.2 Status of the HERA-B Experiment

8.2.1 Comparison with other B projects

The HERA-B experiment at DESY has been designed to measure CP-violation parameters in the system of neutral B mesons, especially in the so-called golden decay channel $B_d^0 \rightarrow J/\psi K_s^0$. The construction of the experiment is nearing completion, the targets and large parts of the detector are routinely operated. Commissioning of the first-level trigger has commenced and defines the critical path for the startup of physics data taking, which should begin in spring 2000. For a recent summary of the HERA-B experiment we refer also to O. Steinkamp's presentation at the Taipeh conference [3].

The standard model of particle physics predicts sizeable CP violating asymmetries in many different decays modes of B and \bar{B} mesons. Measurements of these asymmetries will put a stringent test on the Standard Model. The golden decay channel is one of the theoretically cleanest and experimentally easiest accessible. Analyses from the LEP experiments Opal and Aleph, and from the CDF collaboration at Fermilab give indications for an asymmetry in this decay channel but the statistical error on these measurements are large.

HERA-B is one of several upstarting experiments that are going to produce large enough samples of B mesons to establish CP violating effects and test Standard Model predictions.

BaBar and Belle are experiments at asymmetric e^+e^- colliders at SLAC and KEK, respectively. Both are entering the data taking phase, while the CDF and D0 experiments at the Fermilab Tevatron are undergoing major detector upgrades that will allow them to study B -meson physics.

In HERA-B, $b\bar{b}$ quark pairs are produced in proton-nucleon interactions on thin wire targets that are introduced into the halo of the HERA proton beam. Different from the e^+e^- collider experiments, all species of B hadrons are produced, giving access to a broader range of observables. Especially the investigation of the oscillation and decays of B_s mesons will give additional constraints on Standard Model parameters. Compared to the general-purpose experiments at Fermilab, the strength of HERA-B lies in its particle identification capabilities. Efficient kaon identification over a wide momentum range is crucial for a large number of measurements.

The main experimental challenge of HERA-B is due to the small $b\bar{b}$ production cross section ratio of $\sigma_{b\bar{b}}/\sigma_{\text{inel}} \approx 10^{-6}$. The experiment must run at a continuous inelastic pN interaction rate of 40 MHz in order to collect in one year of data taking the 1500 reconstructed golden decays that are needed for a competitive measurement of the CP asymmetry in this channel.

Consequently, one of the most challenging systems of HERA-B is the multi-level trigger that must extract the signal channel from the overwhelming inelastic background. In addition, the construction and commissioning of the experiment suffered considerable delays due to various ageing problems discovered in the tracking detectors, that could not withstand the high rates of high-multiplicity hadronic events.

8.2.2 The detector

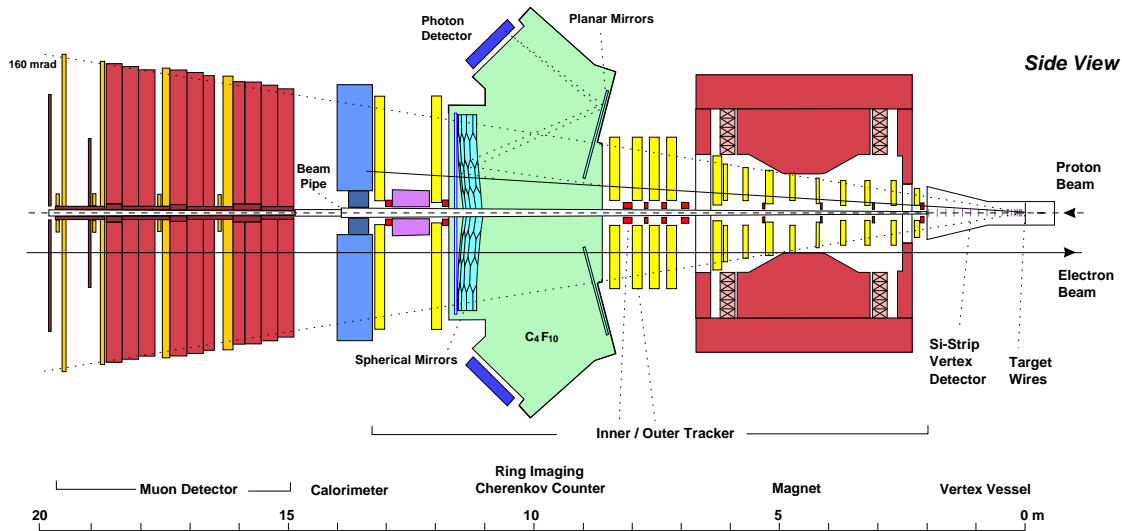


Figure 8.5: *The HERA-B detector*

The experimental apparatus (Fig. 8.5) consists of a large-acceptance forward magnetic spectrometer with a 2.1 Tm normal-conducting dipole magnet, which is complemented by detector elements for vertexing, triggering and particle identification. The main tracking system consists of 13 stations. In each station, the inner tracker (see above) covers the innermost 20 cm around the beam pipe, where particle fluxes are highest. The outer part of the acceptance is covered by up to 4.5 m long honeycomb wire chambers. The first of these detectors that

were operated in HERA-B suffered from various ageing problems. It took a considerable R&D program to demonstrate that no major redesign of the detector concept was necessary and that the observed problems could be overcome by different choices of materials and gas mixture, and improved production techniques. The detector has been completed end of 1999, commissioning is in progress.

Just downstream of the target stations, a seven-station silicon strip vertex detector is located in retractable Roman pots inside the HERA vacuum vessel. For data taking, the detectors approach the proton beam to 1 cm, they are retracted during beam insertion. The system is completely installed and routinely operated. It performs well, primary vertex resolutions approach design values.

A gaseous RICH detector mainly serves to identify kaons for tagging purposes. It employs multi-anode photo tubes to detect Cherenkov light produced in a 2.5 m long C_4F_{10} radiator. The detector is fully installed and commissioned, its performance matches design values. An early analysis, comparing measured RICH ring radii with track momenta, shows a clear $p/K/\pi$ separation.

A sampling electromagnetic calorimeter allows to trigger on high transverse momentum (p_T) electrons and provides offline reconstruction for decays involving photons. It uses a shashlyk design with scintillating fibers in tungsten and lead absorbers. The detector is fully installed. In the absence of tracking information, a preliminary calibration was performed using the $\pi^0 \rightarrow 2\gamma$ invariant mass. Clear $\eta \rightarrow 2\gamma$ and $\omega \rightarrow 3\gamma$ signals are seen.

The muon detector consists of four stations, which are separated by iron/concrete absorbers. The innermost part of each station is covered by gas pixel detectors, the outer part by gas tube chambers. The last two stations are equipped with a pad readout for triggering on high- p_T muons. The detector is fully installed and operational. Observed occupancies and coincidence rates between the trigger layers agree with expectations.

8.2.3 The trigger system

The HERA-B multi-level trigger system is based on the reconstruction of high- p_T tracks, two-particle invariant masses and detached vertices. High- p_T electron, muon and hadron pre-triggers are generated by clusters in the calorimeter, coincidences in two layers of the muon system, or three-fold coincidences from dedicated pad detectors inside the magnet. Any such pre-trigger defines a geometrical region of interest (RoI) which is sent as a message to the first-level trigger. At nominal interaction rates, several such RoIs will be found for each HERA bunch crossing. Almost the full acceptance of the calorimeter is equipped with pre-trigger electronics. The system is in routine operation. Muon pre-trigger electronics are installed on a significant part of the detector and perform according to expectations. Both systems should be completed in March 2000. Installation of the hadron pre-trigger system is expected to begin in March.

The first-level trigger (FLT) must provide a reduction factor of about 200, within a latency of less than $12 \mu s$. Starting from the RoIs defined by the pre-trigger systems, it searches for tracks through four tracking stations downstream of the magnet. Track candidates are passed as messages between custom-made processors, each of which covers part of the acceptance of a station. On reception of a message, the processor searches the corresponding RoI for matching hits and generates an updated message which it sends to the appropriate processors in the next station. A momentum estimate is calculated for tracks that were followed through all stations. The trigger decision is based on single high- p_T tracks and on the invariant mass of track pairs. Most of the FLT hardware has been produced, installation and commissioning are under way. The system is planned to reach full power by April 2000.

The second- and third-level triggers together have to provide a reduction factor of about 1000. The second-level trigger re-processes FLT tracks. It performs a track fit, follows track candidates through the vertex detector and tries to fit vertices. The trigger decision is based on single-track impact parameters or on secondary vertices. The third-level trigger can refine the second-level decision, using full event information. Both trigger levels are integrated with the data-acquisition system on a 240-processor farm of Pentium processors running the Linux operating system, a high-bandwidth switch, and a system of so-called second-level buffers. The hardware is in routine operation, portions of the second-level algorithm have been exercised routinely. Figure 8.6 shows a reconstructed $J/\psi \rightarrow e^+e^-$ signal, where two high- p_T calorimeter clusters with matching tracks in the vertex detector were demanded. A loose vertex cut was made and one of the tracks was required to have an associated bremsstrahlung cluster. No information from the main tracking detectors was used.

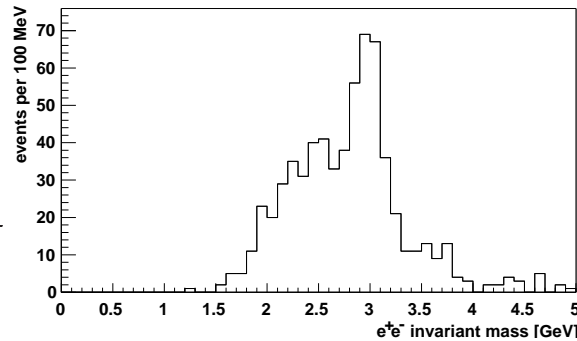


Figure 8.6: $J/\psi \rightarrow e^+e^-$ signal, reconstructed by the second-level trigger

The fourth-level trigger is intended for full online event reconstruction. It runs on a 200-node farm of Pentium processors, which is connected via standard Ethernet technology and operates at a data throughput rate of 50 Hz. The farm is complete and routinely in use for data logging, monitoring purposes and partial reconstruction. The full reconstruction code exists and is being tuned for online running.

After significant delays, the HERA-B detector is nearing completion. Large parts of the apparatus have been operated routinely over the last year and have performed up to expectations. The critical path is now defined by the installation and commissioning of the first-level trigger. HERA running will continue until September 2000, when the accelerator will be shut down for several months to allow for a major luminosity upgrade. If routine operation of the first-level trigger can be established, HERA-B should be able to accumulate before this shutdown a solid sample of B decays and possibly contribute to the ongoing effort to establish CP violation in decays of neutral B mesons. After the shutdown, especially the high- p_T hadron trigger will open a wide field of studies in CP violation and heavy-flavour physics.

References

- [1] Physik-Institut, Universität Zürich, Annual Report 1998/9, available at <http://www.physik.unizh.ch/jb/1999>.
- [2] *Microstrip gas chambers (MSGC) for the HERA-B experiment*, Thesis T. Walter, in preparation.
- [3] *Status and Results from HERA-B*, O. Steinkamp, 3rd Int. Conf. on B Physics and CP Violation, Taipei (Taiwan), December 1999, to be published by World Scientific (Singapore).

9 High-precision CP-violation Physics at LHCb

R. Bernet, P. Sievers, O. Steinkamp, U. Straumann, D. Wyler, M. Ziegler

in collaboration with:

University of Lausanne, Max Planck Institute, Heidelberg, University of Santiago de Compostela, Spain, and 47 other institutes

LHCb Collaboration

LHCb is a second generation experiment on b quark physics which will run from the beginning of the LHC (Large Hadron Collider) operation at CERN (around the year 2005). The goal of the experiment is to make systematic measurements of CP violation and rare decays in the B-meson system with unprecedented precisions. By measuring CP violation in many different decay modes of B_d , B_s and B_c mesons and comparing the results with the predictions from the Standard Model, the experiment will open a new and very sensitive window for searching for new physics.

The LHCb group at the University of Zurich was founded when U. Straumann became the successor of W. Kündig at the Physics Institute in September 1999. The group joined LHCb as a full collaboration member in December 1999. LHCb consists now of about 50 institutions from 14 countries.

The Zurich group concentrates on development, construction, operation and data analysis of the inner tracking part of this experiment. The present research and development phase includes a close collaboration with the particle physics group of the university of Lausanne. Furthermore the Max Planck Institute in Heidelberg, Germany, and the University of Santiago de Compostela, Spain, are members of the inner tracking group of LHCb. The R&D will be continued until about end of 2001, when we are expected to define the final system and document it in a technical design report. After that we will contribute to the construction of these detectors, making use of the excellent technical infrastructure provided by our institute.

We also want to contribute to the preparation for the running and analysis strategy, with special emphasis on trigger algorithm development and support. Here we can fortunately rely on the large experience of our colleagues in the “Institut für theoretische Physik” of our faculty in the field of B physics (group of Prof. D. Wyler).

Since this is a new activity this section is somewhat detailed and contains also an extended discussion of the physics motivation. Part of the detector R&D described below, has started in Heidelberg, and was later on continued at the university of Zurich.

9.1 CP – Violation and Physics of B Mesons

9.1.1 CP violation within the standard model and beyond

The past 10 years have seen a tremendous improvement in the quantitative understanding of the standard model (SM) of particle physics, describing three different fundamental interactions and three generations of fundamental particles. The relevant constants of nature (mass of electroweak interaction bosons, Weinberg mixing angle, coupling constants etc.) have been determined consistently. There are, however, two important open issues within the SM: the Higgs particle, yet unobserved, and the CP violation which so far is only understood qualitatively in the SM.

While a discovery of the Higgs during the last year of LEP operation is still possible, the experiments ATLAS and CMS at the LHC project will definitely shed light on the question of its existence and hopefully be able to study its properties in detail.

A very fundamental feature of the standard model is its prediction of CP violation in the weak interaction of quarks. Any violation of the discrete space – time symmetries is by itself certainly very fundamental for our understanding of nature. Moreover, CP violation is one of the three crucial ingredients necessary to explain the present matter – antimatter asymmetry in the universe (Sakharov 1967). The SM can naturally generate some CP violation, but new sources of CP violation in theories beyond the SM are needed [1] to predict the magnitude of this asymmetry.

The SM describes CP violation with a single complex phase in the quark mixing matrix V_{CKM} . In the following we will refer to the Wolfenstein parametrisation, in which η represents the imaginary CP violating component:

$$V_{\text{CKM}} = \begin{pmatrix} V_{ud} & V_{us} & V_{ub} \\ V_{cd} & V_{cs} & V_{cb} \\ V_{td} & V_{ts} & V_{tb} \end{pmatrix} = \begin{pmatrix} 1 - \lambda^2/2 & \lambda & A\lambda^3(\rho - i\eta) \\ -\lambda & 1 - \lambda^2/2 & A\lambda^2 \\ A\lambda^3(1 - \rho - i\eta) & -A\lambda^2 & 1 \end{pmatrix} + \delta V_{\text{CKM}} \quad (9.1)$$

The first part is accurate to third order in λ . Once the CP violation in the B system will be measured to an accuracy of order 2% or better, terms up to order λ^5 will have to be taken into account. This is also needed for the determination of CP violation in the K system:

$$\delta V_{\text{CKM}} = \begin{pmatrix} 0 & 0 & 0 \\ -iA^2\lambda^5\eta & 0 & 0 \\ A(\rho + i\eta)\lambda^5/2 & (1/2 - \rho)A\lambda^4 - iA\lambda^4\eta & 0 \end{pmatrix} \quad (9.2)$$

Often the phases of the complex numbers are also quoted: $\beta := -\arg V_{td}$, $\gamma := -\arg V_{ub}$, $\delta\gamma := \arg V_{ts} \approx 2\%$.

At present the best values of the four independent parameters are [2]:

$$\begin{aligned} \lambda &= 0.2196 \pm 0.0023 \\ A &= 0.82 \pm 0.04 \\ \rho &= 0.20 \pm 0.06 \\ \eta &= 0.340 \pm 0.035 \end{aligned} \quad (9.3)$$

These values were obtained by a global standard model fit, including the CP violation parameter ϵ_K determined in $K^0 - \overline{K}^0$ mixing, $|V_{ub}|$ from $b \rightarrow ul\nu$ branching ratios and the $|V_{td}|$ obtained from the mass difference Δm_d measured in $B_d^0 - \overline{B}_d^0$ oscillation [3].

9.1.2 Present experimental activities

Recently three new experimental results were announced, which indicate a non zero value of the parameter η , and in fact the standard model seems to describe all presently known CP violation effects more or less in a consistent way:

First of all experiments at FNAL (KTeV [4]) and at CERN (NA48 [5]) presented their observation of direct CP violation in the channel $K^0 \rightarrow \pi\pi$. The combined result of the two experiments on the quantity ϵ'/ϵ ($\approx 24 \times 10^{-4}$) lies outside the range predicted by the standard model. Since these calculations have large uncertainties, this discrepancy may not be so significant. However, it stimulated a lot of discussions and more detailed theoretical investigations.

The second important result is the CP violating asymmetry in the channel $B_d \rightarrow J/\psi K_S^0$ reported first by the CDF experiment at the TEVATRON [6]. There exist also analyses from the OPAL [7] and ALEPH [8] collaborations at LEP, albeit with larger errors.

Although the observed value of $\sin 2\beta \approx 0.8 \pm 0.4$ from CDF represents only a two standard deviation from zero, it does indicate the SM expectation of a sizable CP violation in the $B_d^0 - \overline{B}_d^0$ mixing could be correct. The SM prediction using the values from Eq.9.3 yields $0.65 < \sin 2\beta < 0.77$ [3], consistent with the experimental result.

It is interesting to note, that information about V_{td} can also be obtained from $K \rightarrow \pi\nu\nu$, in a theoretically very clean way. The experiment E787 at Brookhaven has measured the branching ratio of the decay $K^+ \rightarrow \pi^+\nu\bar{\nu}$ to be $(1.5^{+3.4}_{-1.2}) \times 10^{-10}$ [9], one of the lowest branching ratios ever determined in particle physics. It is sensitive to $|V_{td}|$ and is in fact predicted to be of order 10^{-10} [2]. Also at Brookhaven National Laboratory the proposed experiment BNL E926 will search for $K_L \rightarrow \pi^0\nu\bar{\nu}$. The branching ratio is proportional to η^2 and is calculated to be about 2.8×10^{-11} [10].

Presently, we see the two asymmetric e^+e^- collider B factories at SLAC (experiment BaBar) and KEK (experiment Belle) coming into operation. Together with run II of the TEVATRON with the upgraded experiments D0 and CDF and the experiment HERA-B at DESY they will soon provide a reasonably accurate measurement of the angle β , and thus contribute to a good initial understanding of CP violation in the B_d sector.

9.1.3 Second generation B physics program

The planned LHCb experiment will become operational in 2005 as soon as the LHC collider becomes available. At that moment, the results from the B factories, TEVATRON and HERA-B will have already established CP violation in the B -meson systems in a few decay channels. These measurements will concentrate on $\sin(2\beta)$ which, however, is not sufficient to test the validity of the standard model.

In addition, HERA-B, CDF and D0 will probe $B_s - \overline{B}_s$ oscillations. Their sensitivities cover most of the parameter space allowed by the SM. A $B_s - \overline{B}_s$ oscillation frequency much larger than expected from the SM would be a clear indication of new physics.

A second generation B physics experiment must ask more fundamental questions: It should search for a sign of new physics by measuring ρ and η from many different CP violating B meson decay modes with a high precision. In absence of new physics, all the measurements must give consistent values of ρ and η , while inconsistent values will require new physics. In any case the observations will drastically reduce the parameter space of new physics models.

New physics can also be searched for by studying the decay modes that are rare in the SM. Many rare B meson decay modes are generated by penguin diagrams. Since they are first order in the weak interaction, new physics may not alter the branching fractions significantly. However, a sizable CP violation effect can be produced through the interference between the SM and new physics interactions [11]. There is a growing theoretical interest to identify promising decay modes to probe new physics. Particularly, comparing different determinations of the angle γ is potentially very sensitive to new physics [12]. Recently the use of B_c mesons to measure γ has been rediscovered [13].

Unfortunately, such studies of very low branching fractions or small CP asymmetries require very large numbers of B mesons. Only hadronic interactions at the highest available energies can produce a sufficient number of b quarks. The production cross section of B mesons at the new collider LHC at CERN will exceed those of the B factories and HERA-B by several orders of magnitude and those of the TEVATRON by more than one order of magnitude. At the TEVATRON a B experiment is being considered (BTeV) to be run in collider mode after the year 2006, simultaneous to the LHCb experiment. This experiment will certainly allow to perform many cross checks of LHCb results.

9.2 The design of a B experiment at LHC

Even though the B production cross section is very large at LHC, selecting interesting and accurately measurable B events out of the minimum bias background (due to light quark production in pp scattering) represents a major challenge. The following considerations lead to an optimized second generation B experiment at LHC:

- b quarks are mainly produced through gluon – gluon fusion and gluon splitting processes. Their angular distribution is strongly peaked in the forward direction and the B mesons have larger average momentum here, reducing inaccuracies in momentum and mass resolutions due to multiple scattering. Therefore a forward spectrometer geometry is chosen.
- Because most of the time the $b\bar{b}$ pairs are leaving into the same hemisphere, only a single spectrometer arm already gives an acceptable efficiency to observe both the b and the \bar{b} decay products in the same event. This allows to identify the initial flavour of a given B^0 decay by looking at the sign of the charged lepton or kaon from the decay of the other b quark (“tagging”).
- The most important selection mechanism for B meson decay events is their finite lifetime. Therefore a vertex detector with very high resolution is mandatory. Vertex information should also be available for trigger decisions at the earliest possible stage. The second level trigger operating at an input rate of 1 MHz allows to reconstruct two or more vertices and to cut on the distance between them.
- Another important event selection method is the reconstruction of the invariant mass and the momentum of the B from its decay products. The magnetic dipole spectrometer is designed in such a way, that the invariant mass resolution receives similar contributions from measurement inaccuracies from the vertex detector and from the spectrometer.
- The rare decays are often hidden behind backgrounds of other very similar B decays, which can only be separated by a good particle identification. A muon system and for electron identification a shashlik type electromagnetic calorimeter (ECAL) is foreseen. To distinguish between pions and kaons a sophisticated ring imaging Cerenkov counter system is being designed, which consists of three different radiators in two detector stations, allowing excellent π/K separation over the whole momentum range.
- Many of the interesting B decay channels contain only hadrons in the final states. Simple lepton triggers do not allow to select such events, therefore a hadronic calorimeter (HCAL) is introduced together with a high p_T trigger system.
- The optimal luminosity, providing a high B production rate and – at the same time – avoiding too many multiple interactions to avoid confusion in the event reconstruction, is presently believed to be $2 \times 10^{32} \text{ cm}^{-2} \text{ s}^{-1}$, about 2 % of the design luminosity of LHC. The luminosity in the LHCb area will be adjustable with a dynamic range of about a factor 100, therefore we will be able to run at our optimal value, independent of the maximum luminosity of LHC, which might be lower during initial operation.

These considerations lead to a detector design for LHCb, which is shown in Fig. 9.7.

The LHCb detector is described extensively in a technical proposal [16], which has been accepted by the CERN scientific committee (LHCC) and was approved by the CERN management in 1998.

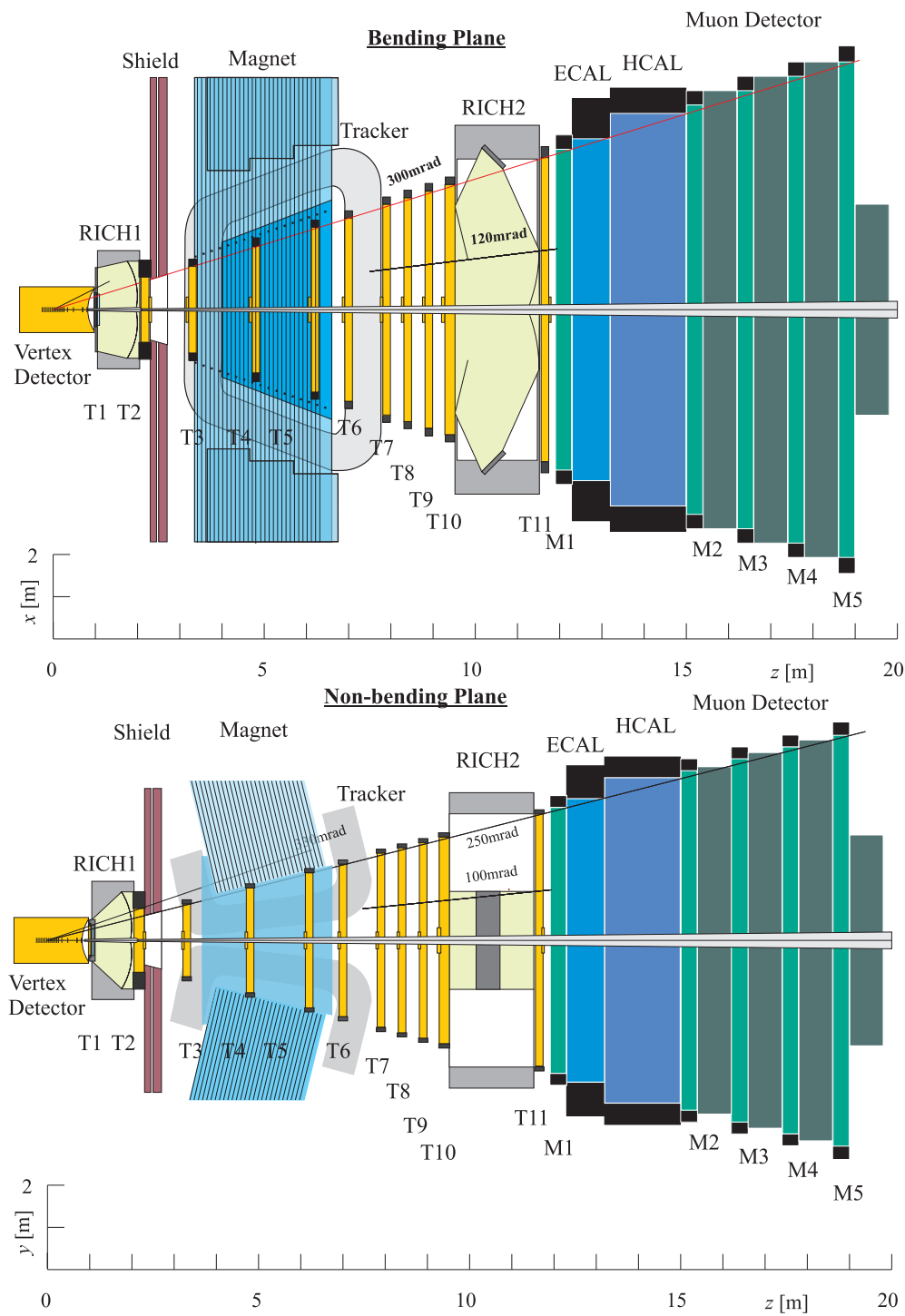


Figure 9.7: Schematic layout of the experiment LHCb in top (bending plane) and side (non-bending plane) view. The pp interaction point is on the left. Each tracking station consists of an inner and an outer part, indicated by T1 ... T11.

Presently detailed design studies are being performed, which should lead to final system definitions in the next two years. They will be described in technical design reports (TDR) separately for each of the various subsystems. The construction period will extend until the year 2004, such that commissioning may coincide with the initial startup of LHC.

9.3 B physics at LHC

The LHCb experiment will run with an optimised luminosity of $2 \cdot 10^{32} \text{ cm}^{-2} \text{ s}^{-1}$ and produce more than 10^{11} B_d and B_s mesons per year. The large improvement of LHCb over the first generation B experiments allows to access many more interesting B decay channels thanks to much larger event samples.

In this context the question arises, whether an extended B – physics program could be done also with the planned universal detector facilities ATLAS and CMS at LHC. Since these detectors are designed to run at full LHC luminosity, they will produce even more B mesons, which one could use for B physics studies.

At a closer look there are, however, four important reasons to build a special experiment dedicated to the second generation B physics program:

1. For time dependent CP asymmetry analysis of B_s decays, but also for efficient event selection, a very good eigentime resolution is needed. The LHCb experiment with its forward geometry has much higher average momenta of the B decay products and therefore the eigentime resolution is less affected by multiple scattering.
2. Many of the interesting channels can only be selected with a very good particle identification, which allows to separate π and K over a wide range of momenta. One example is the decay $B_s^0 \rightarrow D_s^\pm K^\mp$, which suffers from a high background from the channel $B_s^0 \rightarrow D_s^- \pi^+$, which has a much larger branching fraction. The RICH detectors in LHCb provide an elegant solution to this problem, while no such possibility is foreseen in the ATLAS and CMS experiments.
3. A trigger system, especially optimised for B decay channels is needed to make optimal use of the existing B production rate. ATLAS and CMS can neither trigger on secondary vertices nor on high p_t hadrons.
4. Due to the specific optimisations for the large forward spectrometer the reconstructed invariant mass resolution of the B turns out to be typically a factor of two better than in ATLAS and CMS, depending on the decay channel.

Table 9.2 compares the possibilities of the three LHC experiments. Shown are the expected statistical accuracies for the various CP violation parameters. Systematic errors are generally smaller.

It is obvious that, compared to the first generation experiments, much larger samples of many more different decay channels will be available. This will allow to measure not only the angle β very accurately as a test of the standard model description of CP violation, but also the other significant phase angles of the CKM matrix elements γ and $\delta\gamma$.

It is evident, that for simple channels like $B_d \rightarrow J/\psi K_S^0$ all LHC experiments can do equally well. However, for the more sophisticated measurements good π/K separation, well resolved B_s oscillation determination or an efficient hadron trigger are mandatory, which explains the superior performance of LHCb. Only LHCb is able to do the various measurements of γ , which allows high precision cross checking of the standard model predictions and thus provides access to a variety of windows to New Physics. Different supersymmetric

Table 9.2: *Statistical sensitivities^[a] for some quantities in B – decay[14] as expected from the LHC experiments. The event numbers include detector acceptance, trigger and offline efficiencies. Ranges of sensitivity correspond to range of actual values of: $\alpha \equiv \pi - \beta - \gamma$ ($50^\circ \dots 100^\circ$) and Δm_s ($15 \dots 45 \text{ ps}^{-1}$).*

channel	quantity	method ^[b]	Atlas		CMS		LHCb	
			error	events	error	events	error	events
$B_d \rightarrow J/\psi K_S^0$	$\sin(2\beta)$	t-dep	0.017	165 k	0.015	430 k	0.021	88 k
$B_d \rightarrow \pi^+\pi^-$	$\sin(2\alpha)$	t-dep		2.3 k ^[c]		0.9 k ^[c]	0.07	4.9 k
$B_d \rightarrow \rho\pi$	α	t-dep					0.04-0.09	1.3 k
$B_d \rightarrow D^{*\pm}\pi^\mp$ $D^{*\pm}a_1^\mp$	$2\beta + \gamma$	t-dep					0.26	703 k
$B_s \rightarrow D_s K$			$\gamma - \delta\gamma$	t-dep				
$B_d^0 \rightarrow DK^{*0}$	γ	BR					0.07-0.31	300
$B_s \rightarrow J/\psi\phi$	$2\delta\gamma$	t-dep	0.03	300 k	0.14	600 k	0.02	370 k
$B \rightarrow \pi K$	γ	BR					0.03-0.10	90-175 k
$B_s \rightarrow J/\psi K_s$	γ	t-dep				4100 ^[c]		
$B \rightarrow DD$	γ	t-dep					0.02	300 k
$B_s \rightarrow D_s D_s$								
$B_d \rightarrow \pi\pi$	γ	t-dep	0.09-0.13	1.4 k	0.10-0.33	1 k	0.34-0.68	4.6 k
$B_s \rightarrow K^+K^-$								
$B_s \rightarrow D_s\pi$	x_s		46 ^[d]	3.5 k	42 ^[d]	4.5 k	75 ^[d]	86 k
$B \rightarrow K^*\gamma$							0.01	26 k
$B \rightarrow K^*\mu^+\mu^-$				2 k		13 k		22 k

[a] absolute error assuming one year of data taking (except for $B_d \rightarrow \pi\pi$ / $B_s \rightarrow K^+K^-$ where five years are assumed) at design luminosities

[b] *t-dep*: time-dependent asymmetry analysis, *BR*: comparison of branching ratios.

[c] signal/background < 1

[d] largest value observable

models predict a different values for the energy asymmetry of the lepton pairs produced in $b \rightarrow st^+l^-$ decays [15]. LHCb will produce a large sample of $B \rightarrow K^{*0}\mu^+\mu^-$ per year allowing to distinguish between different supersymmetric models.

In summary the LHCb experiment will provide a second generation B physics facility, allowing highest precision determination of the CP violation parameters of the standard model, exploring extensively heavy flavour physics of b and c quarks and looking for new physics through CP violation interference effects and other methods using rare B decays.

9.4 The inner tracking detector of LHCb

The obvious requirement for the LHCb spectrometer is a very high momentum resolution, as explained above. Detailed studies indicate that the crucial quantity is not the spatial resolution but rather multiple scattering in the spectrometer chambers and very high particle fluxes, originating partially in minimum bias events and to a larger extent in photon conversions in the beam pipe and other dead material in the spectrometer. The somewhat contradictory requirements of a low material budget and a high pattern recognition efficiency lead to an optimal number of 11 tracking stations, each being capable of determining an accurate track space point in all three dimensions.

The design considerations of the tracking chambers are dominated by the search for a technology which can withstand the high particle fluxes (up to $10^4 \text{ sec}^{-1} \text{ mm}^{-2}$). The

granularity of the detector should be sufficiently high, resulting in an average occupancy low enough not to spoil pattern recognition.

Since in the HERA-B [17] experiment at DESY the particle rate conditions and the geometrical arrangement in the tracking is very similar to LHCb, it is obvious that any development for LHCb may benefit from the experience with the HERA-B detector, which is being commissioned right now.

Already in early studies for the HERA-B experiment it turned out, that the tracking chamber needed to be divided into two areas: An outer tracking part with relatively low particle density, where in the HERA-B case honeycomb drift chambers turned out to be an adequate implementation. In the inner tracking a finer granularity and therefore larger number of electronic readout channels were necessary to keep the channel occupancy below a few percent. The area of the inner tracking in LHCb measures 60cm x 40cm around the beam pipe (in HERA-B slightly smaller). For installation reasons the chamber needs to be divided up in at least two halves.

Originally HERA-B had chosen MSGCs for their inner tracking chambers (four quadrants with an active size of typically 28cm x 25cm each). In first beam tests with hadronic particles at the Paul Scherrer Institut it turned out, that this technology is inadequate to withstand very high hadronic particle rates, as explained in more detail below. Therefore an additional gas electron multiplier foil (GEM) was added as “preamplifier” allowing to run the MSGC’s at lower gas gain [18].

In LHCb the choice of the technology for the inner tracking is not made yet. Various gas avalanche multiplication techniques have been studied by the inner tracking group. In February 2000 it has, however, been decided to concentrate on one gas chamber technique (triple GEM, see below) and a silicon option.

9.4.1 Preparatory studies for the HERA-B inner tracking

U. Straumann joined the R&D effort of the Heidelberg–Siegen–Zuerich collaboration to develop inner tracking devices for HERA-B and LHCb in 1996 and initiated a series of beam tests with the already existing MSGC prototypes for HERA-B. The π M1 area in the Paul Scherrer Institut was chosen for these studies, since here hadronic particle fluxes can be achieved which are comparable to those expected for LHCb and HERA-B. The beam allows to irradiate the prototype chambers over a significant fraction of their sensitive area. The goal was to measure all relevant performance parameters and to check the operation stability in a realistic environment.

Already in the first beam test in spring 1996 it turned out, that the MSGC were irreversibly damaged due to frequent beam induced HV breakdowns. Further investigations in the laboratory (with α particles) and at the HERA-B beam at DESY showed, that these breakdowns are triggered by very large primary ionization events, which most likely originate from heavily ionizing particles like nuclear fragments originating from nuclear reactions of the beam hadrons with the detector material. These observations initiated a lot of other studies in various research groups and were also recognised at conferences [19].

Since no other affordable technology was at hand, the only way out of this dilemma was to add a gas electron multiplier (GEM) developed at the CERN gas detector development group (GDD) by F. Sauli and collaborators.

With this two amplification stage detector we were able to perform various crucial rate and stability tests mainly at PSI [18]. These included the final readout electronics with the HELIX [20] chip used at HERA, which contains 128 preamplifiers, discriminated trigger outputs, 12 μ sec analog pipeline and readout multiplexing logic. In summer 1998 we were able

to run the full electronic chain the first time in a real beam and full size detector environment.

In October 1998, a package of three consecutive chambers were operated at PSI [21] for the first time. We observed gain differences up to a factor 2 between chambers of identical construction. Also non-uniformities within single chambers were found. Detailed inspection of the chambers showed, that there were sizeable gap variations (up to ± 0.4 mm) between the MSGC wafer and the GEM foil. These cause small changes of the electrical field in and around the GEM holes, which correspond to the measured gain variation of about a factor 2. There are indications, that the GEM foil loses its mechanical tension, after having been exposed to DME (the quencher gas used at that time).

Furthermore it turned out, that after an irradiation time, which corresponded only to a fraction of the expected HERA-B doses per year, significant ageing occurred, resulting in an almost completely dead chamber. Several investigations with X-ray and chemical analysis of the surface of the wafers showed, that the conductive coating, which was put onto the glass substrate for high rate stability reasons had been etched away by the heavy irradiation load.

Running with an Ar/CO₂ mixture solved that problem partially, such that these chambers should survive at least enough time to take physics data with the HERA-B detector.

9.4.2 Extended investigations for LHCb

It soon became clear that the MSGC-GEM combination, as it is used for the HERA-B detector, is not suited for LHCb. Since this experiment is designed for precision physics and should be running for about 10 years, the long term stability of the electrode structure on the MSGC wafer in harsh hadronic beam environment is by far not good enough. The signal size is only just marginally above the thermal noise of the electronics at an operation high voltage, just above which sparking occurs.

The inner tracking group of LHCb chaired by U. Straumann has therefore decided to start an extended R&D program to look for alternative technologies, which would satisfy the requirements of the inner tracking and would operate more reliably over long time periods. We would accept only technologies which avoid all the problems mentioned above, showing narrow signal shapes both in time (extending over at most two LHC bunch crossing, i.e. 50 ns) and in space, such that the channel occupancy stays low.

The options studied in more detail, including tests at the Paul Scherrer Institut, were Micromegas [22], Microwire [23] and triple GEM [24]. We also profit very much from the studies of the CERN GDD group [25] and the efforts made within the CMS collaboration, including those by the University of Zurich.

Apart from these experimental investigations a detailed simulation of all the technologies considered has been developed [26]. Three-dimensional field maps are considered and Monte Carlo methods are used to study the relevant gas parameters.

9.4.3 Triple GEM

Our group concentrated on developing a multistage GEM detector consisting of several GEM foils placed behind each other. As a result the gas gain in a single stage can be kept low. The amplification planes are followed by a simple printed circuit board with readout strips, which see the charge induced by the drifting electron cloud, originating from the last GEM stage.

Using two GEM foils, different groups [25] had already achieved promising results. However, the spark probabilities in hadronic beams seemed to be still rather high. The prototypes studied by other groups were all of small size (typically 10 cm \times 10 cm or less), which makes

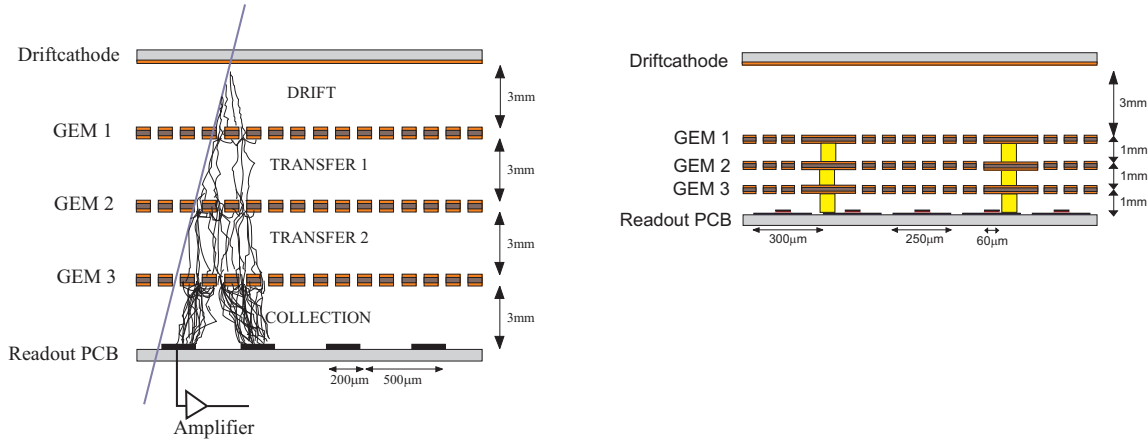


Figure 9.8: Cross section through the triple GEM prototypes. First prototype with 3 mm spacing between the GEM stages (left), second prototype with 1 mm spacing (right).

them much easier to operate due to their lower capacitance resulting in lower thermal noise in the charge sensitive amplifiers.

In order to reduce the total radiation length the Karlsruhe group has tried to use readout boards with two layers of readout strips, allowing to determine two space coordinates with only one detector plane [27]. Unfortunately, this scheme reduces the detector signals by at least a factor two.

All these considerations (large detector increasing the thermal noise, two-dimensional readout lowering the signal, sparking demanding low gas gain) led to the idea to try chambers with three stages of GEM foils.

In 1999 we built two generations of prototypes. Both are full size (about $30 \text{ cm} \times 25 \text{ cm}$) with different sizes of the gap between the GEM foils (see Figures 9.8 and 9.9).

While the first prototype has 3 mm gaps between the GEM foils, the second one was built with 1 mm spacing in order to profit from several advantages of small gaps: It needs less space, needs less total high voltage and most importantly has lower cluster width due to a shorter total drift path. This improves the position resolution and reduces the total occupancy.

In order to keep the gap variations sufficiently low, small spacers (Fig. 9.9) were put between the GEM foils at $\approx 4 \text{ cm}$ intervals. These consist of Polytek H72 Epoxy glue and

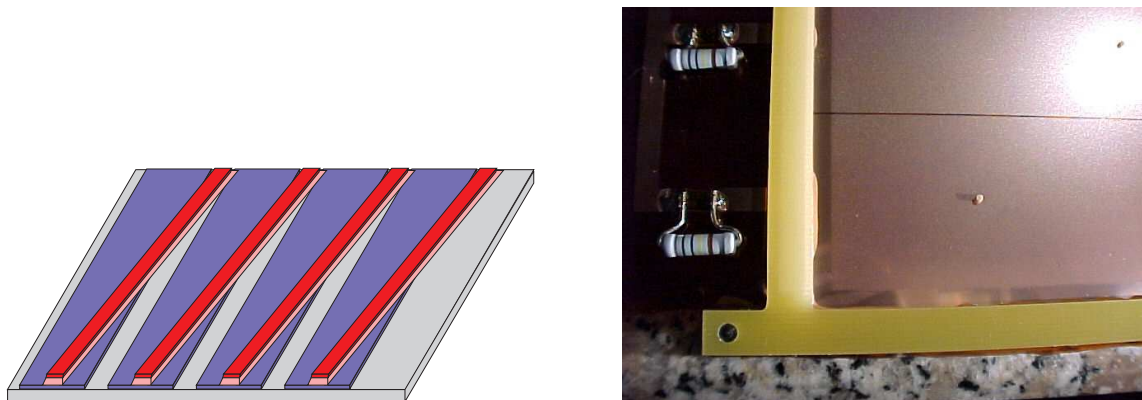


Figure 9.9: Details of the construction of the second prototype. Two-dimensional readout board (left). Frames and spacers (right).

have a diameter of 1.1 mm. In order to avoid any glue to flow into GEM holes, a special mask for GEM foil production makes sure, that at the spacer position there are no GEM holes. The size of this inactive area has a diameter of 2 mm, corresponding to a total inefficient area of less than 0.15 % of the detector.

The chambers are operated with Ar/CO₂ (70:30). Most channels are equipped with HELIX [20] readout, a few channels have a fast amplifier connected (rise time 0.5 ns) to study the signal shape.

The readout strips see in first order only the electron signal from the collection gap and no ion current, therefore this detector produces a very short output signal. Using an iron source we could indeed observe pulse durations consistent with the drift time in the lowest gap (40 ns and 15 ns for the 3 mm and 1 mm gap chamber, respectively) without any indication of an ion tail.

9.4.4 Triple GEM operation in high intensity hadronic beams

After test and calibration of the chambers in the laboratory we operated the detectors in two periods of two weeks each at the π M1 PSI test beam in April and December 1999 respectively.

In the first period we studied the performance of the 3 mm prototype. With a beam containing 50 kHz/mm² π^+ and protons we were able to operate the chamber at a total gain of 20'000 for more than 8 hours without any spark.

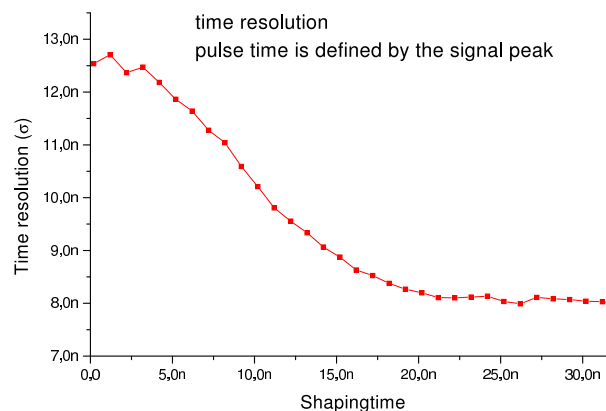


Figure 9.10: *Time resolution, that could be obtained with an ideal zero crossing discriminator, as a function of shaping time.*

With the fast amplifiers signal shapes of the minimum ionizing pions were recorded. They show in fact a complex structure, caused by the overlap of several primary ionization clusters with different size and arrival times. These signals were filtered offline, simulating the influence of a hypothetical electronic shaping circuit. The time resolution was estimated simulating a zero-crossing timing discriminator which determines the time of the pulse maximum. Figure 9.10 shows, that an optimum shaping time exists, which gives good timing resolution and avoids long occupancy times. More details of this pulse shape analysis are given in [24].

The second prototype (1 mm gap) was tested in December 1999 at PSI. It ran very nicely, a plateau curve is shown in Fig. 9.11. The 380 V GEM voltage needed for good efficiency corresponds to a gas multiplication factor of about 20'000. Such a high value is needed, because the two dimensional readout geometry as shown in Fig. 9.9 has a high capacitance of about 90 pF per channel, which causes a very high thermal noise in the connected charge amplifier. We are considering improved geometries to reduce these capacitances by about a factor 3.

At this high gain the 1 mm triple GEM chamber showed a small, but measurable spark probability of order 10^{-9} per incoming π . No damage was observed.

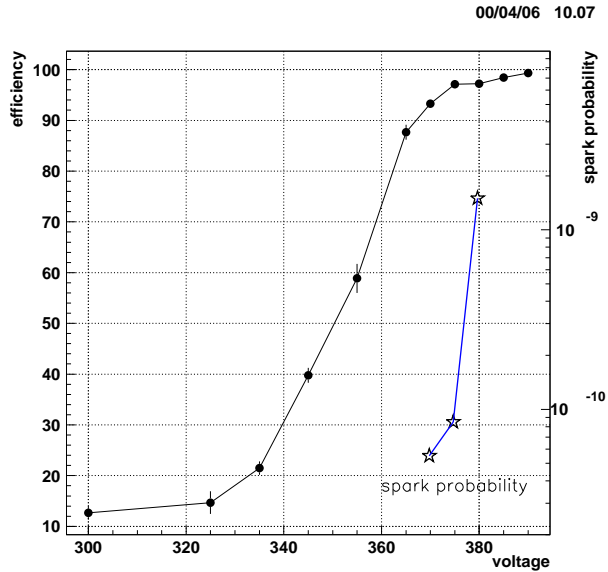


Figure 9.11: *Plateau curve of the 1mm gap prototype measured with 300 MeV/c pions at PSI. The efficiency is given by using a coincidence of two scintillators as a trigger. The spark rate is normalised to the total number of pions impinging onto the detector.*

The cluster size has been measured to be $\sigma = 230\mu\text{m}$, which agrees well with simulations [26].

9.4.5 Conclusions and outlook

The investigations of the other groups within the LHCb collaboration showed, that the sparking rate in both micromegas and microwire is of order 10^{-5} to 10^{-7} per incoming π , which would lead up to 1 kHz of sparking at LHCb running conditions. We therefore abandoned those technologies in a meeting of the inner tracking group in February 2000. LHCb concentrates now on the triple GEM chamber as a gas detector for the inner tracking.

From our experience with gas detectors as well as many other test experiments [25], we learned that chambers with an electrical field configuration which drops significantly slower than $1/r$ away from the anode, are likely to be sensitive to sparking in hadronic environment induced by streamer developments. While a good old fashioned MWPC has a very high HV breakdown limit due to an almost perfect $1/r$ electrical field, chambers with constant electrical fields, like parallel plate chambers or micromegas are very sensitive to sparking. This is also consistent with the observation, that MSGC with surface coating are significantly more sensitive to sparking than those with a high resistive carrier material [28].

There are, however, more effects which are not understood yet, especially the fact, that the spark limits depend very strongly on the chosen noble gas and the quencher gas fraction used.

We therefore started in parallel to look into a silicon microstrip detector solution, which is the only known alternative to the micro pattern gas detectors. They allow to increase the granularity to tackle large occupancies, and they avoid high occupancies due to large angle background tracks originating from the beam pipe, since they have a 10 times shorter active detector length. The total radiation length of the two technologies is comparable (about 0.3% per active layer). Also signal shape and time occupancy look similar in the two technologies, as well as the infrastructure needed (Triple GEM needs gas, silicon needs cooling). Triple GEM detectors are in principle more radiation hard than silicon microstrip detectors.

A final decision for silicon or triple GEM technology will be made before writing the technical design report (about end of 2001).

References

- [1] P. Huet and E. Sather, Phys. Rev. **D51**, 379 (1995).
M.B. Gavela et al., Nucl. Phys. **430B**, 382 (1994).
- [2] *B Physics, the Unitarity Triangle and the Universe*,
A. Falk, J. Hopkins, talk given at Lepton - Photon '99, Stanford University, August 1999.
- [3] *Constraints on the parameters of the CKM Matrix by end of 1998*,
F. Parodi, P. Roudeau and A. Stocchi, LAL preprint 99-03, CERN-SCAN-9905021, March 1999.
- [4] ϵ'/ϵ result from *KTeV*,
E. Blucher, talk given at Lepton - Photon '99, Stanford University, August 1999.
- [5] ϵ'/ϵ result from *NA 48*,
G. Barr, talk given at Lepton - Photon '99, Stanford University, August 1999.
- [6] F. Abe et al., Phys. Rev. Lett. **81**, 5513 (1998),
for an update see also Preprint CDF/PUB/BOTTOM/CDF/4855.
- [7] K. Ackerstaff et al., Eur. Phys. J. **C5**, 379 (1998).
- [8] R. Forty et al., Preprint ALEPH 99-099.
- [9] S. Adler et al., Phys. Rev. Lett. **84** (2000) 3768.
- [10] G. Buchalla, Nucl. Phys. B (Proceedings Supplements) **59**, 130 (1997).
- [11] See for example: L. Wolfenstein and Y.L. Wu, Phys. Rev. Lett. **73** (1994) 2809.
- [12] see for instance: *Extracting γ from $B_{s(d)} \rightarrow J/\psi K_S$ and $B_{d(s)} \rightarrow D_{d(s)}^+ D_{d(s)}^-$* ,
R. Fleischer, CERN-TH-99-78 (hep-ph/9903455) 1999.
- [13] R. Fleischer and D. Wyler, hep-ph/0004010
- [14] *B decays at the LHC*,
P. Ball et al., CERN-TH/2000-101, hep-ph/0003238
- [15] P. Cho, M. Misiak and D. Wyler, Phys. Rev. **D54** (1996) 3329.
- [16] LHCb technical proposal, CERN LHCC 98-4, 20 February 1998.
- [17] HERA-B technical design report, DESY-PRC 95/01, January 1995.
Status and Results From HERA-B,
O. Steinkamp, IIIrd Int. Conf. on B Physics and CP Violation, Taipei City/Taiwan, December 3-7, 1999, (to be published in World Scientific).
- [18] *Operation of a large GEM-MSGC detector in a high intensity hadronic test beam using fully pipelined readout electronics*,
U. Straumann et al., LHCb public note 98-060, 6.10.1998.
- [19] *Microstrip gas chambers: recent developments, radiation damage and long-term behavior*,
B. Schmidt, Nucl. Instrum. Methods Phys. Res., **A419** (1998) 2-3 230-8.
- [20] *The HELIX readout chip manual*, M. Feuerstack-Raible et al.,
<http://wwwasic.ihep.uni-heidelberg.de/~feuersta/projects/Helix/helix.ps.gz>
- [21] Physik-Institut, Universität Zürich, Annual Report 1998/99, chapter 8, available at
<http://www.physik.unizh.ch/jb/1999/kap8.ps>
- [22] *PSI run report of the micromegas detector*,
J.P. Perroud and F. Ronga, LHCb public note 99-020, 14.6.1999.

-
- [23] *Performance of a micro wire detector at a PSI test-beam*,
B. Adeva et al., LHCb public note 99-021, 17.6.1999.
- [24] *A triple GEM detector for LHCb*
M. Ziegler, U. Straumann et al., LHCb public note 99-024, 30.6.1999.
- [25] *High rate behavior and discharge limits in micro-pattern detectors*,
A. Bressan et al., Nucl. Instrum. Methods Phys. Res., **A424** (1999) 321 2/3.
CERN/ EP/ 98-139.
- [26] *Studies on detector prototypes for the inner tracking system of LHCb*,
P. Cwetanski, Diploma thesis, Universität Heidelberg, March 2000.
- [27] *Entwicklung eines hochauflösenden Spurdetektors mit zweidimensionaler Ortsbestimmung*,
Dirk Moehrmann, Diplomarbeit Universität Karlsruhe, 1999.
- [28] *Discharges in MSGC*,
C. Richter et al., submitted to NIM.

10 Particle Physics at LHC/CMS

C. Amsler, R. Kaufmann, H. Pruyss, C. Regenfus, P. Riedler and S. Steiner

in collaboration with:

ETH-Zürich, Paul Scherrer Institut (PSI), Universität Basel and 143 institutes from 30 other countries

CMS Collaboration

The detection of heavy flavors at LHC demands an excellent reconstruction capability for secondary vertices in the high rate environment close to the primary interaction point. The innermost tracking will be provided by a three layer cylindrical pixel barrel detector. We are responsible for the design, test and purchase of the pixel sensors, for the mechanical support structure and for the cooling system.

10.1 Lorentz-angle in irradiated silicon

In 1999 we proceeded with the analysis of the pixel test runs performed at the CERN SPS with 225 GeV/c pions (see last year's annual report and ref. [1]). The depletion thickness of two silicon pixel detectors (8×32 pixels of size $125 \times 125 \mu\text{m}^2$) was measured using the grazing angle method, in which incident particles impinge at small angles α (of typically 7°) with respect to the sensor surface (fig.10.1). This angle was measured accurately for each incident particle by our high precision silicon telescope [1]. The depletion thickness was determined from the "street length" i.e. the number of hit pixels along the beam direction. One of the detectors had been irradiated at PSI with 6×10^{14} pions per cm^2 and annealed for more than one year in a cooled environment of 2°C . For the non-irradiated detector the full depletion thickness of $280 \mu\text{m}$ could be reached, while for the irradiated device we achieved a reduced depletion thickness of $160 \mu\text{m}$.

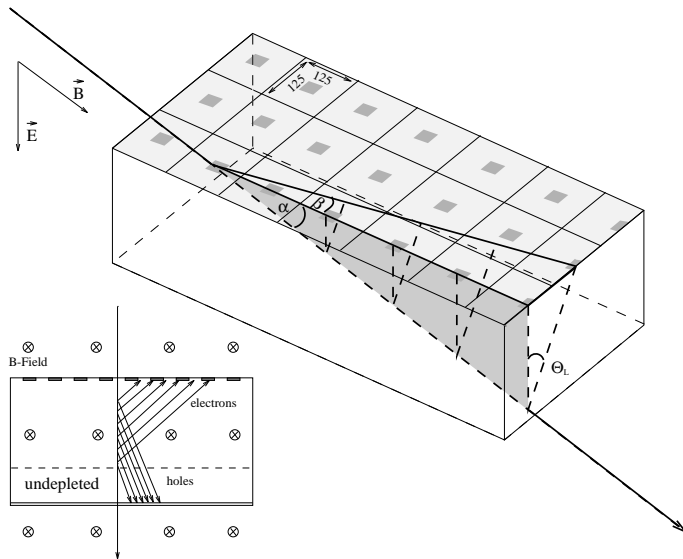


Figure 10.1: *Three dimensional sketch of the pixel detector traversed by a charged particle under the grazing angle α . The Lorentz angle is denoted by Θ_L . The front view of the detector on the left shows the drift directions of electrons and holes.*

The apparatus was immersed in a magnetic field parallel to the beam axis, provided by two Helmholtz coils. Due to deflection in the magnetic field the charge carriers did not move along the electric field lines but drifted at an angle Θ_L (the Lorentz angle) towards the adjacent pixel row (fig. 10.1). The energy deposit was therefore shared among adjacent pixels. By comparing the charge deposits we were able to determine the Lorentz angle: $\Theta_L = (18.2$

$\pm 1.2^\circ$) at 3 Tesla for the non-irradiated detector. The charge sharing between pixels will lead to a position resolution at CMS of typically $15\mu\text{m}$ (r.m.s), well below the individual pixel dimensions.

For the irradiated detector, however, the situation turns out to be more complex. Thanks to the tracking provided by our telescope we could observe a peculiar behaviour as a function of depth. The Lorentz angle appears to vary with the depth of the migrating electron cloud. Figure 10.2(left) shows how the energy deposit is shared between two adjacent pixel rows for the non-irradiated detector. As expected, charge sharing is nearly linear as a function of depth. It increases with depth due to the longer drift distance to the sensors. This is not the case for the irradiated device (right) for which charge sharing increases more rapidly with depth. This different behaviour must be attributed to the changes that occurred after irradiation (type inversion, increase in effective doping concentration and charge trapping from irradiation defects). The effect is not fully understood yet. It leads to a smaller Lorentz angle of about 6° at 3 Tesla just below the sensors and to a larger angle of about 27° at larger depths [2].

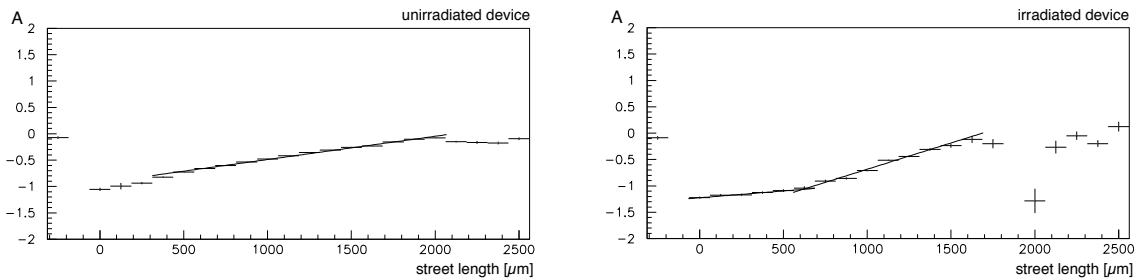


Figure 10.2: *Asymmetry $A = (Q_n - Q_i)/(Q_n + Q_i)$ between charges collected by adjacent pixels as a function of pixel street length (hence depth) for the non-irradiated (left) and the irradiated detector (right). Q_i refers to the charge collected by pixels just above the particle track and Q_n to the charge collected by the next adjacent pixel row (left or right, depending on the sign of the magnetic field).*

10.2 Sensor developments

The barrel detector is made of three cylindrical layers, 53 cm long with radii of 4, 7 and 11 cm, the first layer being used only during initial low luminosity runs [3]. Each layer is made of two half-cylinders to allow insertion into the CMS detector. A pixel unit cell contains 53×52 pixels. The dimensions of the (square) pixels have been increased from $125\mu\text{m}$ in the original proposal to $150\mu\text{m}$. Two rows of 8 cells build a module and a row of 8 modules builds a facet of length 53 cm and width 1.75 cm. The total number of pixels to be read out is about 3×10^7 .

The bulk material is n -type (thickness of $300\mu\text{m}$) and the pixel implants are n^+ (larger concentration of donors). A p^+ layer is deposited on the opposite side of the wafer to form the junction. In the original (non-irradiated) detector the depletion layer grows with applied bias voltage in the the n -bulk from the p^+ side. During irradiation type inversion occurs and the depletion layer then grows from the pixels side.

The n^+ sensors are manufactured by ion implantation. A thin layer of SiO_2 is then generated in a O_2 vapour environment at 1000°C , after which a small square hole is etched at the center of the pixel to provide the electrical contact. The sensor is covered with a thin layer of aluminium which also flows into the contact hole, see fig. 10.4 (right) below. After passivation a small hole is etched in the SiO_2 layer in the corner of the sensors and the

aluminium is covered with a titanium-tungsten alloy and gold (underbump metallization). This provides the contact with the readout chip through the indium bump. Figure 10.3 (right) shows an electronic microscope photograph of a readout chip designed at PSI, and the indium bumps.

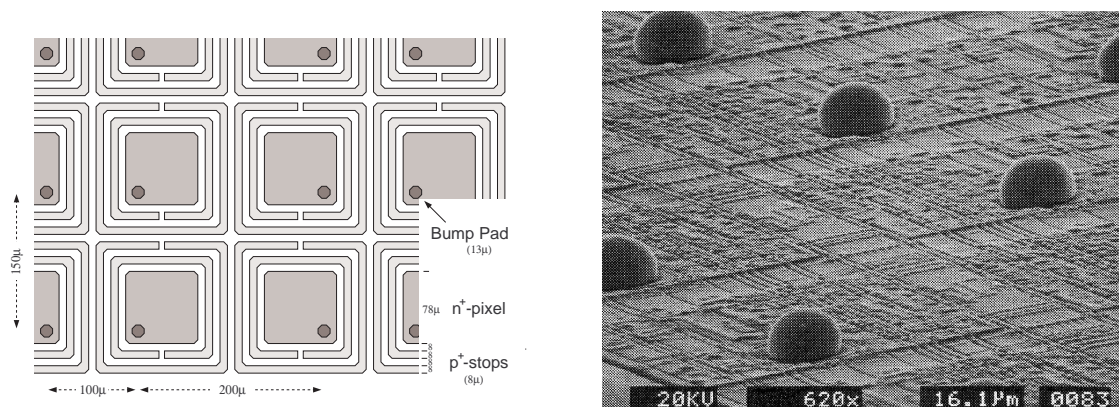


Figure 10.3: *sensors with threefold guard ring structure. Right: Radiation hard readout chip showing the indium bumps.*

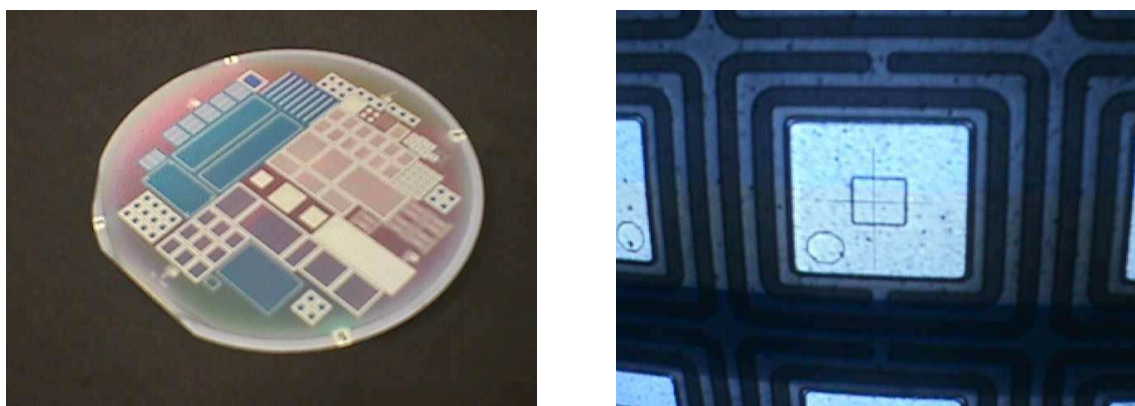


Figure 10.4: *Left: One of the 4" wafers delivered by CSEM. Right: Microscope photograph of one of the sensors showing the p^+ -stop rings (dark) and the metallic layer (bright area) showing the small square and round contact holes for the electrical connections to the n^+ implant and the indium bump, respectively. The faint crosshairs stem from the digital camera.*

One expects that a small fraction of the pixels might have poor electrical connections with the readout chip through the indium bumps. The accumulation of charge would then lead to local breakdown. We have designed a maze around every sensor to increase the resistance between pixels (fig. 10.3, left). The atolls (p^+ -stop rings) provide a high resistive path between the pixels and prevent the charging up, whenever the bump bond fails. A pixel is thus a square of $78 \mu\text{m}^2$ surrounded by two p^+ -stop rings, $8 \mu\text{m}$ wide with a separation pitch of $8 \mu\text{m}$.

We have designed the masks and ordered prototypes for the pixels sensors. A batch of 24 wafers (4"), some with high (5-6 $\text{k}\Omega \text{ cm}$) and some with low (1-2 $\text{k}\Omega \text{ cm}$) resistivity were ordered from CSEM in Neuchâtel. Since oxygen impurities have been found to improve the radiation hardness of silicon detectors [4], we have ordered an additional batch of oxygenated wafers which have not been delivered yet. Figure 10.4 shows a photograph of one of the

delivered wafers which contains various pixel and atoll geometries. (Our sensor submission also included silicon pads to be used on PSI/SLS projects.) We have performed mechanical stress tests and also electrical tests of the (so far not irradiated) prototypes by measuring the capacitances C on a probe station. The depletion thickness d grows as the square root of the bias voltage while C increases with $1/d$. Therefore $1/C^2$ should increase linearly with bias voltage, as observed, until full depletion is achieved (Fig. 10.5, left). Figure 10.5 (right) shows the current between a pixel at 0.2 V and its grounded neighbours as a function of bias voltage. After full depletion, reached at a bias voltage of 160 V (kink), a resistance of a few $M\Omega$ is achieved. The residual current is due to e^- accumulation under the oxide layer.

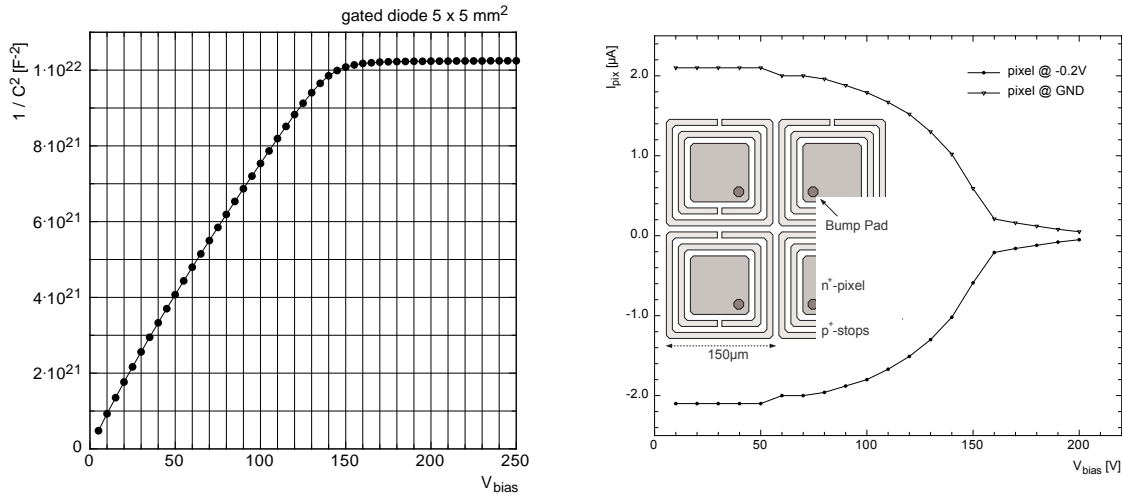


Figure 10.5: *Left: Measurement on a probe station of the capacitance as a function of bias voltage. The maximum depletion thickness is achieved in the plateau region. Right: Interpixel current as a function of bias voltage. Full depletion is reached at 160 V (kink).*

However, the resistivity will change after radiation damage. This will be investigated next summer. The delivered sensors will be cut and bump-bonded to the DMILL PSI30 readout chips developed at PSI. After irradiation at the CERN-PS we will perform tests of the atoll structure (breakdown performance, charge collection efficiency between pixels) using our tracking telescope. The R&D phase of the project will continue until 2002 and will be followed by the mass production phase. LHC will be commissioned in 2005 at which time we should have delivered the two innermost pixel layers for the initial low luminosity runs.

References

- [1] M. Glättli, Diplomarbeit, Universität Zürich (1998).
- [2] R. Kaufmann and B. Henrich, Proc. of the ENDEASD Workshop, Santorin (1999) and Nucl. Instr. and Methods in Phys. Research A (in print).
- [3] Technical Design Report of the CMS Tracker, CERN/LHCC 98-6 (1998)
- [4] M. Moll, E. Fretwurst, G. Lindström (ROSE Collaboration), Nucl. Instr. Meth. in Phys. Res. A 439 (2000) 282.

11 Superconductivity and Magnetism

J. Hofer, H. Keller, R.I. Khasanov (since September 1999), M. Mali, P. Morf, J. Roos, A. Schilling, A. Shengelaya, M. Willemin (till September 1999), G.M. Zhao, S. Zech-Döttinger (since May 1999), C. Boekema (visiting scientist), V.A. Ivanshin (visiting scientist), B.I. Kochelaev (visiting scientist), T. Schneider (Titularprofessor), and K.A. Müller (Honorarprofessor)

in collaboration with:

ETH Zürich (K. Conder, J. Karpinski), PSI Villigen (E. Morenzoni), IBM Rüslikon (C. Rossel), U. of Birmingham (E.M. Forgan, S.H. Lloyd, T.M. Riseman, T.J. Jackson, P.G. Kealey), U. of St. Andrews (S.L. Lee, F.Y. Ogrin, C. Ager), Institut Laue-Langevin, Grenoble (R. Cubitt), U. of Oxford (S.J. Blundell, B.W Lovett), RIKEN-RAL (F.L. Pratt), U. of Warwick (D.McK. Paul), U. of Tokyo (K. Kishio, T. Sasagawa), U. of Tsukuba, Tsukuba, Ibaraki, Japan (K. Kadowaki), U. of Maryland (R.L. Greene, T. Venkatesan, D.J. Kang, W. Prellier, M. Rajeswari), U. of Rome (A. Bianconi, N.L. Saini, A. Lanzara), U. of Berkeley (R.A. Fisher, N.E. Phillips), Los Alamos National Laboratory (M. Hundley, A. Lacerda), Argonne National Laboratory (U. Welp, W.K. Kwok, R.J. Olsson, G.W. Crabtree), Kazan State U., Russia (B.I. Kochelaev), U. of Belgrade, Yugoslavia (I.M. Savić), Institute of Low Temperature and Structure Research, Wrocław, Poland (P.W. Klamut), Institute of Physics, Warsaw, Poland (A. Wisniewski), Northern Illinois U., DeKalb, USA (B. Dabrowski), Neurochirurgische Klinik, Städtisches Krankenhaus, Ingolstadt, Germany (A. Horowski).

11.1 Introduction

In the past year we have continued and extended our investigations of the magnetic and electronic properties of high-temperature superconductors (HTS) and related magnetic systems. In particular, we have performed extensive oxygen isotope ($^{16}\text{O}/^{18}\text{O}$) effect studies on various physical quantities (critical temperature, charge ordering temperature, spin glass temperature, in-plane penetration depth, EPR linewidth) in these systems in order to explore the role of lattice effects in these systems. Furthermore, we have continued our detailed study of the complex vortex state in HTS that we have started several years ago. Last year we have made an important extension of our solid state physics laboratory by incorporating a part of Prof. Brinkmann's former NMR/NQR laboratory, which is now under the supervision of the NMR/NQR specialists Dr. Roos and Dr. Mali. A major contribution to the strength of our work is the application of complementary experimental techniques such as muon spin rotation (μSR), small angle neutron scattering (SANS), NMR/NQR, electron paramagnetic resonance (EPR), together with bulk SQUID and torque magnetometry measurements, resistivity, and thermal measurements. This allows us to investigate the same physical problems on the same samples by means of different methods. The scientific goal of our research is not only to gain new insight on the basic understanding of high-temperature superconductivity, but also to contribute to a better understanding of vortex matter in these materials, which is of fundamental importance for technical applications.

11.2 Studies of oxygen isotope effects

11.2.1 Oxygen isotope effects in manganites

The magnetic properties of the manganite perovskites $\text{Re}_{1-x}\text{A}_x\text{MnO}_3$ (Re = a rare-earth element, and A = a divalent element) have attracted renewed interest because of the observation of colossal magnetoresistance (CMR) in thin films of these materials [1, 2]. Despite

of tremendous experimental efforts [3], the basic physics and the microscopic mechanism for CMR in these materials remain controversial [4, 5, 6].

In order to discriminate among those different models, we study the oxygen isotope effect on the transport properties of high-quality epitaxial thin films of $\text{La}_{0.75}\text{Ca}_{0.25}\text{MnO}_3$ and $\text{Nd}_{0.7}\text{Sr}_{0.3}\text{MnO}_3$. The intrinsic resistivity of these compounds shows a strong dependence on the oxygen isotope mass in both the paramagnetic and the ferromagnetic state (see Fig. 11.1).

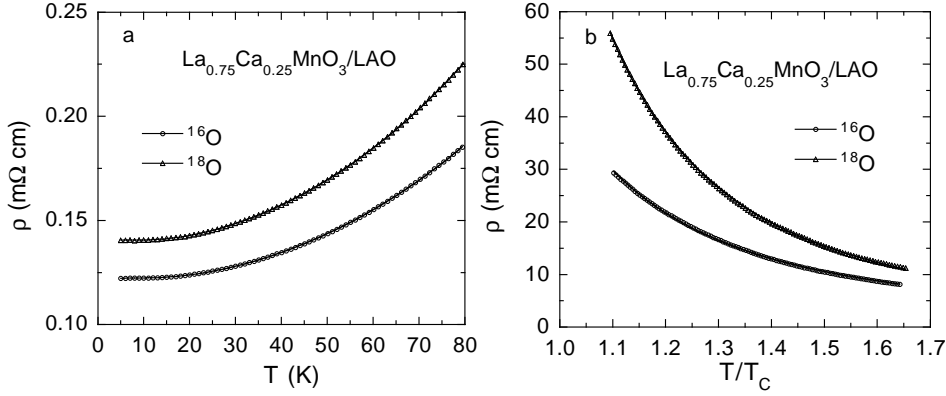


Figure 11.1: *Temperature dependence of the resistivity in the ferromagnetic (a) and paramagnetic (b) state in the oxygen-isotope exchanged thin film of $\text{La}_{0.75}\text{Ca}_{0.25}\text{MnO}_3$. The solid lines are the fitted curves.*

In the ferromagnetic state, the data can be perfectly fit by

$$\rho(T) = \rho_0 + BT^{4.5} + C\omega_s / \sinh^2(\hbar\omega_s/2k_B T).$$

Here ρ_0 is the residual resistivity, the second term arises from 2-magnon scattering, and the third term is associated with small-polaron coherent motion which involves a relaxation due to a soft optical phonon mode [7]. Such a soft mode is related to the tilt/rotation of the oxygen octahedra, and has a low frequency ($\hbar\omega_s/k_B \sim 80$ K). Both ρ_0 and the coefficient C should be proportional to the effective carrier mass m^* , and depend strongly on the oxygen isotope mass if the carriers in the ferromagnetic state is of small polaron type. Indeed, we find that both quantities increase by 15(3)% upon replacing ^{16}O with ^{18}O isotope. The result provides first experimental evidence for the presence of small polaronic carriers and their metallic conduction in the low temperature ferromagnetic state, and is in quantitative agreement with a CMR theory proposed by Alexandrov and Bratkovsky [6].

In the paramagnetic state, the data can be well fit by [8]

$$\rho = \frac{A}{\sqrt{T}} \exp(E_\rho/k_B T),$$

where $A = (ah/e^2\sqrt{k_B})(1.05W_p)^{1.5}/\hbar\omega_o$, W_p is the polaron bandwidth, $E_\rho = E_a + \Delta/2$, Δ is the bipolaron binding energy, E_a is the activation energy of small polaron hopping mobility. The quantity A should strongly depend on the isotope mass, and Δ is also isotope-mass dependent according to a theoretical model [6]. It is striking that, upon replacing ^{16}O with ^{18}O isotope, the parameter A decreases by 35(5)%, and E_ρ increases by 13.2(5) meV. The result is in quantitative agreement with the CMR theory by Alexandrov and Bratkovsky [6].

11.2.2 Oxygen isotope effects in cuprates

a) Charge-stripe ordering in $\text{La}_{1.94}\text{Sr}_{0.06}\text{CuO}_4$

One of the outstanding features in the high-temperature copper oxide superconductors is the formation of alternating spin and charge stripes below a characteristic temperature [9, 10]. Such a stripe phase is believed to be important to the understanding of the pairing mechanism of high-temperature superconductivity [11]. However, the microscopic origin of the stripe phase is still highly debated. It could be caused by purely electronic interactions and/or by a strong electron-phonon interaction.

Although there is increasing experimental evidence for the presence of a strong electron-phonon interaction in the cuprate superconductors, it is not clear whether this interaction is relevant for the formation of the stripe phase. For the colossal magnetoresistive manganites, a strong electron-phonon interaction plays an important role in the formation of the Jahn-Teller paired stripes (or charge ordering), as shown by a very large oxygen-isotope shift of the charge-ordering temperature in both $\text{Nd}_{0.5}\text{Sr}_{0.5}\text{MnO}_3$ and $\text{La}_{0.5}\text{Ca}_{0.5}\text{MnO}_3$ systems [12]. Therefore it is natural to expect that the stripe formation temperature in cuprates should also depend on the oxygen-isotope mass if lattice vibrations are strongly coupled to the charge carriers.

The x-ray absorption near edge spectroscopy (XANES) is a powerful technique to probe the local structure conformations for a system. There are two characteristic peaks in the XANES spectra of the cuprates, which characterize the local structures within and out of the CuO_2 planes. A parameter R is defined as $R = (\beta_1 - \alpha_1)/(\beta_1 + \alpha_1)$, where β_1 and α_1 are the intensities of two characteristic peaks observed by XANES. When a charge-stripe ordering takes place, a change in the local structures leads to a sudden increase in R below the charge-stripe formation temperature T^* . The identification of T^* by XANES has been tested in an extensively studied compound $\text{La}_{1.875}\text{Ba}_{0.125}\text{CuO}_4$ [13].

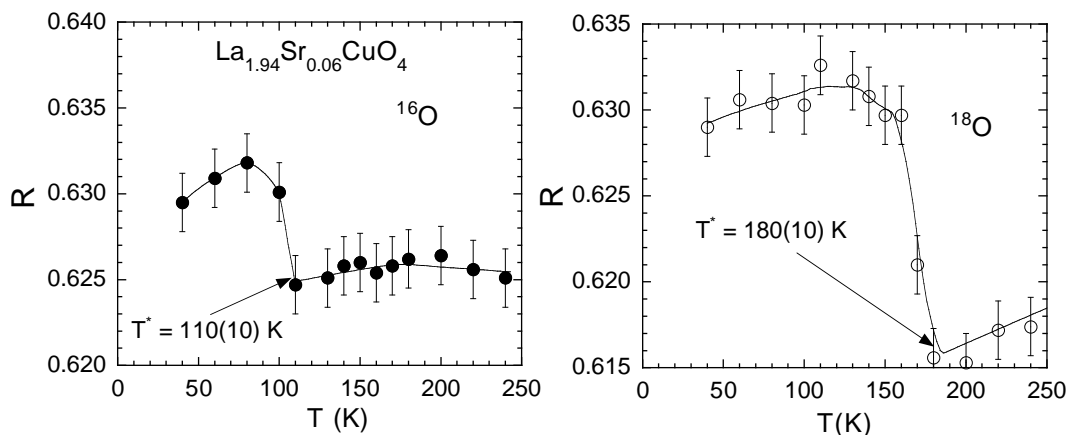


Figure 11.2: Oxygen isotope effect on charge-stripe ordering temperature T^* in $\text{La}_{1.94}\text{Sr}_{0.06}\text{CuO}_4$, as determined from XANES peak intensity ratio R (see text).

In Fig. 11.2, we show the temperature dependence of the parameter R for the oxygen isotope exchanged $\text{La}_{1.94}\text{Sr}_{0.06}\text{CuO}_4$. From the figure, one can clearly see that, upon replacing ^{16}O with ^{18}O , the stripe formation temperature T^* in this cuprate increases from about 110 K to 180 K. Such a huge oxygen isotope shift of T^* indicates that a strong electron-phonon interaction is likely to be involved in both the charge-stripe formation and the occurrence of high-temperature superconductivity.

b) Spin glass transition

There is increasing evidence that a strong electron-phonon coupling is present in the cuprates, which may lead to the formation of polarons (bare charge carriers accompanied by local lattice distortions). Several independent experiments have demonstrated that superconductivity and the underlying lattice vibrations are intimately linked. On the other hand, little is known about the influence of the electron-phonon interaction on magnetism in the cuprates. Conventional theories of magnetism neglect atomic vibrations; the atoms are generally considered as infinitely heavy and static in theoretical descriptions of magnetic phenomena, so there should be no isotope effect on magnetism. However, if charge carriers are polaronic, i.e., nuclear and electronic motions are no longer decoupled, one might expect isotope effects on magnetic properties. The question is whether such an isotope effect exists in the cuprates.

In order to answer this question we performed studies of the oxygen-isotope effect on the low temperature magnetism in $\text{La}_{2-x}\text{Sr}_x\text{Cu}_{1-z}\text{Mn}_z\text{O}_4$ ($x = 0.03, 0.05$; $z = 0, 0.02$) using the zero-field μSR technique [14]. These samples are in the so-called cluster spin glass regime. The pair of samples with different oxygen isotopes ^{16}O and ^{18}O were mounted on the two sides of the sample holder. This allows one to switch between the two isotope samples by rotating the sample holder without removing it from the cryostat, so the two isotope samples can be investigated at the same experimental conditions.

At low temperatures in all studied samples we observed damped oscillations due to muon-spin precession in local magnetic fields. A clear oscillation observed in ZF- μSR spectra implies that the muons sense a well defined internal magnetic field, in agreement with previous μSR measurements [15].

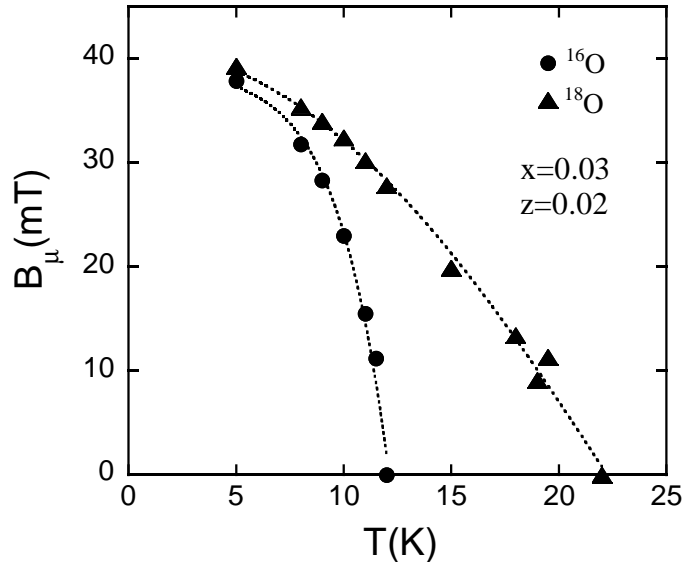


Figure 11.3: *Temperature dependence of the internal magnetic field at the muon site B_μ for the ^{16}O and ^{18}O samples of $\text{La}_{1.97}\text{Sr}_{0.03}\text{Cu}_{0.98}\text{Mn}_{0.02}\text{O}_4$. Dotted lines are guides to the eye.*

Fig. 11.3 shows the internal magnetic field B_μ for the two oxygen isotope (^{16}O and ^{18}O) samples ($x = 0.03$, $z = 0.02$) as a function of temperature. One can see that the spin glass freezing temperature T_g is strongly isotope dependent. The T_g of the ^{18}O sample is 10 K higher than that of the ^{16}O sample. This results in a huge value of the oxygen isotope exponent for the spin glass freezing temperature: $\alpha_{T_g} = -d\ln T_g/d\ln M = -6.0(7)$, which is the largest *negative* oxygen isotope exponent ever measured for any phase transition temperature. These novel isotope effects clearly demonstrate a strong effect of lattice vibrations on magnetism in cuprates which can be explained taking into account the polaronic nature of the charge carriers.

c) Magnetic penetration depth

Most oxygen isotope effect (OIE) studies performed on HTS were carried out on powder samples so far [16, 17]. In the small grains of these samples an almost complete oxygen isotope exchange by diffusion can be achieved. However, due to the strongly anisotropic nature of HTS (expressed in terms of the effective mass anisotropy $\gamma = \sqrt{m_c^*/m_{ab}^*}$) isotope experiments on single crystals are advantageous. Magnetic OIE studies on $\text{La}_{2-x}\text{Sr}_x\text{CuO}_4$ microcrystals with a mass of only 3 - 12 μg were performed during the last year [18]. SQUID magnetometry, which is the most commonly used technique for investigating magnetic properties of superconductors, is not sensitive enough for measuring such small samples. Therefore, a highly sensitive miniaturized torque magnetometer [19] (see also Annual Report 96/97) was used to perform all magnetic measurements. This device measures the magnetic torque $\vec{\tau} = \vec{m} \times \vec{B}_a$ acting on the magnetic moment \vec{m} of a HTS single crystal in an applied magnetic field \vec{B}_a .

Temperature-dependent torque measurements were performed at a fixed magnetic field $B_a = 0.1$ T and at an angle $\delta = 45^\circ$ of \vec{B}_a with respect to the c -axis of the sample. An example of these measurements carried out on an underdoped $\text{La}_{2-x}\text{Sr}_x\text{CuO}_4$ microcrystal (mass ~ 3 μg) with $x = 0.086$ is displayed in Fig. 11.4a. Clearly, an OIE on the critical temperature T_c is observed. The excellent reproducibility of the oxygen exchange procedure as demonstrated by the back-exchanged data (crosses) gives evidence that a complete isotope exchange by diffusion was achieved in this tiny single crystal.

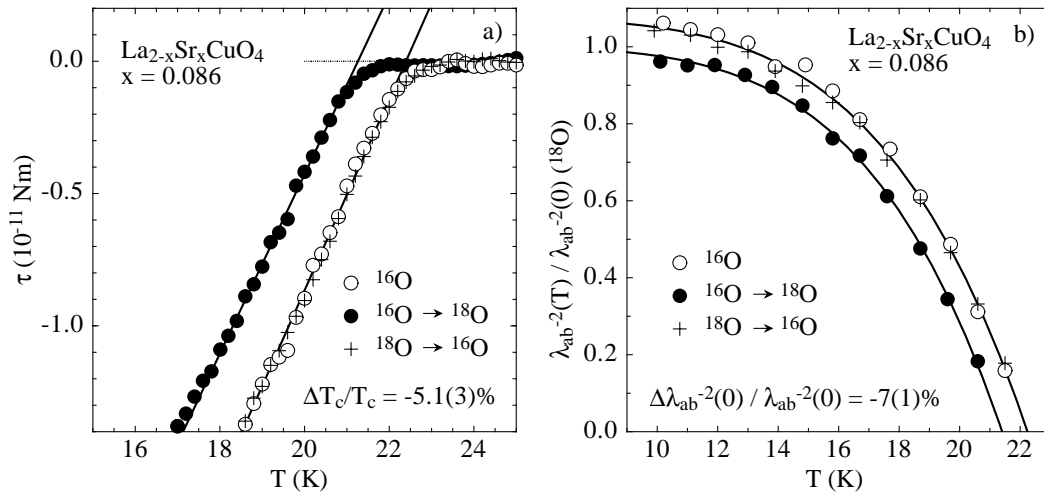


Figure 11.4: a) Magnetic torque τ versus temperature for $\text{La}_{2-x}\text{Sr}_x\text{CuO}_4$ with $x = 0.086$, showing the OIE on T_c . The reproducibility of the exchange procedure, as checked by the back-exchange (crosses), demonstrates a complete isotope exchange. b) Normalized in-plane penetration depth $\lambda_{ab}^{-2}(T)/\lambda_{ab}^{-2}(0)^{(^{18}\text{O})}$ for $\text{La}_{2-x}\text{Sr}_x\text{CuO}_4$ with $x = 0.086$. An OIE not only on T_c but also on $\lambda_{ab}^{-2}(T)$ is clearly seen.

The in-plane penetration depth $\lambda_{ab}(T)$ was extracted from field-dependent torque measurements performed at different temperatures $0.5T_c < T < T_c$ at an angle $\delta = 45^\circ$. $\lambda_{ab}(T)$ was determined from the logarithmic field dependence of $\tau/B_a \propto m$, characteristic for HTS in small fields [20, 21]. The normalized penetration depth $\lambda_{ab}^{-2}(T)/\lambda_{ab}^{-2}(0)^{(^{18}\text{O})}$ for the $^{16}\text{O}/^{18}\text{O}$ exchanged $\text{La}_{2-x}\text{Sr}_x\text{CuO}_4$ microcrystal with $x = 0.086$ is shown in Fig. 11.4b. Again, the OIE on T_c is clearly seen. Furthermore, a systematic shift of $\lambda_{ab}^{-2}(T)$ upon replacing ^{16}O by ^{18}O is observed. The value $\lambda_{ab}^{-2}(0)$ is determined by extrapolating the data to low temper-

atures, using the power law $\lambda_{ab}^{-2}(T) = \lambda_{ab}^{-2}(0)(1 - (T/T_c)^n)$ (solid lines). An oxygen isotope shift of $-7(1)\%$ is found. Many different experiments show that the change of the charge carrier density n_s during the oxygen isotope exchange procedure is negligible [17]. The excellent reproducibility of the isotope exchange gives further evidence that n_s is unaltered. We thus conclude that the observed OIE on $\lambda_{ab}^{-2}(0) \propto n_s/m_{ab}^*$ is due to an OIE on the effective in-plane mass m_{ab}^* of the charge carriers. This implies that lattice vibrations play an important role in the occurrence of HTS. A bipolaronic model of HTS [22] can quantitatively explain the OIE on m_{ab}^* .

d) EPR relaxation

A number of experiments on HTS suggest the possible existence of two quasiparticles: a heavy Jahn-Teller (JT) type polaron and a light fermion [23]. In the present study we performed electron paramagnetic resonance (EPR) experiments on $\text{La}_{2-x}\text{Sr}_x\text{CuO}_4$ ($0 \leq x \leq 0.20$) with different oxygen isotopes ^{16}O and ^{18}O . In order to observe the EPR signal, $\text{La}_{2-x}\text{Sr}_x\text{CuO}_4$ was doped with 2% of Mn^{2+} ions which replace the Cu ions in the copper-oxygen layer and serve as an EPR probe. The temperature dependence of the EPR linewidth was studied from 4 K to 300 K. Fig. 11.5 shows the EPR line observed in a $x=0.03$ sample with different

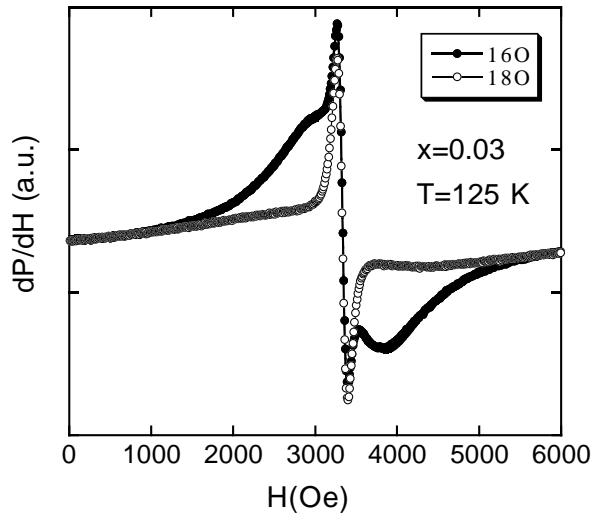


Figure 11.5: EPR signal of ^{16}O and ^{18}O samples of $\text{La}_{1.97}\text{Sr}_{0.03}\text{Cu}_{0.98}\text{Mn}_{0.02}\text{O}_4$ measured at $T=125$ K under identical experimental conditions. The solid lines represent the best fits using a sum of two Lorentzian components with different linewidths: a narrow and a broad one.

oxygen isotopes. First of all one should note that at this particular Sr concentration the EPR spectrum consists of two lines. We found that it can be well fitted by a sum of two Lorentzian components with different linewidths: a narrow and a broad one. One can see from Fig. 11.5 that the narrow line is not affected by the oxygen isotope substitution, while the linewidth of the broad signal exhibits a huge isotope effect. We found that at low temperatures the linewidth of the ^{18}O sample is almost twice larger than the one of the ^{16}O sample. We assign the narrow line to the light carriers and the broad one to the heavy polarons. With increasing doping the two EPR lines merge into a single EPR line, and the isotope effect on the linewidth gradually decreases towards optimum doping. Our results strongly suggest the presence of two quasiparticles in underdoped $\text{La}_{2-x}\text{Sr}_x\text{CuO}_4$. Moreover, the isotope effect observed on the EPR signal provides the first *microscopic* evidence for polaronic charge carriers in cuprate superconductors [24].

11.3 NMR/NQR studies of charge fluctuations in cuprates

One of the central issues in understanding cuprate-based HTS has been to determine in the CuO_2 planes the minimal number of electronic degrees of freedom which are necessary to describe the physics at the atomic scale. According to the so-called *single-spin fluid model* [25] only *one* spin degree of freedom would be necessary to describe the low-energy dynamics of the electronic system in the normal state of the HTS. However, as was discussed by various authors [26], this model might be an oversimplification.

This problem can be addressed by nuclear magnetic resonance (NMR) which probes the low-energy excitations of the HTS electronic system and separately provides information about the electronic structure of copper and oxygen. To examine whether a charge degree of freedom is present in the electronic dynamics, we studied the spin-lattice relaxation (SLR) of plane oxygen in $\text{YBa}_2\text{Cu}_4\text{O}_8$ by employing a recently developed double irradiation technique [27]. In this experiment two ^{17}O NMR spectra are compared, one obtained by starting from thermal equilibrium (standard spin-echo experiment), the other obtained by dynamic saturation of the $-1/2 \leftrightarrow 1/2$ NMR transition of the plane oxygen nuclear spin system. Charge fluctuations cause a quadrupolar contribution to the magnetically dominated SLR and this contribution, if present, will lead to an enhancement of the NMR line intensity at the inner satellite position during dynamic saturation.

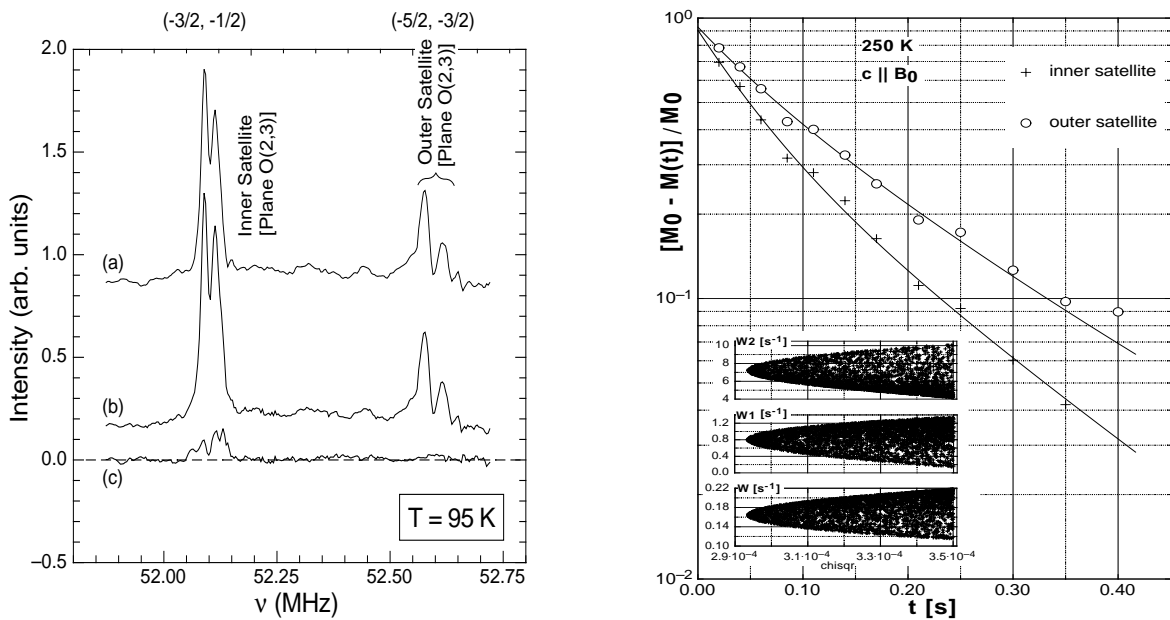


Figure 11.6: *Left:* ^{17}O central transition and high-frequency satellites of plane oxygen: (a) in a standard spin-echo experiment, (b) after dynamic saturation of the $(-1/2, 1/2)$ transition. (c) Difference of spectrum (b) and (a). *Right:* The best simultaneous fit of the multi-exponential magnetization recovery $M(t)$ as a function of W, W_1, W_2 to experimental data for inner and outer satellite. *Inset:* sets of W, W_1, W_2 values plotted versus χ^2 .

The left part of Fig. 11.6 shows a series of such spectra measured in oriented powder at $T = 95$ K with the magnetic field applied along the c axis. The remaining intensity at the inner satellite position in the difference spectrum clearly demonstrates that the SLR at the plane oxygen site in $\text{YBa}_2\text{Cu}_4\text{O}_8$ is not only driven by spin but also by charge fluctuations. We could show [28] that the origin of this low-frequency charge fluctuations is linked neither directly to phonons nor to electron-like quasiparticles. We can further rule out defect motion

of ions. Therefore, the substantial quadrupolar relaxation we observe has to arise either from strongly *correlated* quasiparticles as proposed by different theoretical models [29], or from very strong electron-phonon interactions that could lead to heavy polaronic-like quasiparticles [22, 30].

In addition, $\text{YBa}_2\text{Cu}_4\text{O}_8$ contains double Cu-O chains that present a good example of a quasi-one-dimensional (1D) electronic conductor, where non-Fermi liquid behavior due to strong electron-electron interaction is expected. If probed by NMR or nuclear quadrupole resonance (NQR) the chains do not exhibit simple metallic behavior. Instead, the chain Cu Knight shift varies linearly with temperature, T , rather than remaining constant, and the Cu SLR rate increases with T^3 [31] rather than being linearly dependent on T .

As shown in ref. [31] apex oxygen reflects the electronic behavior of the chain. Its magnetic shift scales with the chain Cu magnetic shift, but not with that of the plane Cu; thus indicating that the 2p apex orbitals only slightly overlap with the plane Cu 3d orbitals. On the other hand, SLR of apex oxygen scales neither with chain Cu nor with plane Cu but with the quadrupolar part of the chain Cu relaxation [31]. This implies that electric field gradient (EFG) fluctuations, presumably induced by charged quasi-particles in the chain, are responsible for the apex oxygen relaxation. Surprisingly, the two relaxation contributions of chain Cu, namely the charge induced quadrupolar and the spin induced magnetic relaxation, do not have the same temperature dependence. This fact points to separate dynamics for charge and spin that could, for instance, originate from a spin-charge separation expected in 1D conductors. Other explanations of course remain.

To confirm that the apex oxygen spin-lattice relaxation is indeed of quadrupolar origin, we performed two independent NMR experiments. The first is the application of the double-irradiation technique as described above in the case of plane oxygen. Our second experiment consists in measuring the magnetization recovery of the apex oxygen inner and outer satellites. In general, the recovery depends in a nontrivial way, besides the initial conditions, on magnetic (W) and quadrupolar (W_1, W_2) transition probabilities [32]. To fit the experimental data we performed a Monte Carlo simulation. For a randomly chosen W, W_1, W_2 set, we solved the so-called master rate equation and fitted the resulting multi-exponential magnetization recovery functions simultaneously to the two experimental magnetization recoveries. For each set, the optimal fit delivered its characteristic χ^2 value whose minimum determines the most reliable parameter set (see Fig. 11.6, right).

As in the double-irradiation experiment, we obtained that $W_2, W_1 > W$; so, the apex oxygen relaxation mechanism is predominantly quadrupolar with an unexpectedly small magnetic component. To better understand this interesting result, a detailed theoretical analysis is required.

11.4 Detection of small thermal effects in transition-metal oxides

In the past years, the physics of vortices in novel superconductors has been a matter of very active research [33]. The main focus in thermodynamic experiments on vortex matter has been to study of the first-order melting transition of the "static" vortex lattice, that has been explored in great detail in $\text{YBa}_2\text{Cu}_3\text{O}_{7-\delta}$ [34, 35]. However, depending on the details of the assumed mechanisms to describe the vortex state, a variety of other unconventional phase transitions may exist whose thermodynamics have not yet been explored experimentally [36]. In order to detect the small thermal and magnetic signals associated with vortex physics, we are performing high-precision magnetic and thermal experiments. The high sensitivity of our techniques allows us also to detect other small thermodynamic signals that occur in another physical context.

11.4.1 Lower critical point of the vortex-lattice melting line in $\text{YBa}_2\text{Cu}_3\text{O}_{7-\delta}$

We analyzed our thermal and magnetic data on the discontinuities in magnetization, ΔM , and entropy, ΔS , at the first-order vortex-lattice melting transition in low magnetic fields, as T approaches the critical temperature $T_c = 93.3$ K [37]. Both the magnetic $\Delta M(T)$ data and the $\Delta S(T)$ values from thermal measurements extrapolate to zero around $T/T_c = 0.995$. (T_c was obtained by fitting the corresponding melting field $H_m(T)$ to a power law, $H_m(T) = H_0(1 - T/T_c)^n$). The fact that $\Delta S(T)$ vanishes below the temperature where the melting lines extrapolate to zero might indicate that the first-order character of the phase transition is lost at a lower critical point, that would be located around $\mu_0 H = 80$ mT in our crystals. The large temperature difference between T_c and the temperature where ΔS vanishes (= 450 mK) does not seem to be related in an obvious way to our estimates for the "chemical" full width of the transition to superconductivity (50-100 mK). We therefore conclude that a lower critical point of $H_m(T)$ indeed does exist in our samples, that might be related to the amount and the character of the disorder in the crystals, as has been recently shown for the case of dilute columnar defects [38].

11.4.2 Investigations on other transition-metal oxides

We performed a number of experiments on other transition-metal oxides using our new high-resolution calorimeter in the temperature range 40-150 K. The apparatus has a resolution in heat of 5 nJ at 77 K. This allows us to start exploring the very challenging magnetic phase diagram of $\text{Bi}_2\text{Sr}_2\text{CaCu}_2\text{O}_8$ [36] with a thermal experiment. Unlike in the case of $\text{YBa}_2\text{Cu}_3\text{O}_{7-\delta}$, our first experiments on a 6 mg single crystal did not show any thermal features at the respective vortex-lattice melting transition, presumably because of homogeneity problems with the sample, and due to the fact that the expected thermal signals are of the order of the sensitivity limit of the apparatus.

Another new experimental setup operating in the temperature range 2-40 K is near completion within the framework of a diploma thesis. With this device we will be able to study some unexplored issues in the thermodynamics of certain low- T_c superconductors. Besides the very interesting thermal phenomena that we have already observed in cuprate superconductors [37], we also studied the effect of an oxygen isotope exchange (^{16}O vs. ^{18}O) on the specific heat at the phase transition from the tetragonal low-temperature phase to an

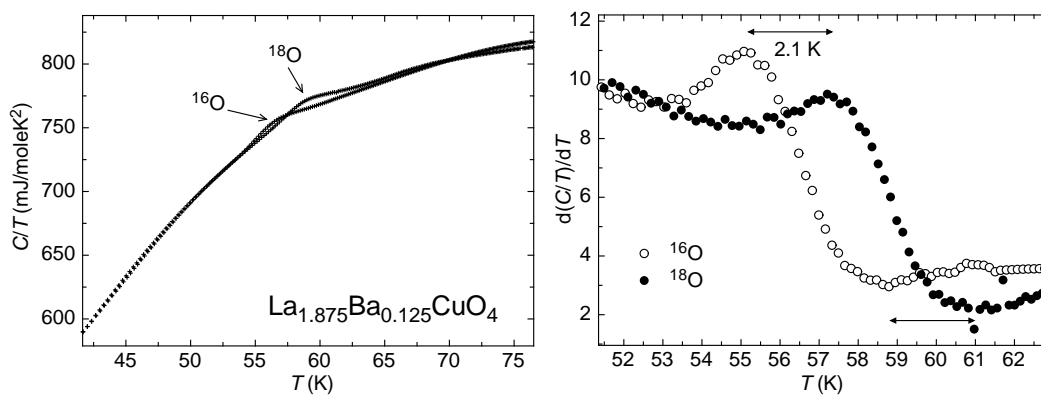


Figure 11.7: Reduced specific heats C/T of $\text{La}_{1.875}\text{Ba}_{0.125}\text{CuO}_4$ for samples containing the oxygen isotopes ^{16}O and ^{18}O (left figure). The right figure shows the corresponding temperature derivatives to better visualize the observed shift of the transition temperature.

orthorhombic phase in the non-superconducting compound $\text{La}_{1.875}\text{Ba}_{0.125}\text{CuO}_4$. This transition has been suggested to be closely related to an electronic phase transition or crossover in connection with the formation of charge stripes (see Sec.11.2.2). In Fig. 11.7 we show the corresponding anomalies in the specific heat that occur at $T = 56.7$ K and 58.8 K for samples containing ^{16}O and ^{18}O , respectively. We believe that the observed discontinuities in the specific heat mainly reflect the signature of the phase transition of the crystal lattice. They do not necessarily contain significant information about an associated change in the electronic structure, the contribution of which is expected to be much smaller than that of the crystal lattice. In analogy to a similar structural phase transition in La_2NiO_4 that is known to be very sensitive to changes in the oxygen sublattice [39], we conclude that the observed oxygen-isotope effect on the transition temperature in $\text{La}_{1.875}\text{Ba}_{0.125}\text{CuO}_4$ can be explained in a natural way by assuming a change in the lattice dynamics of this compound upon isotope exchange, thereby leading to a considerable shift of the observed transition temperature.

11.5 Critical phenomena in the cuprates

Different ordered physical systems, such as fluid, magnetic or superconducting systems, show a singular behavior (described by a power law) of different physical quantities near a critical point [40]. According to their critical behavior these systems are divided into universality classes. Several experiments show that the HTS belong to the 3D XY universality class [41]. During the last two years magnetic torque measurements were performed slightly below and above T_c in magnetic fields $B_a \leq 1.4$ T in order to study critical phenomena in the HTS [42]. In the critical regime of HTS several physical properties are described by a universal scaling function $Q_1^\pm dG^\pm(z)/dz$, where the scaling variable z depends on the temperature, the applied magnetic field B_a and the field orientation δ [21]. The superscript \pm refers to $T > T_c$ and $T < T_c$, respectively. For instance, the magnetic torque is given by $\tau(T, B_a, \delta) \propto Q_1^\pm dG^\pm(z)/dz$. As one can see from Fig. 11.8a, where angular-dependent torque measurements performed on different HTS single crystals are displayed, $Q_1^\pm dG^\pm(z)/dz$ changes its z -dependence drastically upon crossing the critical temperature T_c . The solid lines correspond to the following three limiting behaviors which can be derived analytically [21]: (i) $\lim_{z \rightarrow 0^-} Q_1^- dG^-(z)/dz \propto \ln(z)$ ($T < T_c$), (ii) $\lim_{z \rightarrow 0^+} Q_1^+ dG^+(z)/dz \propto z$ ($T > T_c$), (iii) $\lim_{z \rightarrow \infty} Q_1^\pm dG^\pm(z)/dz \propto \sqrt{z}$ ($T \rightarrow T_c$).

For intermediate values of z the scaling function can be experimentally derived by scaling the angular-dependent data recorded at different temperatures [42]. $Q_1^\pm dG^\pm(z)/dz$ versus z as obtained by this scaling procedure is shown in Fig. 11.8b for various HTS crystals with different anisotropy γ . The scaling functions obtained for the samples investigated deviate systematically with increasing γ from that of $\text{YBa}_2\text{Cu}_3\text{O}_{6.93}$ (Y-123), the sample with the smallest anisotropy. This may be understood in terms of a 3D-2D crossover which leads to non-universal behavior. A quasi-2D feature (the so-called ‘‘crossing point’’ [43]) is present in the scaling function for $z \text{sgn}(T/T_c) \sim -0.7$ where a crossover from the $\ln(z)$ -dependence to the \sqrt{z} -dependence is observed [42].

The $\sin(2\delta)$ signal observed for $T > T_c$ [*c.f.* Fig. 11.8a] yields information about the importance of fluctuations [42]. The amplitude of this signal shows a strong temperature dependence, which is well described by the 3D XY model. The torque signal vanishes at a temperature $T_0 > T_c$ where the $\sin(2\delta)$ amplitude changes its sign. For $T > T_0$ the paramagnetic background of the sample dominates, whereas for $T < T_0$ the fluctuation-induced diamagnetism exceeds the paramagnetic background. Therefore, the quantity $(T_0 - T_c)/T_c$ is a good measure for the importance of superconducting fluctuations. As clearly seen in Fig. 11.8c, fluctuations are more important in the underdoped regime, where γ becomes

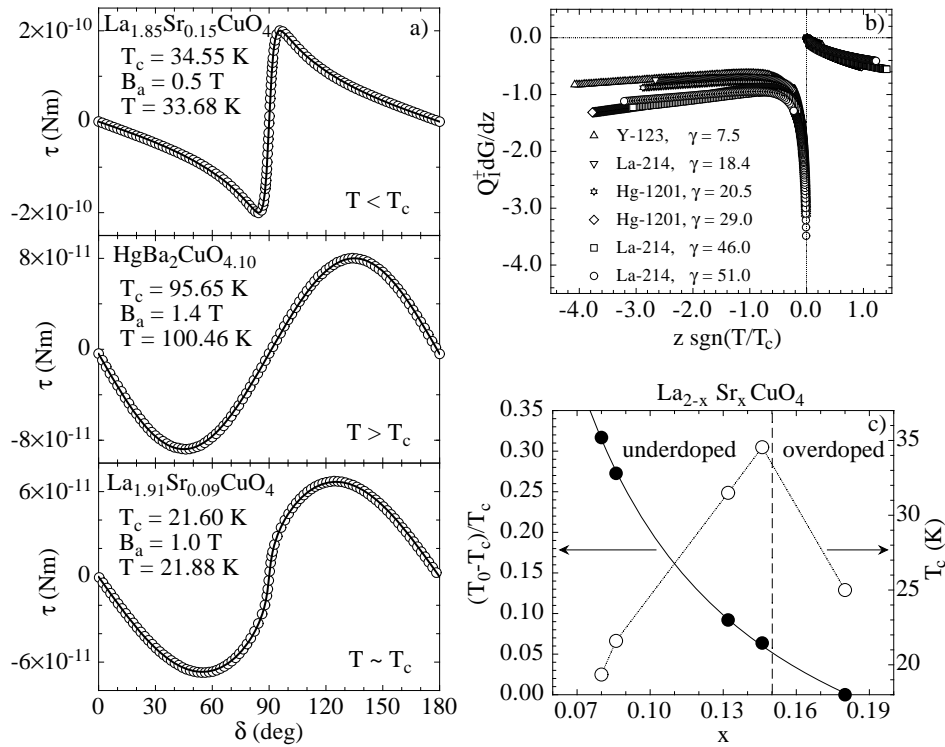


Figure 11.8: *a)* Angular-dependent torque measurements performed on HTS at temperatures $T < T_c$, $T > T_c$, $T \sim T_c$. Different angular dependences of the magnetic torque are observed in these three temperature regimes. *b)* Scaling function $Q_1^\pm dG^\pm/dz$ as a function of the scaling argument z for various HTS crystals with different anisotropy γ . The scaling function is obtained by scaling angular-dependent data recorded at different temperatures around T_c . The systematic deviations of $Q_1^\pm dG^\pm/dz$ with increasing γ can be explained by the fact that HTS are in a 3D-2D crossover regime. *c)* Critical temperature T_c and temperature T_0 (normalized as $(T_0 - T_c)/T_c$) below which the diamagnetic fluctuation signal exceeds the paramagnetic background (see text) as a function of Sr doping x for $\text{La}_{2-x}\text{Sr}_x\text{CuO}_4$ single crystals. Clearly, the importance of fluctuations increases in the underdoped regime, where γ becomes large.

large. Note that the observation of superconducting fluctuations above T_c clearly demonstrates the existence of preformed pairs. Thus, the physics of underdoped HTS seems to be dominated by fluctuations, and preformed pairs condense into the superconducting state (where they show a macroscopic phase coherence) at T_c .

11.6 Studies of superconductors with low-energy muons

Over the last 12 years μSR has demonstrated to be a unique and extremely powerful microscopic magnetic probe for the study of the complex vortex state in HTS, as well as for investigating local magnetic properties of related magnetically ordered systems. In many cases μSR has provided important information on the microscopic magnetic properties of these materials, which are hardly obtained with other experimental techniques. So far μSR studies have been performed using muons with energies in the MeV range, which require rather thick ($\approx 1\text{mm}$) samples for the muons to be stopped. Recently, Dr. Elvezio Morenzoni and his collaborators [44, 45] have developed a low-energy (LE) beam of spin polarized muons at the Paul Scherrer Institute (PSI), Switzerland, in order to circumvent this limita-

tion. Very slow muons with kinetic energy of ≈ 10 eV are obtained from the moderation of high-energy muons in a thin film of a condensed gas. These slow muons of tunable energy between 10 eV and 30 keV can be implanted at very small and controllable depth below the surface of a sample. This allows all the advantages of standard μ SR to be obtained in thin samples, near surfaces, and as a function of depth below surfaces (tunable muon energy). The spectrum of possible applications of the novel LE- μ SR technique is broad, including magnetic and superconducting thin films and structured materials, quasi two-dimensional magnetic systems, and new materials which can only be prepared in thin film form. It should be pointed out, that at present PSI is the only place in the world where LE- μ SR experiments are possible.

Perhaps the most beautiful demonstration of the power of LE- μ SR is the recent first direct observation of the spatial variation of the magnetic field (magnetic flux penetration) beneath the surface of a superconductor in the Meissner state [46]. This was achieved by applying a field parallel to the CuO_2 planes of an 700 nm thick epitaxial $\text{YBa}_2\text{Cu}_3\text{O}_{7-\delta}$ film and then measuring the field profile inside the superconductor by implanting LE muons at various depths (15 to 150 nm) by varying the implantation energy of the muons (≈ 3 to 30 KeV). The observed field profile is in excellent accordance with that expected for a thin film from London theory.

In the near future we plan to apply the LE- μ SR technique to investigate the complex magnetic phase diagram of $\text{Bi}_2\text{Sr}_2\text{CaCu}_2\text{O}_8$, including various vortex phases (vortex solid, vortex glass, vortex liquid). Over the past few years we have investigated these vortex states in the bulk of single-crystal $\text{Bi}_2\text{Sr}_2\text{CaCu}_2\text{O}_8$ by means of standard μ SR and SANS in great detail. Therefore, it is interesting to explore the vortex structure near the surface in thin films and single crystals with a microscopic probe, such as LE- μ SR. In particular, we plan to study vortex-lattice melting and the disorder crossover near the surface of the sample. Is the melting line near the surface and in the bulk the same? Does the melting line change with the thickness of the film? How does the flux-line structure change near the surface of a sample or in a thin film with the magnitude and orientation of the external field? In a further experiment we plan to study the influence of a transport current on the local magnetic flux distribution in a thin HTS film by means of LE- μ SR. This allows to investigate the effect of pinning on the flux-line motion on a microscopic scale.

11.7 Medical engineering

In our group, we started to work in the field of medical engineering. The scope of our work is to apply physical measurement techniques to medical problems. In our first project, we focus on ICP (Intracranial Pressure). Since the importance of continuous intracranial pressure measurements for patients after head injury was accepted, intracranial pressure is being used routinely in the management of neurosurgical patients. Several ICP monitoring systems were developed by various research groups. The most common used systems are the fluid filled ventricular catheter (ventricular measurement) and the fiberoptic device with a transducer at the tip (epidural or parenchymal). Although the methods were improved in the last ten years, there is still no highly accurate and reliable method, and there is still a risk of infections and injuries due to the invasion in the brain. There are efforts to develop a less invasive measurement technique to monitor the ICP during several days. In our project, in collaboration with Neurochirurgische Klinik, Ingolstadt, we consider a technique to monitor the ICP indirectly by a strain gauge sensor which measures the extension of the bone due to the pressure. The measurement of the bone extension was already demonstrated by an airspace experiment by NASA Research Laboratory, San Jose (USA). The strain gauge

sensor would be easily implantable and inexpensive. At the moment, we verify the accuracy, handling characteristics, and possible complications in a prospective study.

References

- [1] R. von Helmolt *et al.*, Phys. Rev. Lett. **71**, 2331 (1993).
- [2] S. Jin *et al.* Science **264**, 413 (1994).
- [3] A. P. Ramirez, J. Phys.:Condens. Matter **9**, 8171 (1997).
- [4] A. J. Millis, P. B. Littlewood, and B. I. Shraiman, Phys. Rev. Lett. **74**, 5144 (1995).
- [5] A. Moreo, S. Yunoki, and E. Dagotto, Science **283**, 2034 (1998).
- [6] A. S. Alexandrov, A. M. Bratkovsky, Phys. Rev. Lett. **82**, 141 (1999).
- [7] G. M. Zhao *et al.*, cond-mat/9912037.
- [8] G. M. Zhao *et al.*, cond-mat/9912355.
- [9] J. M. Tranquada *et al.*, Nature (London) **375**, 561 (1995).
- [10] H. A. Mook *et al.*, Nature (London) **395**, 580 (1998).
- [11] V. J. Emery, S. A. Kivelson, and O. Zachar, Phys. Rev. **B56**, 6120(1997).
- [12] G. M. Zhao, K. Ghosh, and R. L. Greene, J. Phys.:Condens. Matter **10**, L737 (1998); G. M. Zhao *et al.*, Phys. Rev. B **59**, 81 (1999).
- [13] A. Lanzara *et al.*, J. Phys.: Condens. Matter **11**, L541 (1999).
- [14] A. Shengelaya *et al.*, Phys. Rev. Lett. **83**, 5142 (1999)
- [15] Ch. Niedermayer *et al.*, Phys. Rev. Lett. **80**, 3843 (1998)
- [16] For a review see J.P. Franck, in: *Physical Properties of High Temperature Superconductors IV*, ed. D.M. Ginsberg (World Scientific, Singapore, 1994) (p189-293).
- [17] G.M. Zhao *et al.*, J. Phys.: Condens. Matter **10**, 9055 (1998).
- [18] J. Hofer *et al.*, preprint (cond-mat/9912493).
- [19] M. Willemin *et al.*, J. Appl. Phys. **83**, 1163 (1998).
- [20] D.E. Farrell *et al.*, Phys. Rev. Lett. **61**, 2805 (1988).
- [21] T. Schneider *et al.*, Eur. Phys. J. B **3**, 413 (1998).
- [22] A.S. Alexandrov and N.F. Mott, *Polarons and Bipolarons* (World Scientific, Singapore, 1995).
- [23] K.A. Müller *et al.*, J. Phys.: Condens. Matter **10**, L291 (1998).
- [24] A. Shengelaya *et al.*, submitted for publication to Phys. Rev. B
- [25] F.C. Zhang and T.M. Rice, Phys. Rev. B **37**, 3759 (1988).
- [26] V.J. Emery and G. Reiter, Phys. Rev. B **38**, 11938 (1988); J.P. Lu, Q. Si, J.H. Kim, and K. Levine, Phys. Rev. Lett. **65**, 2466 (1990).
- [27] A. Suter, M. Mali, J. Roos, and D. Brinkmann, J. Magn. Reson. **143**, 266 (2000).

- [28] A. Suter, M. Mali, J. Roos, and D. Brinkmann, (cond-mat/9907043).
- [29] V.J. Emery and S.A. Kivelson, *Physica C* **235–240**, 189 (1994); J. Ranninger and J.M. Robin, *Phys. Rev. B* **53**, 15657 (1996).
- [30] A.S. Alexandrov and N.F. Mott, *Rep. Prog. Phys.* **57**, 1197 (1994).
- [31] F. Raffa *et al.*, *Phys. Rev. B* **60**, 3636 (1999).
- [32] A. Suter, M. Mali, J. Roos, and D. Brinkmann, *J. Phys. Condens. Matter* **10**, 5977 (1998).
- [33] G. Blatter *et al.*, *Rev. Mod. Phys.* **66**, 1125 (1994) .
- [34] U. Welp *et al.*, *Phys. Rev. Lett.* **76**, 4809 (1996).
- [35] A. Schilling *et al.*, *Nature* **382**, 791 (1996).
- [36] M. F. Goffman *et al.*, *Phys. Rev. B* **57**, 3663 (1998).
- [37] A. Schilling *et al.*, *Phys. Rev. B* **61**, 3592 (2000).
- [38] W. K. Kwok *et al.*, to appear in *Phys. Rev.*
- [39] J. Rodriguez-Carvajal *et al.*, *Phys. Rev. B* **38**, 7148 (1988).
- [40] For an overview see *e.g.* Shang-Keng Ma, *Modern Theory of Critical Phenomena*, *Frontiers in Physics* **46** (W.A. Benjamin, Inc., Reading, Massachusettes, 1976).
- [41] S. Kamal *et al.*, *Phys. Rev. B* **58**, R8933 (1998); V. Pasler *et al.*, *Phys. Rev. Lett.* **81**, 1094 (1998).
- [42] J. Hofer *et al.*, *Phys. Rev. B* **60**, 1332 (1999); J. Hofer *et al.*, preprint (cond-mat/9912052).
- [43] P.H. Kes *et al.*, *Phys. Rev. Lett.* **67**, 2383 (1991).
- [44] E. Morenzoni *et al.*, *J. Appl. Phys.* **81**, 3340 (1997).
- [45] E. Morenzoni, *Physics and applications of low energy muons*, in *Muon Science*, S.L. Lee *et al.* Eds., IOP Publishing (1999).
- [46] T.J. Jackson *et al.*, to appear in *Phys. Rev. Lett.* (2000).

12 Surface Physics

T. Greber, J. Kröger, J. Wider, H. J. Neff, C. Cepek, W. Auwärter,
F. Baumberger, M. Hoesch, M. Muntwiler, R. Karrer, W. Deichmann, J. Osterwalder

In the surface physics laboratory we study well-defined surfaces of solid materials as well as adsorbed atomic and molecular monolayers and ultrathin films, prepared under ultrahigh-vacuum (UHV) conditions. In order to measure the geometric arrangement of the atoms within the first few monolayers of the surface we apply predominantly electron-based techniques such as x-ray photoelectron diffraction (XPD), medium-energy electron diffraction (MEED), low-energy electron diffraction (LEED), and more recently also scanning-tunneling and atomic force microscopy (STM/AFM). Angle-resolved UV photoelectron spectroscopy (ARUPS) gives us a detailed picture of the electronic band structure of such systems. Specifically, our experimental setup permits to directly map sections through the Fermi surface, which describes the electronic degrees of freedom relevant for transport properties, magnetic interactions and phase transitions. An important asset of such experiments is that the same probe (photoemission) gives us structural, electronic and magnetic information, and we can therefore study the interplay between these different degrees of freedom on the same sample.

Over the past year we have focused our interest on the following systems: Vicinal Cu(111) surfaces represent lateral nanostructures that can be easily prepared. We have studied the behaviour of the two-dimensional electron gas formed by a surface state in this well-defined and tunable potential energy landscape. For a hydrogen saturated Mo(110) surface, a missing link could be established between observed phonon anomalies and strong Fermi surface nesting. The structural characterization of monolayer hexagonal boron nitride films on Ni(111) has been completed, and the measurement of Fermi surface contours on this system has revealed that the presence of the film strongly modifies the Fermi surface of nickel near the interface. This finding is surprising and very important for the understanding of metal-insulator-metal tunneling junctions. The growth of Co clusters on this *h*-BN film has been characterized by STM, showing a variety of different morphologies that can be controlled by temperature and Co coverage. In a collaboration with Prof. M. Sancrotti (TASC Laboratory of the Istituto Nazionale per la Fisica della Materia, Trieste, Italy) the structural and electronic properties of C₆₀ monolayer films on Ag(100) have been investigated. Dr. R. Fasel and Dr. K.-H. Ernst of EMPA Dübendorf have studied the orientation of chiral 7-helicene molecules on various metal surfaces using the XPD capabilities in our surface spectrometer.

Concurrent with these ongoing studies, several new experimental techniques have been pushed forward. In the near-node photoelectron holography project, the first proof-of-principle experiment could be successfully completed during two weeks of beam time at the ALOISA beamline at the Sincrotrone ELETTRA in Trieste. Three near-neighbour shells in a (111) plane of an Al crystal could be imaged at atomic resolution. The development of our picosecond time-resolve MEED experiment has been further delayed due to problems with the sample alignment in the electron scattering chamber. Instead, we have begun to use our femtosecond Ti:sapphire laser system for developing two-photon photoemission (2PPE) spectroscopy in the same angle-mapping mode that we apply for ARUPS. First data measured on Cu(111) clearly show the dispersion of the Shockley surface state (see Section 12.8). These powerful measurement modes will give us unique capabilities for Fermi surface mapping at very low energies that can easily be extended to femtosecond time resolution. Our growing involvement in synchrotron radiation experiments is now fully underway. A new experimental chamber (COPHEE), which is designed to go eventually to the Surface and Interface Spectroscopy beamline of the Swiss Light Source after a temporary deployment to the APE beamline at the Sincrotrone ELETTRA, has produced first test spectra using a laboratory

UV source. A sophisticated extraction electron optical system remains to be designed and built, after which this experiment will permit the spin-resolved measurement of magnetic Fermi surfaces.

We have continued our collaboration with the surface chemistry group of Prof. J. R. Huber of the Physical Chemistry Department (P. Willmott, H. Manoravi, H. Spillmann) who have developed excellent thin film preparation capabilities using pulsed reactive crossed-beam laser ablation. They have grown single crystalline films of technologically relevant GaN and Ti:sapphire, and they were using our photoelectron spectrometer for surface composition analysis and for verifying the crystallinity of their films.

12.1 Surface states on vicinal Cu(111) surfaces

The Shockley (L -gap) surface state on the clean Cu(111) surface provides a low-density two-dimensional free electron gas, which has been used to study quantum interference phenomena in two dimensions [1]. This state is a consequence of the broken translational symmetry in the normal direction at the crystal surface, and it is located in the band gap of the surface-projected bulk bands. The wave functions propagate parallel to the surface and fall off exponentially both towards the vacuum and towards the bulk and are thus quasi two-dimensional. Single monoatomic steps on an otherwise flat surface are known to act as repulsive barriers for surface state electrons [2]. Artificial *periodic* structures of a size appropriate to observe quantum coherence effects are found conveniently on vicinal surfaces: A slight miscut relative to a high symmetry plane of a crystal leads to the formation of terraces bound by a regular step superlattice.

We have studied the Shockley surface state on Cu(332), a surface with a miscut of 10° and a mean (111) terrace length of $\ell = 12\text{\AA}$. The ARUPS data of Fig. 12.1a show the dispersion of the surface state along $\bar{\Gamma}\bar{M}$ (i.e. perpendicular to the steps). The parabolic dispersion

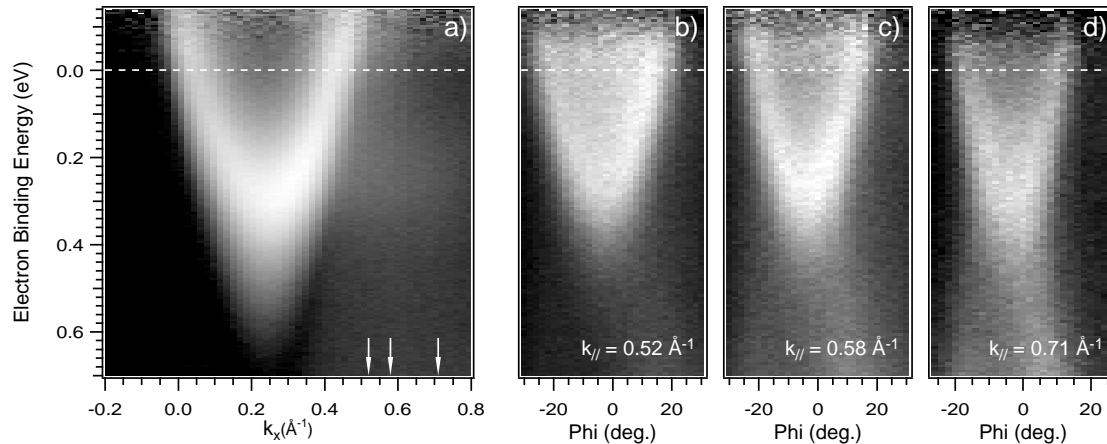


Figure 12.1: *Dispersion plots of the surface state related photoemission feature on Cu(332). a) Polar cut along $\bar{\Gamma}\bar{M}$ (logarithmic gray scale). The arrows indicate the $k_{||}$ -values for the measurements shown in (b)-(d), which represent azimuthal cuts in the direction perpendicular to that of (a).*

with an effective mass slightly larger than the value on flat Cu(111) indicates a propagating Bloch state in a periodic potential. The extra intensity on the right hand side of Fig. 12.1a around a binding energy of 0.24 eV is due to a non-dispersing surface state resonance. The

identification of this state as a one-dimensional resonance is confirmed by the azimuthal cuts for k_{\parallel} -values larger than $2\pi/\ell$, probing the dispersion of the surface state resonance along the steps (Figs. 12.1b-d). The parabolic dispersion with an effective mass equal to the one on flat Cu(111) indicates free propagation along the steps, while the constant binding energy perpendicular to the steps is a signature of localization in this direction.

12.2 Surface states and surface phonons: H/Mo(110)

In low-dimensional systems the electron-phonon coupling can lead to dramatic effects in the lattice dynamics, inducing strong phonon anomalies. Prominent examples are found on the (110) surfaces of W and Mo. Upon H adsorption, both surfaces show characteristic reductions of phonon frequencies at few and very specific phonon wave vectors. This effect is seen clearly in high-resolution electron energy loss spectra (HREELS) [3] and much more pronounced in helium atom scattering spectra [4]. Recent density functional theory (DFT) calculations [5] support the scenario of a giant Kohn anomaly: The dynamic screening of a specific surface phonon mode of wave vector \vec{Q}_c is dramatically enhanced if the Fermi surface exhibits strong nesting features, i.e. extended parallel sets of contours that can be connected with each other by a single nesting vector \vec{Q}_c . Such nesting features provide a large phase space for low-energy excitations that involve the formation of standing electron waves of the same periodicity as the specific surface phonon mode.

While the DFT calculations indicate such nesting features on H/W(110) and H/Mo(110), the experimental situation is less clear. For H/Mo(110) an earlier photoemission study was not able to confirm the nesting properties of the Fermi surface [6].

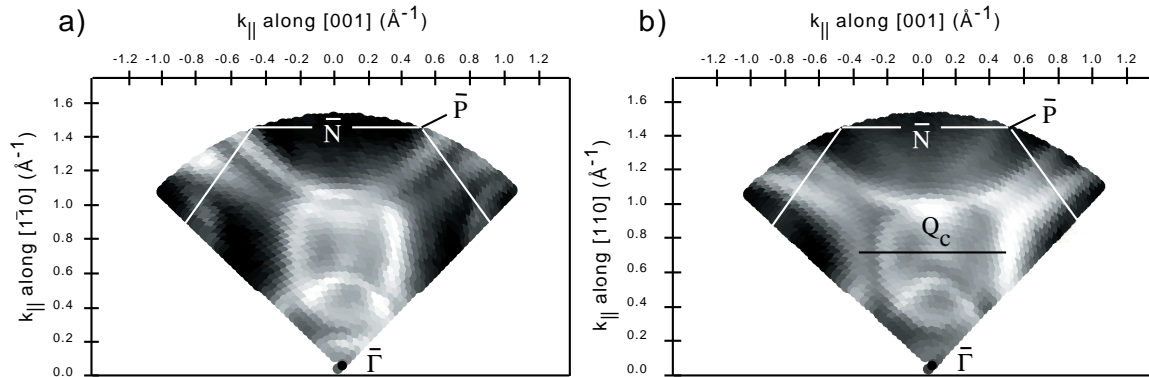


Figure 12.2: Sector of a high-resolution Fermi surface map of the clean (a) and the hydrogen saturated (b) Mo(110) surface. The photoemission intensity ($h\nu = 21.21\text{eV}$) at the Fermi level is plotted in a logarithmic grey scale as a function of k_{\parallel} . In both data sets the surface Brillouin zone is indicated as well as high-symmetry points. In b) the nesting vector \vec{Q}_c connecting extended parallel contours is indicated.

We have repeated this experiment on clean and H-saturated Mo(110), as is summarized in Fig. 12.2. The quarter-pie shaped plots in Figs. 12.2a and b present the high-resolution photoemission measurements of Fermi surface contours within a part of the surface Brillouin zone for the clean Mo(110) surface (a) and for the H-saturated surface (b). The most prominent H-induced change is the splitting off of a contour both on the right and left hand side of a strong bulk-related feature which is not affected itself by H adsorption. These split-off contours form, over a range of the order of 0.4\AA^{-1} , straight sections parallel to the $\overline{\Gamma N}$ direction and are thus strongly nested. The corresponding nesting vector measured from these

data amounts to 0.85\AA^{-1} . This is in excellent agreement with the nesting vector of 0.86\AA^{-1} found in the DFT calculation [5] and is fully consistent with the critical phonon wave vector of 0.90\AA^{-1} along the $\overline{\Gamma H}$ direction where the anomaly occurs [3, 4]. We observe similar nesting also perpendicular to the $\overline{\Gamma S}$ direction (not shown) where the comparison of Q_c yields values of 1.19\AA^{-1} (photoemission), 1.23\AA^{-1} (DFT [5]) and 1.22\AA^{-1} [3, 4]. These results provide therefore strong evidence that the mechanism of a giant Kohn anomaly applies for the occurrence of the phonon anomalies on the H-saturated Mo(110) surface.

12.3 Monolayer hexagonal boron nitride film on Ni(111): Thin film geometries from substrate photoelectron diffraction

Metal-insulator-metal structures are very important as tunneling junctions between any combination of normal metals, ferromagnets or superconductors. The ultimate junction is reached with a single monolayer of insulating material. Recently it was discovered that very stable monolayers of hexagonal boron nitride (*h*-BN) can be prepared by the reaction of benzene-like borazine $(\text{BN})_3\text{H}_6$ with Ni(111) at 1100K [7]. With the aim of studying the electronic and magnetic coupling across such films we characterized their growth by XPD and by STM. From the XPD analysis we learned that film growth stops before a second layer starts to form, and the STM images show large and defect-free film terraces [8]. By means of B 1s and N 1s core-level photoelectron diffraction the film structure was determined to be a graphite-like sheet with a slight corrugation of 0.1\AA and with the nitrogen atoms terminating the film surface. From this analysis using photoemission from within the film, the registry with the substrate could not be observed, because the electron backscattering off the Ni(111) substrate is extremely weak. However, due to the perfect order in the film, we were able to extract this information from the Ni 2p substrate photoelectron diffraction in the following way [9]:

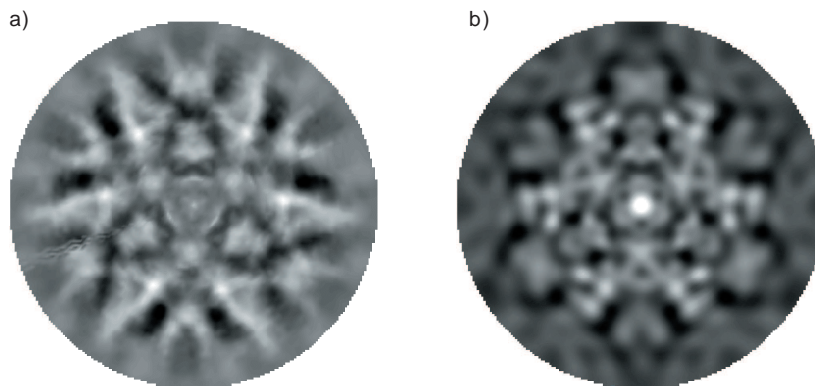


Figure 12.3: *Ni 2p photoelectron diffraction difference plots: In (a), the experimental Ni 2p XPD pattern from the clean Ni(111) surface ($E_{kin}=884$ eV) is subtracted from the corresponding pattern from the *h*-BN covered Ni(111) surface after suitable normalization. In (b), the same procedure has been applied to multiple scattering cluster calculations using three Ni(111) substrate layers with and without *h*-BN film.*

A Ni 2p photoelectron diffraction pattern is measured both for the *h*-BN covered Ni(111) surface and for the clean surface. The two measurements are suitably normalized and subtracted from each other in order to produce a signature for all scattering processes involving the film. The resulting difference pattern is reproduced in Fig. 12.3a. Unlike regular photoelectron diffraction patterns, where the strong forward focusing effect produces maxima along interatomic vectors, this data set does not give a direct clue to the positions of the atoms in

the film relative to those in the substrate. In substrate emission, atoms from all crystal layers below the surface contribute to the elastic photoemission signal, with an exponential decay away from the surface due to inelastic scattering. At the electron energies used in XPD, typically 10 to 20 atomic layers produce primary photoelectrons that reach the surface and that are coherently scattered by the upper layers and by the film. The difference pattern is therefore a complex superposition of all these coherent and incoherent scattering processes involving the film. By means of multiple scattering cluster calculations the same situation can be modeled by taking the difference of a cluster calculation including the h -BN film and one without. The calculations have been carried out for the three high-symmetry alignments of the film where nitrogen sits either on top or in an fcc or hcp hollow surface site. The best fit to the experimental data was obtained for the N-top site (Fig. 12.3b). Note that the fine structure in the data is modelled quite well, while the choice of grey scale representation makes the general appearance look less similar. However, a quantitative analysis using reliability factors confirms our conclusion, which agrees well with an earlier LEED study by Gamou et al. [10].

12.4 Influence of an atomic grating on a Fermi surface

The electronic structure in metal-insulator interfaces is investigated by means of ARUPS. The single layer h -BN film on Ni(111) described in the preceding section serves as a model system forming a well defined commensurate (1x1) structure [7, 8, 10]. Fig. 12.4 shows Fermi surface maps of (a) bare Ni(111) and (b) h -BN/Ni(111). They represent the photoemission intensity from the Fermi level as a function of emission angle. In order to probe the same initial states in reciprocal space (k -space) for the two samples, the photon energy was switched from 23.1 eV (He I β) for Ni(111) to 21.2 eV (He I α) for h -BN/Ni(111). This compensates for the work function reduction due to the formation of the h -BN layer.

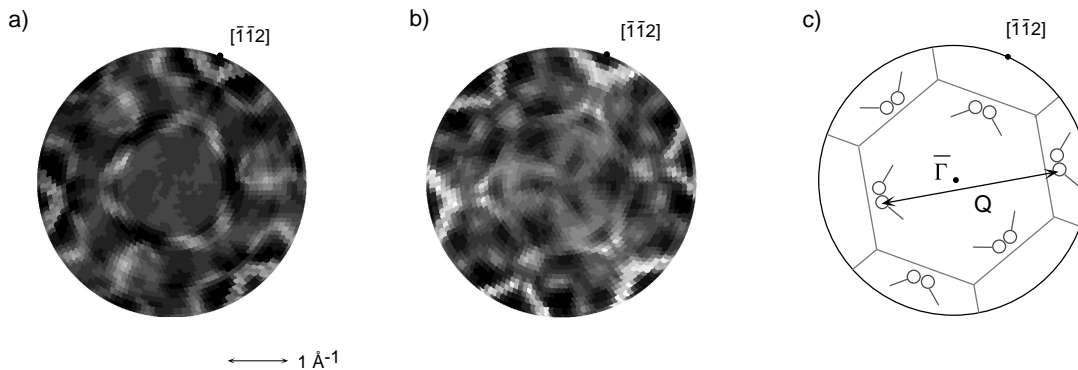


Figure 12.4: *Parallel-projected Fermi surface maps of (a) clean Ni(111) measured with He I β radiation and (b) h -BN/Ni(111) measured with He I α radiation. The high-symmetry direction $[\bar{1}\bar{1}2]$ is indicated. c) Schematic drawing of the surface Brillouin zones seen in (a) and (b). The signal disk like features (sp -bands) are replicated in the presence of h -BN by reciprocal surface lattice vectors \vec{Q} .*

In comparing Figs. 12.4a and b it can be seen that an insulating overlayer with no electronic states at the Fermi energy nevertheless influences strongly the shape of the Fermi surface in the surface region probed by photoemission. The Fermi surface contours remain three-fold symmetric but get distorted, and new features emerge. In Fig. 12.4c, the surface Brillouin zones covered by these data sets are sketched and particular features are highlighted. The

signal disk like features in Fig. 12.4c correspond to the sp band Fermi surface sheets of nickel which are spin split below the Curie temperature [11]. The most striking influence of the h -BN film is the replication of features of the bare nickel Fermi surface by surface umklapp processes as indicated by the reciprocal surface lattice vector \vec{Q} . This clearly reveals that h -BN acts as an atomic grating that modifies the Fermi surface and thus influences physically relevant quantities such as the tunneling characteristics across such junctions.

12.5 Towards well defined metal-insulator-metal junctions

Aiming at a better understanding of electronic and magnetic coupling in metal-insulator-metal (MIM) structures, a system consisting of cobalt clusters on a monolayer h -BN film on Ni(111) is investigated. The insulating h -BN serves as a well defined tunneling barrier [7, 8]. The growth of Co on this flat and defect-free substrate was studied by scanning tunneling microscopy (STM). A wide variety of growth morphologies are found according to the chosen evaporation parameters (see Fig. 12.5). In particular, island size and shape as well as the Co sticking coefficient are strongly temperature dependent. At room temperature (RT) clusters up to 10 Å height with only a few nanometers diameter are formed. They tend to arrange themselves in chains, which are aligned along crystallographic high-symmetry directions but not necessarily along steps. The reason for this alignment is not understood at the moment: STM images show no defects in the h -BN film, and magnetic effects are unlikely since reference measurements with Cu clusters (see inset of Fig. 12.5a) show also chain formation. Cobalt evaporation onto a heated substrate leads to triangular-shaped,

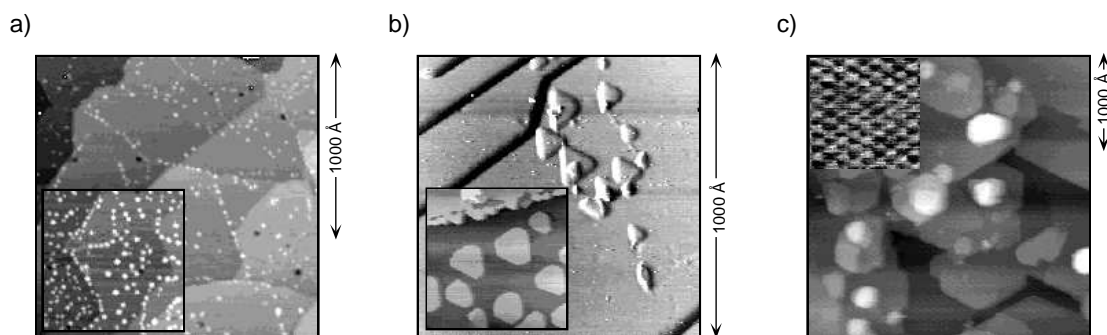


Figure 12.5: *STM images of Co growth on h -BN/Ni(111): a) The nanometer-size clusters arranged in chains originate from Co evaporation at room temperature. The inset displays Cu clusters deposited at RT on h -BN/Ni(111) showing a similar arrangement. b) Larger two-dimensional triangular-shaped Co islands are produced at 150°C. Evaporating Co on bare Ni(111) results in even larger, homogeneously distributed islands of quasi hexagonal shape (inset). c) At higher exposures Co grows three-dimensional. The inset demonstrates atomic resolution on Co.*

two-dimensional islands of several nanometers lateral size (Fig. 12.5b), in contrast to the RT clusters, which are imaged as round objects by the STM. The crystalline structure of these islands is confirmed by recent XPD measurements. Evaporating Co on bare Ni(111) under the same conditions (sample heated to 150 °C) results in even larger, strictly two dimensional islands with quasi hexagonal contours (Fig. 12.5b, inset). Thus, the h -BN layer influences the island growth. Depositing large amounts of Co onto the h -BN film resulted in a rather rough surface: Uncovered h -BN patches coexist with regions of three-dimensional Co islands. Annealing induces a flattening of the surface and a well ordered atomic structure is imaged by STM (Fig. 12.5c).

12.6 Electronic structure of K doped C_{60} monolayers on Ag(100)

In collaboration with M. Sancrotti, TASC-INFM Laboratory, Trieste, Italy

The charge transfer from a Ag(100) surface to a monolayer of adsorbed C_{60} is studied with high-resolution valence band photoelectron spectroscopy. With increasing potassium exposure the progressive filling of the band formed by the lowest unoccupied molecular orbital (LUMO) of C_{60} is observed (Fig. 12.6a). The charge transfer onto the C_{60} molecules is quantified from the observed binding energies of the LUMO derived band (Fig. 12.6b), which can accommodate a total of 6 electrons per C_{60} molecule. In the doping range where the occupancy of the LUMO is $n_{LUMO} < 3$, the LUMO shifts stronger in energy than the highest occupied molecular orbital (HOMO). This non-rigid band shift indicates that the C_{60} molecules get distorted below the LUMO half filling. Furthermore, the intensity of the HOMO is not constant but shows in normal emission a pronounced dip between half and complete LUMO filling (Fig. 12.6c).

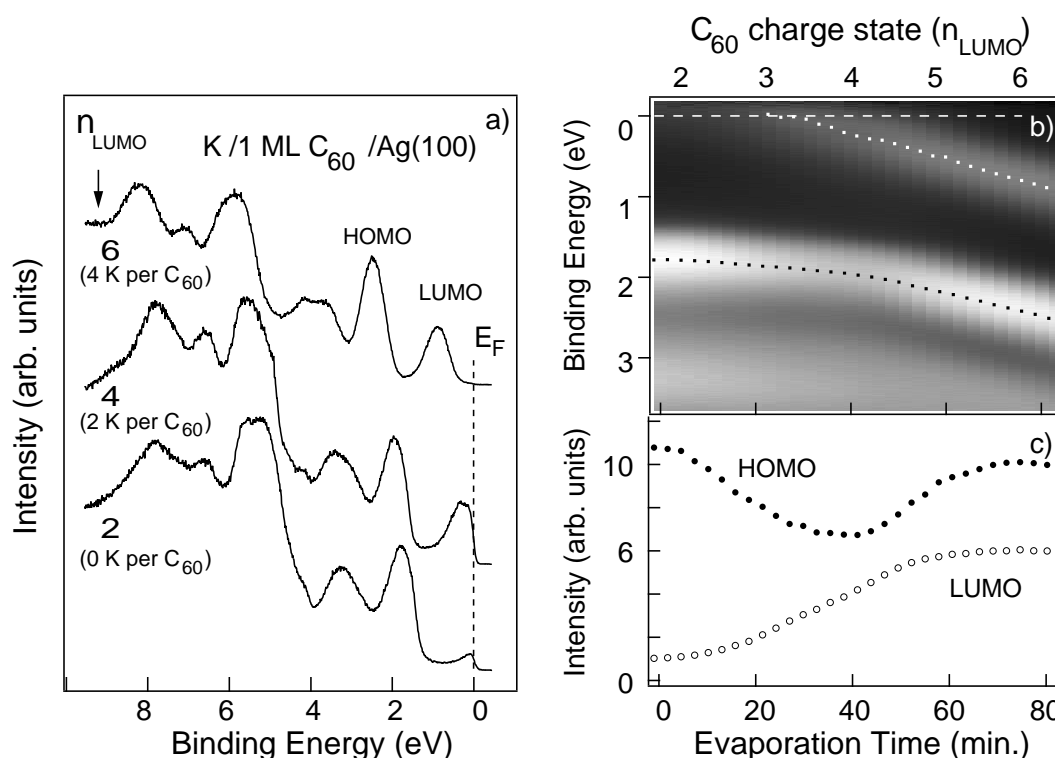


Figure 12.6: a) Valence band photoemission spectra from a C_{60} monolayer on a Ag(100) surface as a function of LUMO occupancy (n_{LUMO}) and potassium doping; b) Grey scale two-dimensional plot of valence band spectra given as a function of the binding energy and the C_{60} charge state. White and black dots refer to the C_{60} LUMO and HOMO peaks; c) Integrated intensities of the LUMO (white open circles) and HOMO (black dots) emission as a function of the K evaporation time.

A new method for the quantitative determination of the charge transfer onto C_{60} upon adsorption on a metal surface has been developed. We suppose a linear relationship between the K exposure and the occupancy of the LUMO (n_{LUMO}). Two reference points are determined from the evaporation time where the LUMO is half ($n_{LUMO} = 3$) and completely ($n_{LUMO} = 6$) filled. The LUMO half filling is identified from the crossing of the LUMO peak

maximum with the Fermi level, while the complete filling is found at the point where the photoemission spectrum does not show significant emission from the Fermi level [12]. For the undoped C_{60} monolayer on $Ag(001)$ the method indicates that 1.7 electrons are transferred from the substrate onto C_{60} .

12.7 Near-node photoelectron holography

In collaboration with the ALOISA beamline team at the Sincrotrone ELETTRA, Trieste, Italy

A photoelectron diffraction pattern results from the coherent superposition of a source wave produced by core-level photoemission and a multitude of waves scattered by near neighbour atoms in a single crystal surface. As such, it contains all the prerequisites of a hologram, which is unfortunately perturbed by strong forward scattering effects that dominate over the truly holographic interference features. Near-node photoelectron holography exploits the anisotropic nature of the electron source wave. If the intensity of the photoelectrons is measured close to a node of the source wave, the interference features are enhanced and the holographic reconstruction should lead to a three dimensional image with atomic resolution of the surrounding of the photoemitter [13].

In order to test the idea of near-node photoelectron holography we performed experiments at the ALOISA beamline at the synchrotron facility ELETTRA in Trieste, Italy. We measured Al 2s photoelectron diffraction patterns over a solid angle of nearly 2π in two different experimental geometries (Fig. 12.7c and d). In the near-node geometry (Fig. 12.7a) the angle γ between the polarization of the light $\vec{\varepsilon}$ and the direction of electron detection is 80° whereas in the far-node geometry (Fig. 12.7b) the intensities of the photoelectrons have been measured along the polarization. The holographic reconstruction of the near-node diffraction pattern clearly shows the atomic positions of nearest and next nearest neighbours (Fig. 12.7e). This is not the case in the far-node geometry (Fig. 12.7g). This experimental result indicates that near-node photoelectron holography is a promising way to determine atomic structures at surfaces in a direct way.

12.8 Angle-scanned two-photon photoemission on Cu(111)

Two-photon photoemission (2PPE) is a promising way for exploring occupied and unoccupied electronic states in the vicinity of the Fermi energy at surfaces. It can readily be extended to study excited state lifetimes and dynamics. For such experiments we exploit our femtosecond laser system in combination with the angle-scanned photoemission experiment. Frequency-doubled 400 nm pulses from a Nd:vanadate pumped Ti:sapphire laser with a pulse duration of 80 fs and with 0.6 nJ energy at a repetition rate of 80 MHz are used. The laser light enters a window of the UHV photoemission chamber and is focused on the sample surface. For a surface with a typical work function of 4-5 eV, a single photon ($h\nu = 3.1\text{eV}$) is insufficient to excite photoelectrons into the vacuum. In these short pulses, however, the peak power is high enough to produce a considerable amount of two-photon absorption, such that the 2PPE spectrum can be measured.

First 2PPE data taken on clean Cu(111) are shown in Fig. 12.8a, where the spectrum along the surface normal is shown. A Fermi edge is observed at the upper end of the spectrum, as well as a peak near 0.4 eV binding energy that can be identified as the Cu(111) Shockley surface state (see Section 12.1). The peak at the lower end of the spectrum is due to secondary electrons and maybe also due to single-photon photoemission of thermally excited electrons.

In Figure 12.8b, electron energy distribution curves for 60 different emission angles are plotted in a grey scale. Clearly the dispersion of the Shockley surface state is observed. The

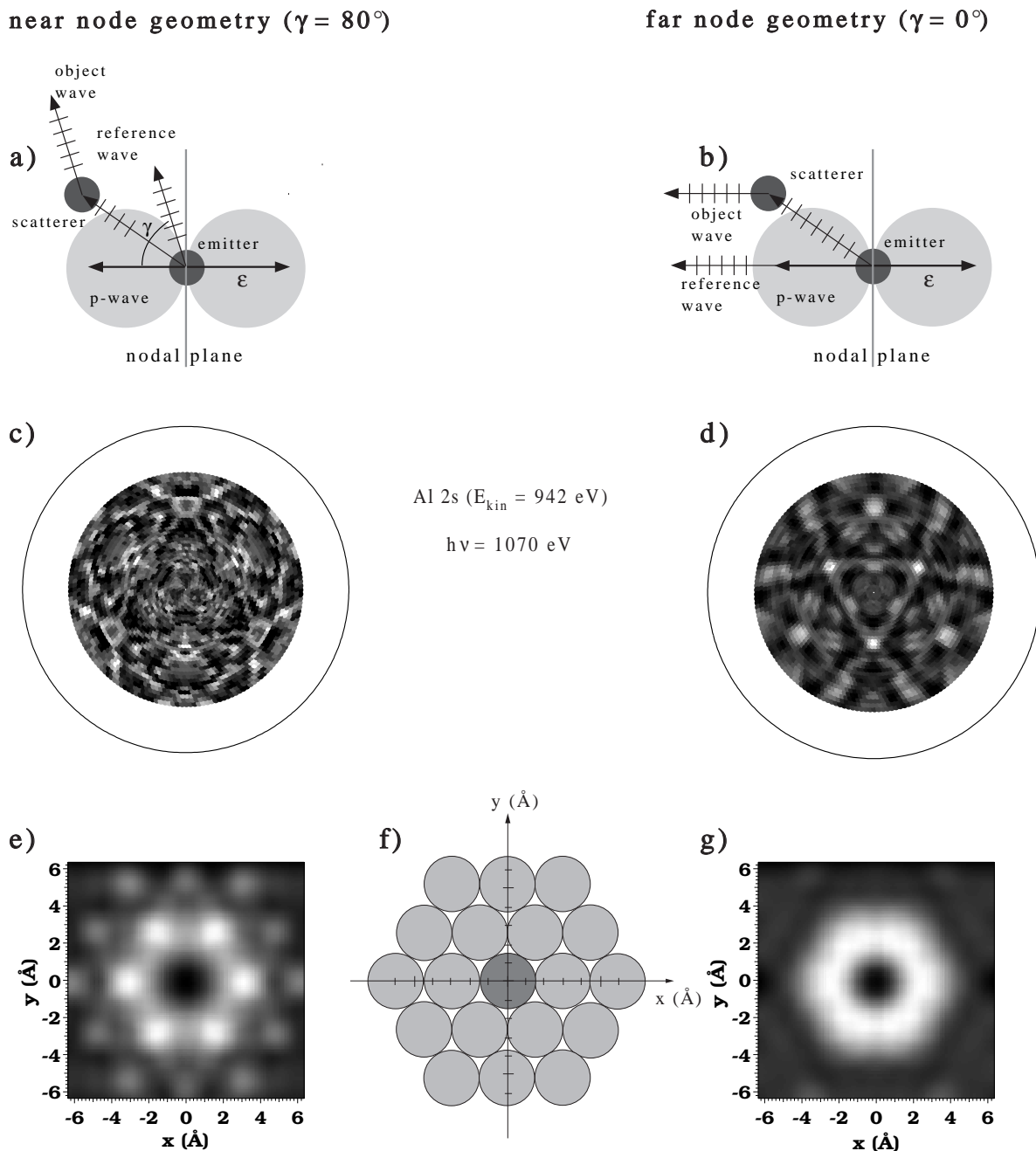


Figure 12.7: (c) and (d) Experimental Al 2s ($E_{kin} = 942$ eV) photoelectron diffraction patterns from a clean Al(111) single crystal for two different orientations of the light polarization $\vec{\epsilon}$ relative to the electron detector. In the near-node geometry (a) the electron intensity is recorded close to the nodal plane of the outgoing p wave whereas in the far-node geometry (b) the electrons are measured perpendicular to the nodal plane. (e) and (g) show corresponding holographic reconstructions within a plane parallel to the surface that contains the emitter. In the near-node image (e) nearest and next nearest neighbours are clearly resolved while in the far-node image (g) the positions of the atoms can not be determined. (f) Hard sphere model of a (111) plane of an Al crystal. The dark disk in the center represents the emitting atom.

shift of the secondary electron cut-off in going from normal emission to higher polar angles is due to the the inner potential that photoelectrons have to overcome in order to propagate into the vacuum (total internal reflection).

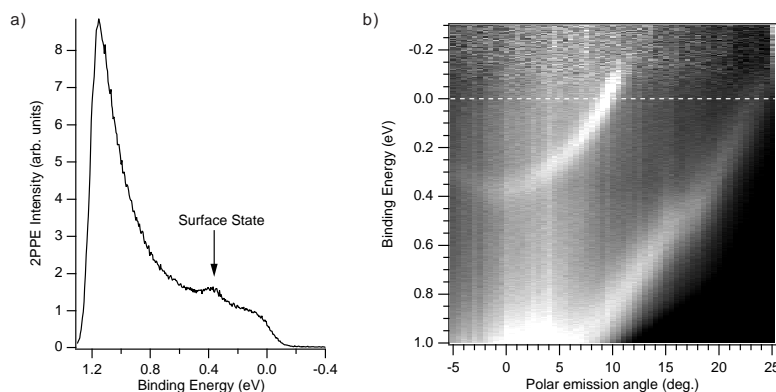


Figure 12.8: *Angle-resolved two-photon photoemission spectra from Cu(111) ($2h\nu = 6.2$ eV, bias voltage = -3.0 V). a) Energy distribution curve at normal emission. The peak at 385 meV binding energy arises from the Shockley surface state. b) Angle-scanned energy distribution curves for 60 different emission angles. The intensities are displayed in a linear gray scale.*

Our electron analyzer has a low transmission for low-energy electrons. Therefore we accelerate the photoelectrons for sensitivity reasons by an electric field that is provided by a negative bias voltage applied to the sample. This field violates parallel momentum conservation for the photoelectrons. The known dispersion of the Shockley surface state (see section 12.1) can be exploited as a reference for the recalibration of the parallel momentum.

12.9 Spin-resolved Fermi surface mapping

In 1999 the setup of a new experimental station running under the ambitious name of *C*OMplete *P*HOtoEmission *E*xperiment *C*OPHEE) began, which will be used for spin-resolved photoemission studies with synchrotron radiation. UV photoelectrons are energy analyzed and angle selected by a commercial hemispherical analyzer at high energy resolution and then spin analyzed by Mott scattering. The manipulator used for Fermi surface mapping allows the rotation of the sample to cover the whole hemisphere above its surface. Therefore spin analysis needs to be performed along all three directions of space to reconstruct the full polarization vector. This is achieved by two independent Mott polarimeters. After setup and tests at the Surface Physics Laboratory at the Irchel, the spectrometer will be used at the APE beamline at the Sincrotrone ELETTRA Trieste. Later the whole system will be moved to the Surface and Interface Spectroscopy (SIS) beam-line of the Swiss Light Source at PSI Villigen (under construction).

The home-made variable-temperature sample goniometer (T. Greber) is mounted vertically on the vacuum chamber. A preparation chamber provides standard equipment for sample cleaning, preparation and characterization (LEED) as well as sample transfer to the preparation facilities of the SIS beamline. Below is the μ -metal analysis chamber, which holds a gas-discharge UV-lamp, a twin-anode x-ray tube (Mg K_α and Si K_α) and the photoelectron spectrometer EA125 from Omicron Vakuumphysik GmbH. The electrostatic beam deflection system is currently under development. The two 60 keV Mott detectors were constructed at St. Petersburg Technical University [14]. They employ electrostatic acceleration and focus-

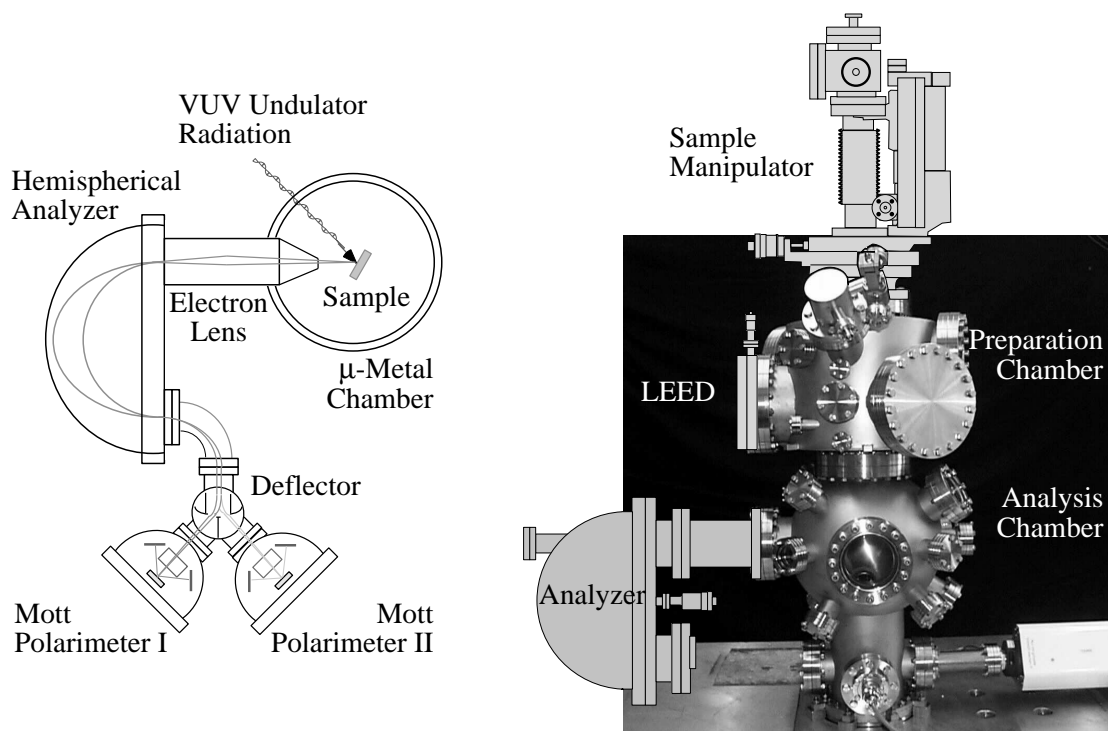


Figure 12.9: Schematic drawing and current status of the setup of COPHEE.

ing, back-scattering off a 80 nm thick gold foil and energy sensitive detection by four silicon surface barrier detectors for each unit.

References

- [1] see e.g. M.F. Crommie, C.P. Lutz and D. M. Eigler, *Science* 262 (1993) 218.
- [2] L. Bürgi, O. Jeandupeux, A. Hirstein, H. Brune and K. Kern, *Phys. Rev. Lett.* 81 (1998) 5370.
- [3] J. Kröger, S. Lehwald, H. Ibach, *Phys. Rev. B* 55, 10895 (1997).
- [4] E. Hulpke, J. Lüdecke, *Surf. Sci.* 287/288 (1993).
- [5] B. Kohler, P. Ruggerone, S. Wilke, M. Scheffler, *Phys. Rev. Lett.* 74, 1387 (1995).
- [6] R. H. Gaylord, K. H. Jeong, S. D. Kevan, *Phys. Rev. Lett.* 62, 2036 (1989).
- [7] A. Nagashima, N. Tejima, Y. Gamou, T. Kawai, and C. Oshima, *Phys. Rev. B* 51, (1995) 4606
- [8] W. Auwärter, T.J. Kreuz, T. Greber, J. Osterwalder, *Surf. Sci.* 429 (1999) 229
- [9] M. Muntwiler, Diplomarbeit, Uni Zürich (1999)
- [10] Y. Gamou, M. Terai, A. Nagashima, and C. Oshima, *Sci. Rep. RITU, A* 44 (1997) 211
- [11] T.J. Kreuz, T. Greber, P. Aebi, J. Osterwalder, *Phys. Rev. B* 58 (1998) 1300
- [12] M. Merkel, M. Knifer, M. S. Golden, J. Fink, R. Seemann and R. L. Johnson, *Phys. Rev. B*, 47 (1993) 11470, P. J. Benning, P. Stepniak and J. H. Weaver, *Phys. Rev. B*, 48 (1993) 9086
- [13] T. Greber, J. Osterwalder, *Chem. Phys. Lett.* 256 (1996) 653 (1996) 653.
- [14] V.N. Petrov, M. Landolt, M.S. Galaktionov, B. V. Yushenkov, *Rev. Sci. Instr.* 68, (1997) 4385

13 Physics of Biological Systems

Hans-Werner Fink and Cornel Andreoli

This project is currently in the process of being established. It is devoted to employing physics tools and concepts to understand and modify molecular objects with a main emphasis on the physics of biological systems. Questions related to Structural Biology and the interfacing of bio-molecules with silicon microstructures to obtain novel physical objects that exhibit new and useful properties are among the central themes of our efforts.

Our electron point source exhibits unique properties in respect to brightness and coherence. We employ the coherent electron waves to image and manipulate bio-molecules in a lens-free holographic microscope, that we named the LEEPS (Low Energy Electron Point Source) microscope.

The low energy of the electrons, although a great benefit in avoiding radiation damage as commonly observed in conventional electron microscopes, makes this tool also susceptible to external ac-magnetic fields and building vibrations. In order to achieve optimal resolution, well below the nanometer regime, the coherent electron waves have to be protected from external disturbances. Construction work for a suitable laboratory environment is presently planned and we expect that the beginning of the winter-semester 2000 completes it.

The holographic record of an individual molecule contains the complete information about the amplitude and the phase of the object wave and it is thus possible to gather 3-dimensional information about the object. In collaboration with scientists from a CNRS laboratory in Marseille, we plan to develop a fast numerical algorithm for the hologram reconstruction to obtain the full object information during the experiment in an on-line modus. With this, a proper constructed laboratory environment and a newly designed electron detector, we expect to be able to routinely address questions of structural biology. One of the important goals will then be to work on appropriate sample preparation methods in collaboration with colleagues from the biochemistry department of our University to obtain structural details on specific proteins.

In-situ studies of the growth of clusters on carbon nanotubes, their charging properties as well as the direct observation of the dynamics of charge hopping processes in quasi insulating bio-polymers are other topics of our current interests.

We could recently obtain the first direct evidence for the electrical conductivity of DNA molecules, which has triggered quite some expectations to use DNA molecules in molecular devices. At the March meeting 2000 of the American Physical Society, there is a special session on DNA conductivity and a related press conference on possible future DNA based electronic devices. While we will not be in the position to employ sophisticated silicon technology, we still plan and hope to maintain a leading role in this emerging field since we have the unique ability to actually see the "DNA-wires" on a device. In view of silicon device fabrication, we are assured of the assistance of the mesoscopic physics groups at the University of Basel as well as of the ETH Zurich. A small biotechnology company in Jena has recently offered its assistance in providing us with partially structured membrane chips that they produce specific to our needs by optical lithography. The final structuring of the membranes on a sub-micron scale, the arrangements of the DNA molecules and the contacts to them should then take place in our laboratory once we shall have an ion-milling instrument available.

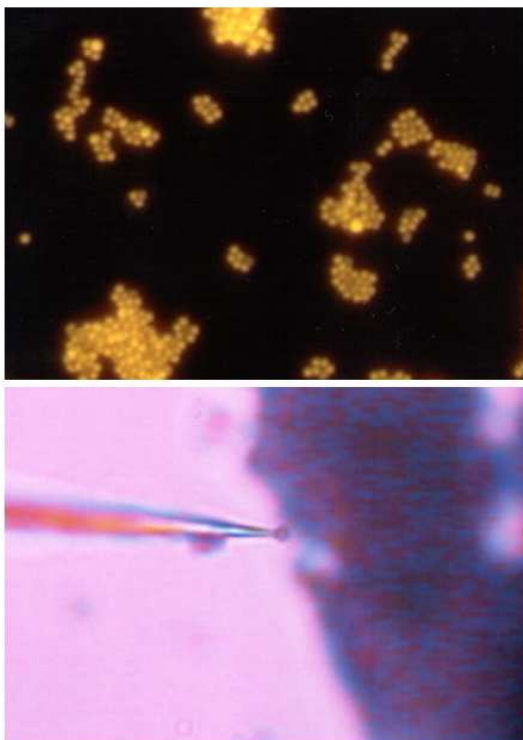


Figure 13.1: Light optical microscopy images of one-micron diameter fluorescent latex spheres clustered on a silicon nitride membrane (top). Manipulation of a single latex sphere with a glass pipette (bottom). At a later stage, the latex spheres should be attached to the end of DNA molecules via a biotin streptavidin bond. The mechanical manipulators will then be used to move the spheres (and the "invisible DNA") to the desired places on the membrane. Holographic imaging of the DNA and electrical measurements will subsequently be carried out in the LEEPS microscope.

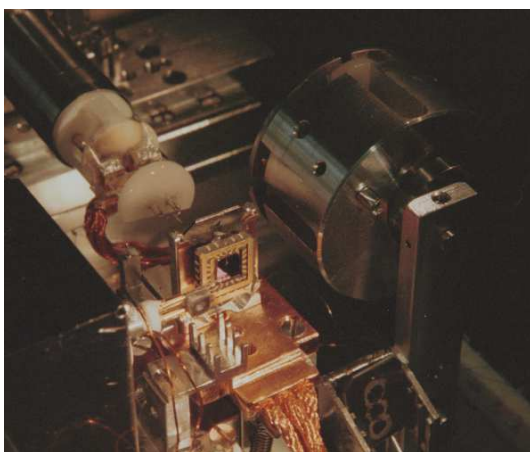


Figure 13.2: Inside view of the Low Energy Electron Point Source (LEEPS) Microscope for imaging and manipulating individual molecules.

14 Computer Assisted Physics

S. Dangel, P.F. Meier, H.-R. Moser, S. Pliberšek and Y. Shen
P. Hüsser (until Sept. 99) and J.M. Singer (until Dec. 99)

The research activities of the Computer Assisted Physics group have focussed this year on the following productive areas

- Large-scale cluster calculations of the electronic structure of materials exhibiting high-temperature superconductivity
- Time series analysis of electroencephalograms with methods developed in the frame of nonlinear dynamics (“chaos research”).

In particular we report on hyperfine interactions at copper and oxygen nuclei in La_2CuO_4 (Sec. 14.1) and on the changes in the microscopic structure induced by dopants (Sec. 14.2). From the collaborations with two groups of the Medical Faculty we present results of a new analysis of sleep EEG and the discrimination of different sleep stages (Sec. 14.3)

14.1 Electronic structure of high- T_c materials: hyperfine interactions

Nuclear quadrupole resonance (NQR) spectroscopy is one of the most productive experimental procedures which non-invasively monitors electron density modifications in high-temperature superconductors with changes in temperature. The method indirectly measures the electric field gradient (EFG) at nuclei with spin ($I > 1/2$) and hence sensitively reflects the details of the total electron density distribution in the neighbourhood of these nuclei. Electron density distributions in solids can be calculated using first-principles cluster calculations and an estimate of our confidence in their accuracy can be assessed by calculating the EFG at chosen nuclei and then comparing them with values derived from NQR spectra. Of course, once the wave functions have been determined the way is open to the calculation of other physical properties. This should provide a good method of correlating which properties are important in deciding superconduction.

The calculated quantities are ground-state properties of the solid and depend sensitively on how charge is distributed within the lattice. Nuclear magnetic resonance (NMR) investigations of the Knight shift and the various nuclear relaxation rate tensors as a function of temperature, doping, and orientation of the applied field with respect to the crystalline axes, provide an additional insight into the static spin density distribution and the low frequency spin dynamics of the electrons in the normal as well as in the superconducting state. Owing to the varied abundances of nuclei with suitable nuclear magnetic and quadrupole moments, most of these quantities can be studied on different sites in the unit cell. This allows one to distinguish static and dynamic features in the CuO_2 planes from those in the interlayer region.

Despite of the rich information of NQR and NMR results about the nature of the spin fluid and the low-energy quasiparticles, there exist only few theoretical first-principles approaches which address the determination of electric-field gradients (EFG) and magnetic hyperfine interactions. Therefore, we have recently carried out [1, 2] cluster calculations on two of the simplest materials which exhibit high temperature superconductivity (HTS), $\text{YBa}_2\text{Cu}_3\text{O}_7$ and La_2CuO_4 . These materials have different structures and composition and should help to elucidate the important features of the electronic structure necessary for superconduction.

The general idea of the cluster approach to electronic structure calculations of properties which depend upon predominantly local electron densities is that the parameters that characterize a small cluster should be transferable to the solid and largely determine its properties.

The essential contributions to EFGs and to magnetic hyperfine fields are given by rather localized interactions and therefore it is expected that these local properties can be determined and understood with clusters calculations. Approximations must be made concerning the treatment of the background that is employed to embed the cluster. Using as large a cluster as is possible is of course advantageous. It is necessary, however, that the results obtained should be checked with respect to their dependence on the cluster size.

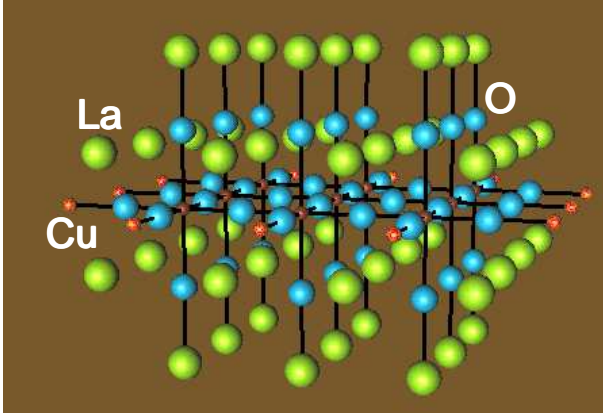


Figure 14.1: $Cu_9O_{42}/Cu_{12}La_{50}$ cluster.

We have performed spin-polarized calculations [3] for clusters Cu_nO_m comprising $n = 1, 2, 4, 5,$ and 9 copper atoms in a plane. The largest cluster, $Cu_9O_{42}/Cu_{12}La_{50}$, is shown in Fig. 14.1. All 663 electrons of 9 Cu and 42 O atoms are treated with an extended basis set whereas the positively charged 12 Cu and 50 La ions at the border of the cluster are represented by bare pseudo-potentials.

The variations of the values of the EEG and the dipolar hyperfine interaction parameters at the Cu and the planar O sites with respect to cluster size and multiplicity are within reasonable bounds and agree well with experimental data.

On the other hand, the calculated values for the Fermi contact interaction, $D(Cu)$, vary strongly with cluster size and position of a particular Cu atom in larger clusters. In Fig. 14.2 the values $D(Cu_i)$ are plotted versus N , the number of nearest-neighbor Cu atoms of Cu_i . It is obvious that the increase of the contact field is linear in N :

$$D(Cu) = a + bN, \quad (14.1)$$

with an on-site field $a = -1.75$ and a transferred field $b = 0.69$ (atomic units). It was known that in diluted copper salts the contact field at the Cu nucleus is negative. In these

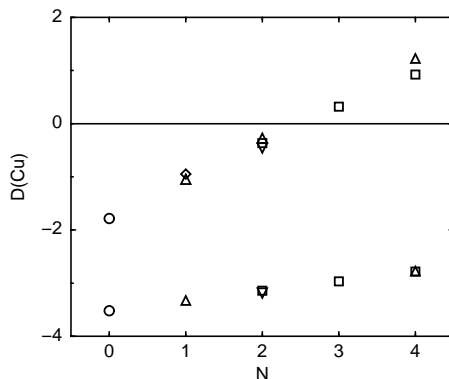


Figure 14.2: Difference between spin-up and spin-down densities at Cu vs. number of nearest neighbor Cu atoms, N , for different sites in various clusters with n Cu atoms. Circles: $n = 1$, diamonds: $n = 3$, triangle down: $n = 4$, triangle up: $n = 5$, squares: $n = 9$. Density functional (Hartree-Fock) values correspond to the upper (lower) data set.

substances the Cu ions are far separated from each other so that the effective number of nearest neighbours is $N = 0$. In the measurements on HTS, however, a positive value of $D(\text{Cu})$ was observed. There each Cu ion has $N = 4$ nearest Cu neighbours. Mila and Rice explained this positive value with a transferred hyperfine field. As seen in Fig. 14.2 cluster calculations allow us a study of the artificial cases of $N = 1, 2$, and 3 as well. This demonstrates nicely the power of computer simulations.

Similarly, there is also a transferred hyperfine field on the planar oxygen nuclei. We could show, however, that this field is due to nearest neighbours only and that contributions from next nearest neighbours are marginal. This implies that the assumptions made by Zha et al. to reconcile the neutron scattering and NMR data are not justified.

In Fig. 14.3 we show the spin density along the O-Cu-O-Cu-O-Cu-O bonds as calculated for the cluster $\text{Cu}_5\text{O}_{26}/\text{Cu}_8\text{La}_{34}$. The maxima correspond to those of the squares of the Cu $3d_{x^2-y^2}$ -orbitals. Close to the copper nuclei one observes the effect of the core-polarization.

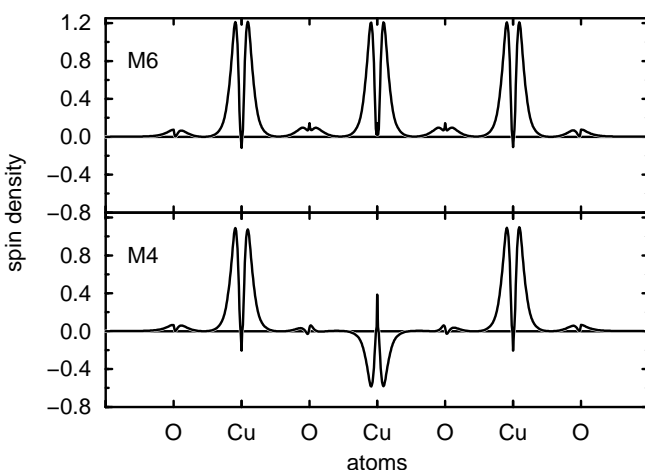


Figure 14.3: *Difference in spin densities along the O-Cu-O-Cu-O-Cu-O bonds as calculated with the density functional method for the cluster $\text{Cu}_5\text{O}_{26}/\text{Cu}_8\text{La}_{34}$. Top: multiplicity $m = 6$ (ferromagnetic alignment). Bottom: $m = 4$ (antiferromagnetic alignment).*

14.2 Electronic structure of high- T_c materials: influence of dopants

The material La_2CuO_4 is an insulator which becomes superconducting only upon alloying on the La site or changing the oxygen content. There is therefore considerable interest in understanding the changes in the local electronic structure that the various dopants induce. Doping in this sense means replacement of a La atom by a Sr atom, e.g., or introducing excess oxygens.

The modifications in the microscopic structure when a Sr replaces a La cannot be adequately studied with conventional band-structure calculations. The cluster approach, however, enables one to work out the local differences between undoped and doped structures in great detail. The ^{63}Cu NQR spectrum of the parent compound displays a single, narrow peak at 33 MHz [4]. Upon doping with Sr an additional (B) peak arises [5], displaced to higher frequencies with respect to the main (A) peak by 2 – 3 MHz. When pure La_2CuO_4 is doped with excess oxygen a similar behaviour is observed [6], namely a development of a secondary peak with a 3 – 4 MHz shift from the main peak. We have calculated [7] the changes in the EFG at the copper site that occur when a La with a bridging apical O to the Cu is replaced by Sr. With the density functional method, an increase of 10 % was obtained, in nice agreement with the experimentally observed NQR frequency of the B-line that is about 8 % higher than that of the A-line. Moreover, applying the cluster approach to the study of excess oxygens (which enter interstitial sites, see Fig. 14.4) we could explain

the existence of the NQR B-lines in $\text{La}_2\text{CuO}_{4+\delta}$. It is evident that the squeezing in of the interstitial oxygen $\text{O}(i)$ into the interstice will cause a relaxation of the four apical oxygen atoms in the immediate neighborhood. Therefore we used those positions of the $\text{O}(a)$ which also minimized the energy of the cluster. An energy minimum was found for a tilt of the $\text{O}(a)$ by 16° for which the EFG is 11 % larger than in the undoped case [7]. The close agreement of the frequencies of the satellite peaks in strontium- and oxygen-doped lanthanum cuprate is therefore only accidental; they have different physical origins.

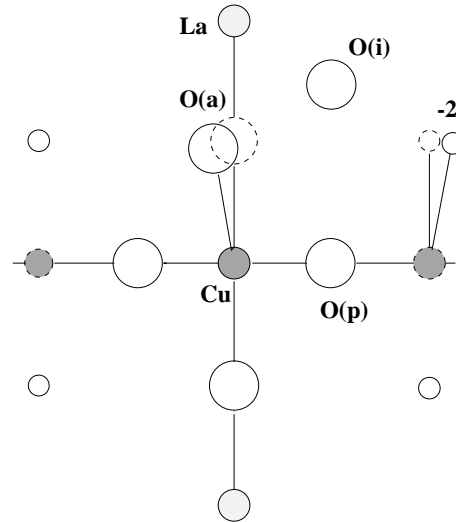


Figure 14.4: *Illustration of the atomic sites in the plane $y = 0$ for the cluster model with an interstitial oxygen $\text{O}(i)$ and the induced relaxation of the apical oxygens $\text{O}(a)$.*

14.3 Time series analysis of sleep EEG

We continued our collaboration with the Department of Neurology of the Medical Faculty where our analysis was directed principally towards using non-linear dynamical methods to predict epileptic seizures. A new collaboration has been established by attempting to interpret the EEG's which have been recorded in the Sleep Laboratory of the Institute of Pharmacology of our University (Prof. A. A. Borbély).

The scalp electroencephalogram (EEG) represents the summed synaptic activity from large groups of neurons primarily from the cerebral cortex and has led to widespread application to sleep research [8]. Sleep can be divided into two major components:

1. REM (Rapid Eye Movement) sleep
2. non-REM sleep, which itself has four identifiable stages, 1, 2, 3 and 4. Here, stages 1 and 2 are collectively labelled as "light sleep" and stages 3 and 4 correspondingly as "deep sleep".

Whereas deep sleep is characterized by slow-wave activity, REM sleep is distinguished by the slow waves being desynchronized from higher wave frequencies.

According to the neurophysiological generating mechanism of the EEG, the EEG signals stem from a highly nonlinear system indicating that non-linear methods of analysis are entirely appropriate in the study of the processes underlying sleep regulation. In this framework, the complexity of the sleep EEG can be estimated by calculating the correlation dimension D_2 . The D_2 of the synchronized EEG in slow-wave sleep should be lower than values for the desynchronized EEG in REM sleep [9]. However, random fractal noise with $1/f^{-\beta}$ spectrum has also a finite correlation dimension [10], and the scalp EEG exhibits such random fractal structure. On the other hand, although the surrogate-data test indicates nonlinear elements

in EEG dynamics [11], it does not support a low-dimensional deterministic picture. Since the source of the nonlinearity could arise from stochastic processes we apply, in addition to the dimensional analysis, multifractal-analysis in the framework of turbulence and related multiscale phenomena to the EEG data.

Table 14.1: *Dimensional, monofractal and multifractal measures of the 3-min. episodes from the sleep EEG.*

	REM sleep	Light sleep	Deep sleep
D_2	9.13 ± 0.67	8.19 ± 0.34	6.35 ± 0.52
H_2	0.08 ± 0.05	0.21 ± 0.03	0.45 ± 0.01
τ_2	-0.09 ± 0.02	-0.22 ± 0.07	-0.13 ± 0.02

Two all-night sleep EEG data sets from C3-A2 derivation have been analyzed to date. 30 artifactfree 3-min.-episodes for each sleep stage were selected. Initially the correlation dimensions D_2 of these EEG-episodes were calculated using time-delay embedding combined with a SVD (Singular Value Decomposition)-filter to help reduce the white-noise as shown in Table 14.1. As expected, the deep sleep phase has a significantly lower dimension than the light sleep phase. The so-called Hurst-exponent H_2 of these EEG-episodes was then calculated to characterize the nonstationary behavior of the signals. This can be extracted subsequently from the scaling behaviour of the structure function. However, here it was estimated by the method of detrended fluctuation analysis (DFA)[12], which is used to detect and quantify the long-range correlation within a non-stationary time series. The advantages of DFA are that it can eliminate the nonstationary external trend. The Hurst-exponent H_2 is related to the exponent α from DFA with $H_2 = \alpha/2 - 1$. However it should be noticed that DFA is sensitive to artifacts with short duration (See Fig. 14.5). From Table 14.1 and Fig. 14.5 there is clearly a negative correlation between the values of D_2 and H_2 , when considering EEG-episodes at different stages. This is the expected behaviour of a stochastic system with power-law spectra, $D_2 = \max(\frac{1}{H_2}, M)$, where M is the embedding dimension. The DFA method is appropriate for the study of monofractal signals since monofractal signals are homogeneous and have linear properties. EEG, like other physiological signals, are generated by complex self-regulating systems that process inputs with a broad range of characteristics. Additionally the surrogate-data test has shown nonlinear properties of the EEG dynamics, so it is meaningful that we apply multifractal analysis to the EEG signals. The multifractality is quantified through the

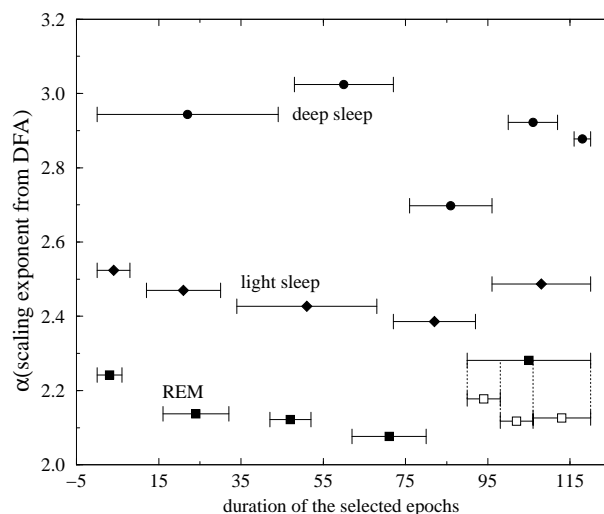


Figure 14.5: *Scaling exponent α as obtained from a detrended fluctuation analysis for the five longest episodes for each sleep stage. The length of the bar indicates the duration of the episode. The high value of $\alpha \approx 2.3$ for the REM epoch at the right is due to two large artifacts. After dropping these artifacts the analysis yields smaller α values for the three shorter episodes (open squares) as shown below the longer episode.*

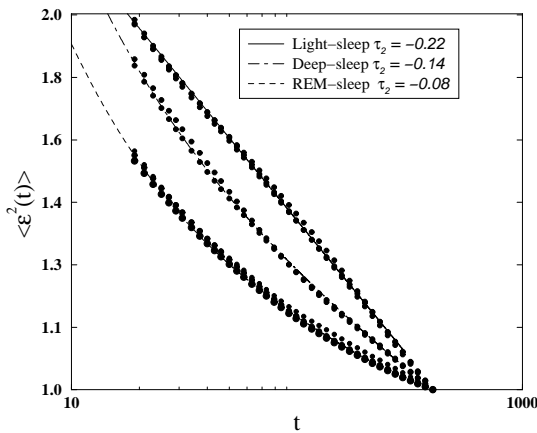


Figure 14.6: *Multifractal measure scaling: $\log \langle \epsilon^2 \rangle$ vs. $\log(t)$ for 3 different episodes of REM sleep, 2 episodes of light sleep and deep sleep. The curves are fits to a Γ -like function and yield for the strength of the multifractality the values $\tau_2 = -0.08, -0.22$, and -0.14 , respectively.*

exponent τ_2 extracted from the scaling behaviour of the multifractal measure $\langle \epsilon^2 \rangle$, in turn calculated from the gradient field of the original signals. The scaling behaviour can be fitted to a straight line for large τ_2 or a Γ -like function for small τ_2 [13]. These results are displayed in Table 14.1 and Fig. 14.6. We find both H_2 and τ_2 can discriminate the sleep stages, when we pay attention to the influence of artifacts.

As a preliminary conclusion, a combination of nonlinear deterministic and stochastic methods would seem to offer optimistic future for this type of EEG analysis.

References

- [1] P. Hüsser, E.P. Stoll, H.U. Suter, and P.F. Meier, *Physica C* **294**, 217 (1998).
- [2] H.U. Suter, P. Hüsser, E.P. Stoll, S. Schafroth, and P.F. Meier, *Hyperfine Interactions*, **120**, 137 (1999).
- [3] P.Hüsser, H.U. Suter, E.P. Stoll, and P.F. Meier, *Phys. Rev. B* **61**, 1567 (2000).
- [4] T. Imai, C.P. Slichter, K. Yoshimura, and K. Kosuge, *Phys. Rev. Lett.* **70**, 1002 (1993).
- [5] K. Yoshimura, T. Imai, T. Shimuzu, Y. Ueda, K. Kosuge, and H. Yosuka, *J. Phys. Soc. Japan* **58**, 3057 (1989).
- [6] P.C. Hammel, A.P. Reyes, S-W. Cheong, Z. Fisk, and J.E. Schirber, *Phys. Rev. Lett.* **71**, 440 (1993).
- [7] S. Pliberšek and P.F. Meier, submitted.
- [8] E. Niedermeyer, Sleep and EEG, in E. Niedermeyer and F. Lopes Da Silva, *Electroencephalography*, 174 (1993).
- [9] P. Achermann, R. Hartmann, A. Gunzinger, W. Guggenbühl and A.A. Borbély, *European Journal of Neuroscience* **6**, 497 (1994).
- [10] A. Provenzale, L.A. Smith, R. Vio, and G. Murante, *Physica D* **58**, 31 (1992).
- [11] J. Fell, J.Röschke and C. Schäffner, *Biological Cybernetics* **75**, 85 (1996).
- [12] C.-K. Peng, S. Buldyrev, S. Havlin, M. Simons, H.E. Stanley and A.L. Goldberger, *Phys. Rev. E* **49**, 1691 (1994).
- [13] R. Badii and P. Talkner, *Europhys. Lett.* **43**, 284 (1998).

15 Mechanical Workshop

B. Schmid, K. Bösiger, P. Treier, A. Streuli, B. Wachter,
B. Zaugg, A. Rochat (apprentice), and Y. Steiger (apprentice)

The activities of the mechanical workshop are three-fold³:

- Fabrication of specialized equipment, which can not be purchased commercially, for the various research projects of the institute. Some major components are listed below.
- Training of apprentices, and first year students in experimental physics in short special workshop courses.
- Services for other institutes or firms.

In the following we list some examples of components produced during 1999 with reference to the sections in this annual report:

Measurement of the gravitational constant: the suspension system has been completely reconstructed (see Sec.1 and Figures 15.1 and 15.2).

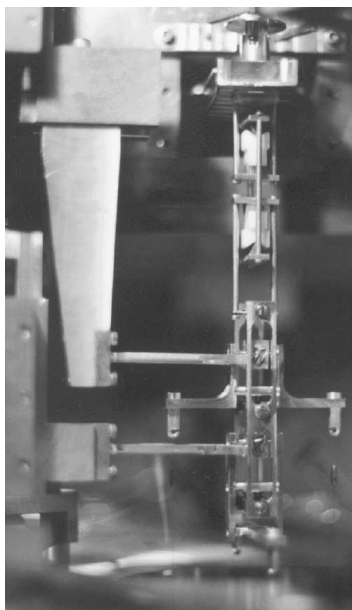


Figure 15.1: *Part of the setup of the measurement of the gravitational constant (Sec.1). The two horizontal bars in the lower half of the picture act as cantilevers. They can be moved up and down to exchange the test masses.*

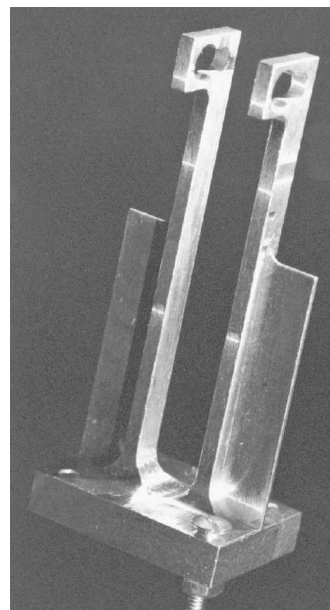


Figure 15.2: *Close-up of a cantilever (total length 58 mm) made of a single piece of aluminum.*

Surface physics: manufacture of ultrahigh vacuum components, such as sample manipulators with five degrees of freedom, major components for the COPHEE spectrometer (Sec. 12.9), such as support frame, mu-metal shieldings, gas system for sample preparation,

³See <http://www.physik.unizh.ch/groups/werkstatt> for additional information.

and high-precision sample holders made of various materials (see Sec. 12).

HERA-B: fabrication of support structures for the MSGC detectors made of various materials (CFK, GFK, Hexel, aluminum) allowing for precise and easy adjustments of the detector positions (see Sec. 8).

H1: preparations for the construction of a set of five concentric proportional chambers like e.g. four high-precision steel cylinders (300 to 400 mm diameter and 2700 mm length) serving as mandrels, special milling tools for the cutting of grooves into the Rohacell layer for the cathode readout cables, ovens for the heat-treatment of surfaces and glued components, high-precision gauges, modifications to wire transfer frames and tooling, construction of a prototype chamber, and start of construction of final chambers (see Sec. 7 for further details).

Athena: fabrication of the support structure for the silicon microstrip modules and the CsI crystals of the annihilation detector which is operated at very low temperature, and is machined from a single block of aluminum (see fig. 6.4 and Sec. 6).

16 Electronics

K. Esslinger and P. Soland

In the report period 1999/2000 we were mostly occupied with the following projects:

H1: for the upgrade of the large multiwire proportional chamber we produced blueprints for the HV- and READ-OUT prints and contacted a manufacturer. We experienced serious difficulties due to the unusually small distances between the signal lines (80-100 μm) of the twenty different printed circuit foils (see Sec. 7).

HERA-B: in summer 1999, we further developed and built a 6-channel offset amplifier as an additional option for the current monitoring system used in the tests of micro-strip-gas-chambers (MSGC's) at PSI Villigen (see Sec. 8).

ATHENA: a multifold analog buffer amplifier system with 36 channels is being constructed. Each channel accepts differential input signals from the silicon detector modules for an energy and topology determination. The buffer amplifiers have a fixed gain and deliver output signals to the ADC's through 50 Ω Lemo cables. The 36 channels will be housed in a special case situated close to the vacuum feedthroughs (see Sec. 6).

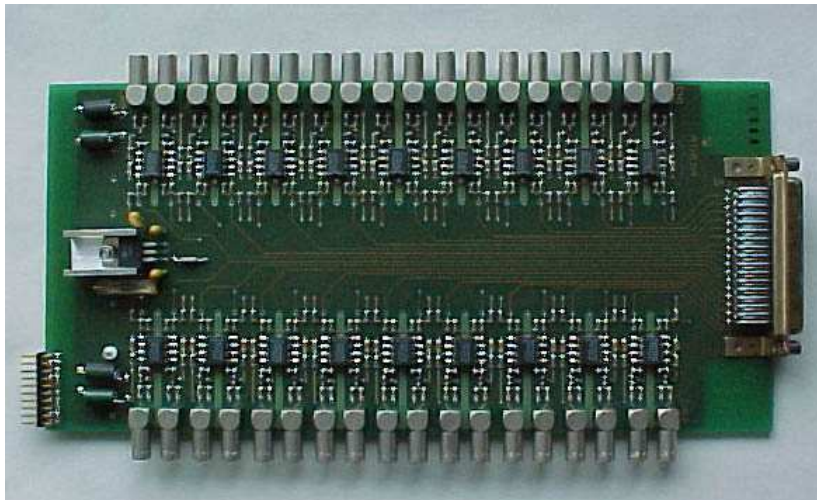


Figure 16.1: 36 - channel buffer amplifier for the ATHENA project

17 Publications

17.1 Research group of Prof. C. Amsler

Articles

- Observation of resonances in the reaction $\bar{p}p \rightarrow \pi^0\eta\eta$ at 1.94 GeV/c
A. Abele et al. (Crystal Barrel Collaboration)
Eur. Phys. Journal C8 (1999) 67
- $\bar{p}d$ -annihilation at rest into $\pi^+\pi^-\pi^-p_{spectator}$
A. Abele et al. (Crystal Barrel Collaboration)
Phys. Lett. B 450 (1999) 275
- Antiproton-proton annihilation at rest into $K^+K^-\pi^0$
A. Abele et al. (Crystal Barrel Collaboration)
Phys. Lett. B 468 (1999) 178
- The ρ -mass, width and line shape in $\bar{p}p$ annihilation at rest into $\pi^+\pi^-\pi^0$
A. Abele et al. (Crystal Barrel Collaboration)
Phys. Lett. B 469 (1999) 270
- Observation of Pontecorvo reactions with open strangeness: $\bar{p}d \rightarrow \Lambda K^0$ and $\bar{p}d \rightarrow \Sigma^0 K^0$
A. Abele et al. (Crystal Barrel Collaboration)
Phys. Lett. B 469 (1999) 276
- Scalar mesons in the 1500 MeV mass region
C. Amsler
Proc. Workshop on Hadron Spectroscopy, Frascati Physics Series, Vol. XV (1999) 609
- Recent results from Crystal Barrel in $\bar{p}p \rightarrow K\bar{K}\pi$ and $\omega 4\pi$
P. Giarritta
Proc. LEAP 98 Conf., Villasimius, Nucl. Phys. A 655 (1999) 71c
- Strangeness production in Pontecorvo reactions on deuterium
C. Regenfus
Proc. LEAP 98 Conf., Villasimius, Nucl. Phys. A 655 (1999) 263c
- Antihydrogen production and precision experiments on trapped cold antihydrogen
C. Regenfus
Proc. Workshop on Exotic atoms, molecules and muon catalyzed fusion, Ascona, Hyperfine Interactions 119 (1999) 301
- Lorentz-angle measurement in irradiated silicon
R. Kaufmann and B. Henrich
Proc. of the ENDEASD Workshop (C. Claeys, Ed.), Santorin (1999) 167

Articles in press

- Test of $\bar{N}N$ potential models: isospin relations in $\bar{p}d$ annihilations at rest and the search for quasinuclear bound states
A. Abele et al. (Crystal Barrel Collaboration)
Eur. Phys. Journal C
- $\bar{p}p$ -annihilation into ωX ($X = \pi^0, \eta, \eta'$) at 600, 1200 and 1940 MeV/c
A. Abele et al. (Crystal Barrel Collaboration)
Eur. Phys. Journal C

- Study of f_0 Decays into four Neutral Pions
A. Abele et al. (Crystal Barrel Collaboration)
Eur. Phys. Journal C
- Branching ratios for $\bar{p}p$ annihilation at rest into two-body final states
A. Abele et al. (Crystal Barrel Collaboration)
Nucl. Phys. A
- Search for New Mesons in Proton-Antiproton Annihilation into $\omega\pi^0\pi^0$ and $\omega\eta\pi^0$
P. Giarritta
Dissertation, Universität Zürich (2000)
- Hadron Spectroscopy
C. Amsler
Proc. XVth Particles and Nuclei Int. Conf., Uppsala (1999)
- Proton-antiproton annihilation into 6γ and 7γ
C. Amsler
Proc. 8th Int. Conf. on Hadron Spectroscopy, Beijing (1999), Nucl. Phys. A
- Lorentz-angle in irradiated silicon
R. Kaufmann and B. Henrich
Nucl. Instr. and Methods in Phys. Research A
- Pontecorvo reactions with strangeness production on deuterium
C. Regenfus
Proc. XVth Particles and Nuclei Int. Conf., Uppsala (1999)
- Study of the Performance of ATLAS Prototype Detectors using Analog LHC Frontend Electronics
P. Riedler
Proc. 5th Int. Conf. on Position-Sensitive Detectors, London (1999), Nucl. Instr. and Methods in Phys. Research A

Conference reports

- Study of scalar mesons in $\bar{p}p$ annihilation into $\eta\eta\pi$ at 900 MeV/c
M. Heinzlmann
Annual Meeting of the Swiss Physical Society, Montreux (2000)

Invited lectures

- C. Amsler
Plenary talk, XVth Particles and Nuclei Int. Conf., Uppsala, 12.6.99
“Hadron Spectroscopy”
- C. Amsler
Invited talk, 8th Int. Conf. on Hadron Spectroscopy, Beijing, 23.8.99
“Proton-antiproton annihilation at rest into $\omega\pi^0\pi^0$ and $\omega\eta\pi^0$ ”
- C. Amsler
Invited talk, 8th Int. Conf. on Hadron Spectroscopy, Beijing, 23.8.99
“Proton-antiproton annihilation into three neutral pseudoscalars at 900 MeV/c”
- R. Kaufmann
Invited talk, European network on defect engineering of advanced semiconductor devices (ENDEASD), Santorin, 25.4.99
“Lorentz-angle measurement in irradiated silicon”

- C. Regenfus
Invited talk, XVth Particles and Nuclei Int. Conf., Uppsala, 15.6.99
“Pontecorvo reactions with strangeness production on deuterium”
- P. Riedler
Invited talk, 5th Int. Conf. on Position-Sensitive Detectors, University College, London, 13.9.99
“Study of the Performance of ATLAS Prototype Detectors using Analog LHC Frontend Electronics”
- P. Riedler
Seminarvortrag, Inst. f. Hochenergiephysik, Österr. Akademie der Wissenschaften, 23.3.00
“Development and Status of the ATHENA detector”

17.2 Research group of Prof. R. Engfer

Articles

- Suche nach der Myon-Elektron-Konversion in Gold
F. Riepenhausen
PhD thesis, Zürich University, 1999.
- Results of the SINDRUM II experiment
P. Wintz
Proc. Lepton-Baryon 98, ed. H.V. Klapdor-Kleingrothaus and I.V. Krivosheina, Institute of Physics Publ., Bristol (1999) 534-546.
- The future of $\mu \rightarrow e\gamma$ at PSI
A. van der Schaaf
Proc. Lepton-Baryon 98, ed. H.V. Klapdor-Kleingrothaus and I.V. Krivosheina, Institute of Physics Publ., Bristol (1999) 547-566.

Conference reports

- Results from SINDRUM II
P. Wintz
Proc. 29th International Conference on High Energy Physics, ed. A. Astbury, D. Axen, J. Robinson, World Scientific, Singapore (1999) Part 2, 1.

Invited lectures

- A. van der Schaaf
seminar at DESY, February 2000
”Lepton Flavor violation”
- P. Wintz
seminar at Jülich, January 2000
”Status of SINDRUM II”

17.3 Research group of Prof. H. Keller

Articles

- Flux-line lattice structure in untwinned $\text{YBa}_2\text{Cu}_3\text{O}_{7-x}$
S.T. Johnson, E.M. Forgan, S.H. Lloyd, C.M. Aegerter, S.L. Lee, R. Cubitt, P.G. Kealey,

- C. Ager, S. Tajima, A. Rykov, and D. McK. Paul
Phys. Rev. Lett. **82**, 2792-2795 (1999)
- Fluxoids and neutron polarisation effects
E.M. Forgan, P.G. Kealey, T.M. Riseman, S.L. Lee, D.McK. Paul, C.M. Aegerter, R. Cubitt, P. Schleger, S.T. Johnson, A. Pautrat, and Ch. Simon
Physica B **268**, 115-121 (1999)
 - Temperature dependence of muon spin relaxation in $\text{Pr}_{1/2}\text{Sr}_{1/2}\text{MnO}_3$
R.I. Grynspan, I.M. Savić, S. Romer, X. Wan, J. Fenichel, C.M. Aegerter, H. Keller, D.R. Noakes, C.E. Stronach, A. Maignan, C. Martin, and B. Raveau
Physica B **259-261**, 824-825 (1999)
 - Stability of the vortex lattice in ET superconductors studied by μSR
S.J. Blundell, S.L. Lee, F.L. Pratt, C.M. Aegerter, Th. Jestädt, B.W. Lovett, C. Ager, T. Sasaki, V.N. Laukhin, E.M. Forgan, and W. Hayes
Synth. Met. **103 (1-3)**, 1925-1928 (1999)
 - Specific heat of $\text{YBa}_2\text{Cu}_3\text{O}_{7-\delta}$ and $(\text{La}_{2-x}\text{Sr}_x)\text{CuO}_4$: Evidence for d-wave pairing
N.E. Phillips, B. Buffetau, R. Calemczuk, K.W. Dennis, J.P. Emerson, R.A. Fisher, J.E. Gordon, T.E. Hargreaves, C. Marcenat, R.W. McCallum, A.S. O'Connor, A. Schilling, B.F. Woodfield, and D.A. Wright
J. Superconductivity **12 (1)**, 105-111 (1999)
 - Specific heat of $\text{YBa}_2\text{Cu}_3\text{O}_{7-\delta}$ and $(\text{La}_{2-x}\text{Sr}_x)\text{CuO}_4$: Evidence for d-Wave Pairing
N.E. Phillips, R.A. Fisher, A. Schilling, B. Buffetau, T.E. Hargreaves, C. Marcenat, R. Calemczuk, A.S. O'Connor, and R.W. McCallum
Physica B **259-261**, 546-547 (1999)
 - Calorimetric study of the transitions between the different vortex states in $\text{YBa}_2\text{Cu}_3\text{O}_7$
F. Bouquet, C. Marcenat, R. Calemczuk, A. Erb, A. Junod, M. Roulin, U. Welp, W.K. Kwok, G.W. Crabtree, N.E. Phillips, R.A. Fisher, and A. Schilling
in: *Physics and Materials Science of Vortex States, Flux Pinning and Dynamics*, eds. R. Kossowsky *et al.*, NATO Science Series E, Vol. **356**, 1999 (Kluwer Academic) (p. 743)
 - Experimental evidence for fast cluster formation of chain oxygen vacancies in $\text{YBa}_2\text{Cu}_3\text{O}_{7-\delta}$ being at the origin of the fishtail anomaly
A. Erb, A.A. Manuel, M. Dhalle, F. Marti, J.-Y. Genoud, B. Revaz, A. Junod, D. Vasumathi, Sh. Ishibashi, A. Shukla, E. Walker, Ø. Fischer, R. Flükiger, R. Pozzi, M. Mali, and D. Brinkmann
Solid State Commun. **112**, 245-249 (1999)
 - Spin and charge dynamics in the Cu-O chains of $\text{YBa}_2\text{Cu}_4\text{O}_8$
F. Raffa, M. Mali, A. Suter, A. Yu. Zavidonov, J. Roos, D. Brinkmann, and K. Conder
Phys. Rev. B **60**, 3636-3642 (1999)
 - Spin dynamics in the paramagnetic phase of $\text{YBa}_2\text{Cu}_3\text{O}_{6.12}$ as seen by Cu NMR
R. Pozzi, M. Mali, D. Brinkmann, and A. Erb
Phys. Rev. B **60**, 9650-9661 (1999)
 - Angular-dependent torque magnetometry on single-crystal $\text{HgBa}_2\text{CuO}_{4+y}$ near the critical temperature

- J. Hofer, T. Schneider, J.M. Singer, M. Willemin, H. Keller, C. Rossel, and J. Karpinski
Phys. Rev. B **60**, 1332-1339 (1999)
- High-pressure synthesis, crystal growth, phase diagrams, structural and magnetic properties of $\text{Y}_2\text{Ba}_4\text{Cu}_{6+n}\text{O}_{14+n}$, $\text{HgBa}_2\text{Ca}_{n-1}\text{Cu}_n\text{O}_{2n+2+\delta}$ and quasi-one-dimensional cuprates
J. Karpinski, G.I. Meijer, H. Schwer, R. Molinski, E. Kopnin, K. Conder, M. Angst, J. Jun, S. Kazakov, A. Wisniewski, R. Puzniak, J. Hofer, V. Alyoshin, and A. Sin
Supercond. Sci. Technol. **12**, R153-R181 (1999)
 - High pressure crystal growth and physical properties of Hg-based superconductors and infinite-chain $\text{A}_{1-x}\text{CuO}_2$ compounds
J. Karpinski, H. Schwer, R. Molinski, G.I. Meijer, E. Kopnin, M. Angst, J. Hofer, R. Puzniak, and A. Wisniewski
in: *Ceramics: Getting into the 2000's, Part A, Advances in Science and Technology*, Vol. **13**, ed. P. Vincenzini (Techna srl Publ., Faenza 1999)
 - Electron spin resonance and magnetic susceptibility suggest superconductivity in Na doped WO_3 samples
A. Shengelaya, S. Reich, Y. Tsabba, and K.A. Müller
Eur. Phys. J. B **12**, 13-15 (1999)
 - Giant oxygen isotope effect on the spin glass transition in $\text{La}_{2-x}\text{Sr}_x\text{Cu}_{1-z}\text{Mn}_z\text{O}_4$ as revealed by muon spin rotation
A. Shengelaya, Guo-meng Zhao, C.M. Aegerter, K. Conder, I.M. Savić, and H. Keller
Phys. Rev. Lett. **83**, 5142-5145 (1999)
 - Oxygen isotope effects in manganites: Evidence for (bi)polaronic charge carriers
G. M. Zhao, H. Keller, R. L. Greene, and K. A. Müller
in: *Physics of Manganites*, ed. T. A. Kaplan and S. D. Mahanti (Kluwer Academic/Plenum publisher, 1999) pp. 221-241
 - Isotope and pressure effects in manganites: Important experimental constraints on the physics of manganites
G. M. Zhao, K. Conder, H. Keller, and K. A. Müller
Phys. Rev. B **60**, 11914-11917 (1999)
 - Oxygen isotope shift of the charge-stripe ordering temperature in $\text{La}_{2-x}\text{Sr}_x\text{CuO}_4$ from x-ray absorption spectroscopy
A. Lanzara, G. M. Zhao, N. L. Saini, A. Bianconi, K. Conder, H. Keller, and K. A. Müller
J. Phys.: Condens. Matter **11**, L541-L546 (1999)
 - Magnetic field induced dimensional crossover phenomena in cuprate superconductors and their implications
T. Schneider and J.M. Singer
Physica C **313**, 188-196 (1999)
 - Fundamental constraints for the mechanism of superconductivity in cuprates
T. Schneider and J.M. Singer
Eur. Phys. J. B **7**, 517-518 (1999)
 - Magnetic field induced phase transitions in $\text{YBa}_2\text{Cu}_4\text{O}_8$
T. Schneider and J.M. Singer
Eur. Phys. J. B **8**, 331-334 (1999)

- Qunatum Monte Carlo Simulations of the Twodimensional Attractive Hubbard Model: Phase Diagram and Spectral Properties
J.M. Singer, T. Schneider, and P.F. Meier
in: *Symmetry and Pairing in Superconductors*, eds. M. Ausloos and S. Kruchinin (Kluwer Academic Publisher, 1999) (pp. 41-70)
- Anisotropy of the magnetization discontinuity at the vortex-lattice melting in untwinned $\text{YBa}_2\text{Cu}_3\text{O}_{7-\delta}$
A. Schilling, M. Willemin, C. Rossel, H. Keller, R.A. Fisher, N.E. Phillips, U. Welp, W.K. Kwok, R.J. Olsson, and G.W. Crabtree
Phys. Rev. B **61**, 3592-3603 (2000)
- Influence of neutron-irradiation-induced defects on the flux pinning in $\text{HgBa}_2\text{Ca}_2\text{Cu}_3\text{O}_{8+x}$ single crystals
A. Wisniewski, R. Puzniak, J. Karpinski, J. Hofer, R. Szymczak, M. Baran, F.M. Sauerzopf, R. Molinski, E.M. Kopnin, and J.R. Thompson
Phys. Rev. B **61**, 791-798 (2000)
- Evidence for line nodes in the energy gap for $(\text{La}_{2-x}\text{Sr}_x)\text{CuO}_4$ from low-temperature specific-heat measurements
R.A. Fisher, B. Buffetau, R. Calemczuk, K.W. Dennis, T.E. Hargreaves, C. Marcenat, R.W. McCallum A.S. O'Connor, N.E. Phillips, and A. Schilling
Phys. Rev. B **61**, 1473-1476 (2000)
- Specific heat of Zn-doped $\text{YBa}_2\text{Cu}_3\text{O}_{6.95}$: Possible evidence for Kondo screening in the superconducting state
D.L. Sisson, S.G. Doettinger, A. Kapitulnik, R. Liang, D.A. Bonn, and W.N. Hardy
Phys. Rev. B **61**, 3604-3609 (2000)
- Electron spin resonance with $g_{eff} \simeq 4.2$ in $\text{YBa}_2\text{Cu}_3\text{O}_{6.35}$. The model of copper-oxygen chain fragments
M.V. Eremin, R.M. Eremina, M.R. Gafurov, V.A. Ivanshin, I.N. Kurkin, S.P. Kurzin, H. Keller, and M. Gutmann
JETP **90(2)**, 363-369 (2000)
- EPR in $\text{La}_{1-x}\text{Ca}_x\text{MnO}_3$: Relaxation and bottleneck
A. Shengelaya, Guo-meng Zhao, H. Keller, K.A. Müller, and B.I. Kochelaev
Phys. Rev. B **61**, 5888-5890 (2000)
- Separation of quadrupolar and magnetic contributions to spin-lattice relaxation in the case of a single isotope
A. Suter, M. Mali, J. Roos, and D. Brinkmann
J. Magn. Reson. **143**, 266-273 (2000)

Articles in press

- EPR of $\text{YBa}_2\text{Cu}_3\text{O}_{6.35}$: Models of paramagnetic centres with $g_{eff} \simeq 4.2$
R. Eremina, M. Eremin, M. Gafurov, V. Ivanshin, I. Kurkin, S. Kurzin, H. Keller, and M. Gutmann
Physica B

- High pressure crystal growth and properties of Hg-based superconductors and one-dimensional $A_{1-x}CuO_2$ (A=Sr,Ca,Ba) cuprates
J. Karpinski, G.I. Meijer, H. Schwer, R. Molinski, E. Kopnin, M. Angst, A. Wisniewski, R. Puzniak, J. Hofer, and C. Rossel
in: *Proceedings of the 2nd Polish-US Conference "Recent Developments in High Temperature Superconductivity"*, Karpacz, Poland, 1998; *Lecture Notes in Physics*, ed. J. Klamut *et al.* (Springer Verlag)
- Influence of irradiation-induced defects and chemical substitutions on the flux pinning in Hg-based single crystals and films
A. Wisniewski, R. Puzniak, J.R. Thompson, J. Karpinski, M. Angst, H. Schwer, J. Hofer, S. Kazakov, and R. Szymczak
in: *Studies of High Temperature Superconductors*, ed. A. Narlikar, Volume **31** (Nova Science Publisher, New York, 2000)
- Oxygen isotope effect on the in-plane penetration depth in underdoped $La_{2-x}Sr_xCuO_4$ single crystals
J. Hofer, K. Conder, T. Sasagawa, Guo-meng Zhao, M. Willemin, H. Keller, and K. Kishio
Phys. Rev. Lett. (2000) (cond-mat/9912493)
- T. Schneider and J.M. Singer
Phase Transition Approach to High Temperature Superconductivity (Imperial College Press, London, 2000)

Diploma and PhD theses

- Ultrasensitive torque magnetometry on high- T_c superconductors
Michel Willemin
Dissertation, Physik-Institut, Universität Zürich, 1999

Conference reports

- A possible rotation of the magnetization vector at the melting transition probed by torque magnetometry
A. Schilling, M. Willemin, C. Rossel, H. Keller, R.A. Fisher, N.E. Phillips, U. Welp, W.K. Kwok, R.J. Olsson, and G.W. Crabtree
1999 March Meeting of The American Physical Society, Atlanta, GA, USA, 23 March 1999
- Torque magnetometry on single-crystal high- T_c compounds near the critical temperature: a critical fluctuations approach
J. Hofer, T. Schneider, J.M. Singer, M. Willemin, H. Keller, C. Rossel, J. Karpinski, and T. Sasagawa
Swiss Workshop on Superconductivity and Materials with Novel Electronic Properties, Les Diablerets, Switzerland, 27-29 September, 1999
- Methods for the precise determination of the effective mass anisotropy ratio in high- T_c superconductors
C. Rossel, M. Willemin, J. Hofer, and H. Keller
Swiss Workshop on Superconductivity and Materials with Novel Electronic Properties, Les Diablerets, Switzerland, 27-29 September, 1999

- Charge degree of freedom and single-spin fluid model in $\text{YBa}_2\text{Cu}_4\text{O}_8$
A. Suter, M. Mali, J. Roos, and D. Brinkmann
Swiss Workshop on Superconductivity and Materials with Novel Electronic Properties, Les Diablerets, Switzerland, 27-29 September, 1999
- Direct evidence for two type charge carriers in $\text{La}_{2-x}\text{Sr}_x\text{CuO}_4$: An Electron Paramagnetic Resonance Study
A. Shengelaya
Swiss Workshop on Superconductivity and Materials with Novel Electronic Properties, Les Diablerets, Switzerland, 27-29 September, 1999
- Low-energy charge fluctuations in the presence of the pseudo spin gap in $\text{YBa}_2\text{Cu}_4\text{O}_8$
A. Suter, M. Mali, J. Roos, and D. Brinkmann
6th International Conference on Material and Mechanisms of Superconductivity and High Temperature Superconductors, Houston, USA, 20-25 February, 2000
- Chain charge fluctuations in $\text{YBa}_2\text{Cu}_4\text{O}_8$ detected via apex oxygen nuclear quadrupolar relaxation
M. Mali, A. Suter, J. Roos, D. Brinkmann, H. Keller, and J. Karpinski
6th International Conference on Material and Mechanisms of Superconductivity and High Temperature Superconductors, Houston, USA, 20-25 February, 2000
- Oxygen isotope effect on underdoped $\text{La}_{2-x}\text{Sr}_x\text{CuO}_4$ microcrystals measured by torque magnetometry
J. Hofer, Guo-meng Zhao, M. Willemin, H. Keller, K. Conder, T. Sasagawa, and K. Kishio
6th International Conference, Materials and Mechanisms of Superconductivity and High Temperature Superconductors, Houston, USA, 20-25 February, 2000
- Torque magnetometry on single-crystal high temperature superconductors near the critical temperature: a scaling approach
J. Hofer, T. Schneider, J.M. Singer, M. Willemin, H. Keller, T. Sasagawa, K. Kishio, K. Conder, and J. Karpinski
6th International Conference, Materials and Mechanisms of Superconductivity and High Temperature Superconductors, Houston, USA, 20-25 February, 2000
- Giant oxygen isotope effect on the spin glass transition in $\text{La}_{2-x}\text{Sr}_x\text{Cu}_{1-z}\text{Mn}_z\text{O}_4$ as revealed by muon spin rotation
A. Shengelaya, Guo-meng Zhao, C.M. Aegerter, K. Conder, I.M. Savic, and H. Keller
18th General Conference of the Condensed Matter Division of the European Physical Society, Montreux, Switzerland, 13-17 March, 2000
- Angular dependent magnetization discontinuity at the vortex-lattice melting: a comparison with high-resolution calorimetric data
A. Schilling, M. Willemin, C. Rossel, H. Keller, R.A. Fisher, N.E. Phillips, U. Welp, W.K. Kwok, R.J. Olsson, G.W. Crabtree, and K. Kadowaki
18th General Conference of the Condensed Matter Division of the European Physical Society, Montreux, Switzerland, 13-17 March, 2000
- Vortex studies in heavy-ion irradiated $\text{Bi}_{2.15}\text{Sr}_{1.85}\text{CaCu}_2\text{O}_{8+\delta}$ probed by μSR and small-angle neutron scattering

F.Y. Ogrin, S.L. Lee, C. Ager, H. Keller, I.M. Savic, E.M. Forgan, S.H. Loyd, T. Rise-
man, R. Cubitt, and G. Wirth
18th General Conference of the Condensed Matter Division of the European Physical
Society, Montreux, Switzerland, 13-17 March, 2000

- Electrical transport in the ferromagnetic state of manganites: small-polaron metallic
conduction at low temperatures
Guo-meng Zhao, W. Prellier, and H. Keller
18th General Conference of the Condensed Matter Division of the European Physical
Society, Montreux, Switzerland, 13-17 March, 2000
- Charge fluctuations in the normal state of $\text{YBa}_2\text{Cu}_4\text{O}_8$ observed by ^{17}O NMR
M. Mali, J. Roos, A. Suter, D. Brinkmann, H. Keller, and J. Karpinski
18th General Conference of the Condensed Matter Division of the European Physical
Society, Montreux, Switzerland, 13-17 March, 2000
- Oxygen isotope effect on underdoped $\text{La}_{2-x}\text{Sr}_x\text{CuO}_4$ microcrystals
J. Hofer, Guo-meng Zhao, M. Willemin, H. Keller, K. Conder, T. Sasagawa, and
K. Kishio
18th General Conference of the Condensed Matter Division of the European Physical
Society, Montreux, Switzerland, 13-17 March, 2000

Invited lectures

- A. Schilling
Superconducting ceramics: materials of atoms, matter of vortices
ETH Zürich, Switzerland, 30 April 1999
- H. Keller
Vortexmaterie und Myonen in Supraleitern
University of Zurich, Switzerland, 6 May, 1999
- A. Shengelaya
Oxygen isotope effects in the manganates and cuprates studied by electron paramag-
netic resonance
Specialized Colloque Ampere, Pisa, Italy, 14-18 June, 1999
- A. Schilling
The magnetization discontinuity at the vortex-lattice melting in $\text{YBa}_2\text{Cu}_3\text{O}_7$ for an
extreme off-c-axis geometry and in low magnetic fields
International Workshop on Vortex Dynamics in High-Temperature Superconductors,
Stanford, CA, USA, 21 June, 1999
- M. Willemin
Hochempfindliche Drehmoment-Magnetometrie an Hochtemperatur-Supraleitern
CSEM, Zurich, 14. July, 1999
- M. Willemin
Separation of the irreversibility line from the melting line in $\text{YBa}_2\text{Cu}_4\text{O}_7$ by an oscillat-
ing magnetic field
Swiss Workshop on Superconductivity and Materials with Novel Electronic Properties,
Les Diablerets, Switzerland, 27-29 September, 1999

- A. Schilling
Superconducting ceramics: materials of atoms, matter of vortices
Johann Wolfgang Goethe-Universität Frankfurt am Main, Germany, 16 August, 1999
- A. Shengelaya
Giant oxygen isotope effect on the spin glass transition in $\text{La}_{2-x}\text{Sr}_x\text{Cu}_{1-z}\text{Mn}_z\text{O}_4$ as revealed by muon spin rotation
8th International Conference on Muon Spin Rotation, Relaxation and Resonance, Les Diablerets, Switzerland, August 30 - September 3, 1999
- H. Keller
Magnetische Flusslinien in Hochtemperatur-Supraleitern
Physikalische Gesellschaft Zürich, Zurich, Switzerland, 4 November, 1999
- Guo-meng Zhao
Experimental constraints on the physics of the cuprate superconductors
Symposium on polarons and their condensation, University of Zurich, 10-11 November, 1999
- J. Hofer
Studies of intrinsic magnetic properties of high temperature superconductors by means of torque magnetometry
University of Zurich, Switzerland, 30 March, 2000

17.4 Research group of Prof. P. F. Meier

Articles

- Electroencephalograms in epilepsy: analysis and seizure prediction within the framework of Lyapunov theory
H. R. Moser, B. Weber, H. G. Wieser and P. F. Meier
Physica D **130**, 291-305 (1999)
- Cluster calculations of the hyperfine properties of copper compounds
H. U. Suter, P. Hüsler, E. P. Stoll, S. Schafroth, and P. F. Meier
Hyperfine Interactions, **120**, 137-140 (1999)
- Pre-ictal changes and EEG analyses within the framework of Lyapunov theory
H. R. Moser, P. F. Meier, H. G. Wieser and B. Weber
in Proceedings of the Workshop "Chaos in Brain?", p. 96-111, World Scientific Singapore, (1999)
- The structure of a Lyapunov spectrum can be determined locally
H. R. Moser and P. F. Meier
Physics Letters A **263**, 167-174 (1999)
- Cluster calculations of the hyperfine interactions in superconducting copper compounds
P. F. Meier, T. A. Claxton, P. Hüsler, S. Pliberšek, and E. P. Stoll
Z. Naturf., **55 a**, 247-255 (2000)
- First-principles calculations of hyperfine interactions in La_2CuO_4
P. Hüsler, H. U. Suter, E. P. Stoll, and P.F. Meier
Phys. Rev. B **61**, 1567-1579 (2000)

Articles in press

- Interpretation of nuclear quadrupole resonance spectra in doped La_2CuO_4
S. Pliberšek and P. F. Meier
Europhysics Letters
- Quasiparticle diffusion in tantalum using superconducting tunnel junctions
T. Nussbaumer, P. Lerch, E. Kirk, A. Zehnder, R. Füchslin, P. F. Meier, and H. R. Ott
Phys. Rev. B

Invited lectures

- P. F. Meier
“Pre-ictal Changes and EEG Analyses within the framework of Lyapunov Theory”
Invited talk, Interdisciplinary workshop on “Chaos in Brain?”, Bonn, 11. 3. 99
- P. F. Meier
“Examples of Collaborations between Computational Physics, Computer Science, and Medicine”
Übersichtsvortrag, Tagung der Schweiz. Phys. Gesellschaft, Bern, 25. 2. 99
- P. F. Meier
“Cluster Calculations of the Electronic Structure of High-Temperature Superconducting Materials”
Invited talk, XVth Internat. Symposium on Nuclear Quadrupole Interactions, Leipzig, 29. 7. 99
- P. F. Meier
“Cluster Calculations of the Electronic Structure of High-Temperature Superconducting Materials”
Invited talk, Symposium on Polarons and their Interaction, Zürich, 11. 11. 99
- P. F. Meier
“Ab initio Approach to the Electronic Structure of High-Temperature Superconducting Materials”
Seminar talk, Univ. of Notre Dame, South Bend (IN), 7. 12. 99

17.5 Research group of Prof. J. Osterwalder**Articles**

- Controlled underdoping of cuprates using ultraviolet radiation
P. Schwaller, S. Berner, T. Greber, J. Osterwalder
Appl. Phys. Lett. 74 (1999) 1877-1879
- Correlation effects in the low-energy region of nickel photoemission spectra
F. Manghi, V. Bellini, J. Osterwalder, T. J. Kreuz, P. Aebi, C. Arcangeli
Phys. Rev. B 59 (Rapid Communication) (1999) R10409-R10412
- XPD and STM investigation of hexagonal boron nitride on Ni(111)
W. Auwärter, T. J. Kreuz, T. Greber, J. Osterwalder
Surf. Sci. 429 (1999) 229-236

- Interaction of gas-phase oriented N_2O with lithium metal: evidence for an Eley-Rideal mechanism
M. Brandt, F. Kuhlmann, T. Greber, N. Böwering, U. Heinzmann
Surf. Sci. 439 (1999) 49-58
- Production and characterization of Ti:sapphire thin films grown by reactive laser ablation with elemental precursors
P. R. Willmott, P. Manoravi, J. R. Huber, T. Greber, T. A. Murray, K. Holliday
Optics Lett. 24 (1999) 1581-1583
- Deposition of Ti:sapphire thin films by reactive pulsed laser ablation using liquid metals and oxygen
P. Manoravi, P. R. Willmott, J. R. Huber, T. Greber
Appl. Phys. A [Suppl.] 69 (1999) S865-S867
- X-ray photoelectron diffraction study of an anatase thin film: $TiO_2(001)$
G. S. Herman, Y. Gao, T. T. Tran, J. Osterwalder
Surf. Sci. 447 (2000) 201-211

Articles in press

- Electronic structure of K doped C_{60} monolayers on $Ag(001)$
C. Cepek, M. Sancrotti, T. Greber, J. Osterwalder
Surf. Sci. (2000)
- Angle-resolved photoemission study of clean and hydrogen saturated $Mo(110)$
J. Kröger, T. Greber, J. Osterwalder
Phys. Rev. B (2000)
- Full hemispherical photoelectron diffraction and Fermi surface mapping
J. Osterwalder, T. Greber, E. Wetli, J. Wider, H.-J. Neff
Prog. Surf. Sci. (2000)
- Surface states on clean and adsorbate-covered metal surfaces
J. Osterwalder, T. Greber, J. Kröger, J. Wider, H.-J. Neff, F. Baumberger
M. Hoesch, W. Auwärter, R. Fasel, P. Aebi
Proceedings of the *Workshop on Physics in Low Dimensions*, Oaxaca, Mexico, (Plenum Press, 2000)
- Influence of an atomic grating on a magnetic Fermi surface
T. Greber, W. Auwärter, J. Osterwalder
Proceedings of the *Workshop on Physics in Low Dimensions*, Oaxaca, Mexico, (Plenum Press, 2000)

Diploma and PhD Theses

- Structural analysis of hexagonal boron nitride on nickel (111) and additional cobalt clusters by angle-scanned photoelectron diffraction
Matthias Muntwiler
Diploma Thesis, Physik-Institut, Universität Zürich, 1999

Conference reports

- Fermi-Kanten als Probenthermometer
J. Kröger
Frühjahrstagung der Deutschen Physik. Gesellschaft, Münster, 26.3.99

- Surface structure and crystallinity of CVD grown anatase-TiO₂(001) by x-ray photoelectron diffraction
J. Osterwalder
Environmental Molecular Sciences Symposium on Physics and Chemistry of Oxide Surfaces, Pacific Northwest National Laboratory, Richland, WA, USA, 24.7.99
- Structure-bandstructure relationship for Co layers on Cu(111)
E. Wetli, H.-J. Neff, T. Greber, J. Osterwalder (Poster)
Sixth Int. Conf. on the Structure of Surfaces, Vancouver, Canada, 29.7.99
- Surface sensitivity of medium-energy electron diffraction (MEED)
H.-J. Neff, E. Wetli, H. Schmid, M. Aeschlimann, J. Osterwalder (Poster)
Sixth Int. Conf. on the Structure of Surfaces, Vancouver, Canada, 29.7.99
- Ultraviolet photoelectron diffraction from oriented CO molecules
M. Hoesch
18th European Conference on Surface Science, Vienna, 22.9.99
- Towards near-node photoelectron holography
J. Wider (Poster)
18th European Conference on Surface Science, Vienna, 23.9.99
- Towards near-node photoelectron holography
T. Greber (Poster)
Swiss Light Source Workshop, Brunnen, 29.10.99
- Spin-resolved Fermi surface mapping at SLS
M. Hoesch (Poster, short talk (Poster Prize))
Swiss Light Source Workshop, Brunnen, 29.10.99
- COPHEE, the complete photoemission experiment
M. Hoesch
Joint INFM, the Abdus Salam ICTP School on *Magnetism Investigated with Neutron Scattering and Synchrotron Radiation Techniques*,
Trieste, 8.2.2000

Invited lectures

- T. Greber
Structural characterization of interfaces with x-ray photoelectron diffraction
Topical Conference on Microstructure and Surface Morphology Evolution in Thin Films,
Trieste, 24.3.99
- J. Osterwalder
Valence band photoemission, Fermi surface mapping and applications of photoelectron diffraction
6-hours of Lecture at the *John Fuggle School on Synchrotron Radiation*,
ICTP Trieste, 17.-21.5.99
- J. Osterwalder
Photoelectron diffraction and Fermi surface mapping
8th Symposium on Surface Physics, Trest Castle, Czech Republic, 1.7.99
- T. Greber
Exploring microscopic processes with electrons
Seminar, Van der Waals-Zeeman Institut, University of Amsterdam, 5.7.99

- J. Kröger
Hydrogen and Oxygen on Mo(110): Are data from electron energy loss spectroscopy and angle-resolved photoelectron spectroscopy consistent?
Max-Planck-Institut für Mikrostrukturforschung, Halle, 1.11.99
- J. Kröger
Oberflächenphononen und elektronische Oberflächenzustände auf Mo(110): eine Studie mittels Elektronenenergieverlustspektroskopie und winkelaufgelöster Photoelektronenspektroskopie
II. Physik. Institut der Rheinisch-Westfälischen Techn. Hochschule Aachen, 18.11.99
- J. Kröger
Hydrogen and Oxygen on Mo(110): Giant Kohn anomalies and Fermi surface nesting
Institut für Laser- und Plasmaphysik der Universität Essen, 19.11.99
- J. Kröger
Adsorbatinduzierte Phononanomalie auf Mo(110)
Physik-Institut der Universität Rostock, 23.11.99
- J. Kröger
Adsorbatinduzierte Phononanomalie auf Mo(110)
Institut für Oberflächenphysik und Mikrostrukturphysik,
Techn. Universität Dresden, 24.11.99
- J. Osterwalder
Surface states on clean and adsorbate-covered metal surfaces
Workshop on *The Physics of Low Dimensions*, Oaxaca, Mexico, 17.1.2000
- T. Greber
Magnetic coupling across a single layer tunnelling barrier: Co on *h*-BN/Ni(111)
Workshop on *The Physics of Low Dimensions*, Oaxaca, Mexico, 18.1.2000

17.6 Research group of Prof. U. Straumann (for H1 publications see Sec. 17.7)

Articles

- Search for heavy neutrinos in the β -spectrum of ^{63}Ni
E. Holzschuh, W. Kündig, L. Palermo, H. Stüssi, and P. Wenk
Phys. Lett. B 451, 247 (1999).

Articles in press

- The β -spectrum of ^{35}S and search for the admixture of heavy neutrinos
E. Holzschuh, L. Palermo, H. Stüssi, and P. Wenk
Phys. Lett. B.

Conference reports

- Determination of the gravitational constant
St. Schlamminger, E. Holzschuh, W. Kündig, F. Nolting, and J. Schurr
Proceedings 220th WE-Heraeus-Seminar,
Testing Relativistic Gravity in Space – Gyroscopes, Clocks, and Interferometers
(Springer, Heidelberg)

- Measurement of the Inclusive Deep Inelastic ep Scattering Cross Section at Low Q^2
R. Wallny, H1 Collaboration
To appear in the proceedings of the International Europhysics Conference HEP 99,
Tampere, Finland, July 15 - 21, 1999
- Messung des tief-inelastischen Wirkungsquerschnitts bei kleinen Q^2
R. Wallny, DPG Frühjahrstagung, Heidelberg, Germany, March 15 - 19, 1999

Invited lectures

- St. Schlamminger
Determination of the gravitational constant
Sommer school, Bad Honnef, Aug. 1999
- O. Steinkamp
Running Experience with the Outer Tracker
HERA-B Seminar, DESY, February 3, 1999
- O. Steinkamp
A Honeycomb Tracking Detector for the HERA-B Experiment
Seminar, Universität Heidelberg, February 8, 1999
- O. Steinkamp
HERA-B and LHCb - Two Generations of Hadronic B Factories
Workshop on B Physics at the Tevatron - Run II and Beyond, Fermilab, September
23-25, 1999
- O. Steinkamp
Status and Results From HERA-B
IIIrd Int. Conf. on B Physics and CP Violation, Taipei City/Taiwan, December 3-7,
1999, (to be published in World Scientific)
- O. Steinkamp
HERA-B - Status and Perspectives
NIKHEF Annual Scientific Meeting, Universiteit Utrecht, December 17, 1999
- U. Straumann
Neuere Resultate von H1
seminar Physikalisches Institut der Universität Basel, November 18, 1999
- M. Ziegler, P. Cwetanski, U. Straumann
A triple GEM detector for LHCb
Workshop on Micro-Pattern Gas Detectors, Orsay, France, June 28-30, 1999.
LHCb PUBLIC Note, 99-024, June 30, 1999,
<http://lhcb.cern.ch/notes/postscript/99notes/99-024.ps>

17.7 Research group of Prof. P. Truöl

Articles

- Charged Particle Cross Sections in Photoproduction and Extraction of the Gluon Density in the Photon
H1-Collaboration**, C. Adloff et al.
DESY 98 - 148, hep-ex 9810020
The European Physical Journal **C10** (1999), 363 - 372

- Measurement of D^* Meson Cross Sections at HERA and Determination of the Gluon Density in the Proton
H1-Collaboration**, C. Adloff et al.
DESY 98 – 204, hep-ex 9812023
Nuclear Physics **B545** (1999), 21 - 44
- Measurement of Internal Jet Structure in Di-jet Production in Deep Inelastic Scattering at HERA
H1-Collaboration**, C. Adloff et al.
DESY 98 – 210, hep-ex 9901010
Nuclear Physics **B545** (1999), 3 - 20
- Charmonium Production in Deep Inelastic Scattering at HERA
H1-Collaboration**, C. Adloff et al.
DESY 99 – 026, hep-ex 9903008
The European Physical Journal **C10** (1999), 373 - 393
- A Search for Leptoquark Bosons and Lepton Flavour Violation in e^+p Collisions at HERA
H1-Collaboration**, C. Adloff et al.
DESY 99 – 081, hep-ex 9907002
The European Physical Journal **C11** (1999), 447 - 471
- Measurement of Transverse Energy Flow in Deep-Inelastic Scattering at HERA
H1-Collaboration**, C. Adloff et al.
DESY 99 – 091, hep-ex 9907027
The European Physical Journal **C12** (2000), 595 - 607
- Measurement of Open Beauty Production at HERA
H1-Collaboration**, C. Adloff et al.
DESY 99 – 126, hep-ex 9909029
Physics Letters **B467** (1999), 156 - 164
- Forward π^0 -Meson Production at HERA
H1-Collaboration**, C. Adloff et al.
DESY 99 – 094
Physics Letters **B462** (1999), 440 - 452
- A New Measurement of the Properties of the Rare Decay $K^+ \rightarrow \pi^+ e^+ e^-$
E865-Collaboration†, R. Appel et al.
hep-ex 9907045
Physical Review Letters **83** (1999), 4482 - 4485

Articles in press

- Di-jet Rates in Deep-Inelastic Scattering at HERA
H1-Collaboration**, C. Adloff et al.
DESY 98 – 076
The European Physical Journal **C** (2000), in print
- Measurement of Dijet Cross Sections in Low Q^2 and the Extraction of an Effective Parton Density for the Virtual Photon

- H1-Collaboration**, C. Adloff et al.
DESY 98 – 205, hep-ex 9812024
The European Physical Journal **C** (2000), in print.
- $K^+ \rightarrow \pi^+ \mu^- \mu^+$ in E865 at BNL
E865 Collaboration†, Julia A. Thompson et al.
hep-ex 9904026
Proc. 17th Int. Workshop on Weak Interactions and Neutrinos (WIN 99), Cape Town, South Africa, 24-30 Jan 1999.
 - Elastic Electroproduction of ρ Mesons at HERA
H1-Collaboration**, C. Adloff et al.
DESY 99 – 10, hep-ex 9902019
The European Physical Journal **C** (2000), in print.
 - Measurement of Neutral and Charged Current Cross Sections in Positron-Proton Collisions at Large Momentum Transfer
H1-Collaboration**, C. Adloff et al.
DESY 99 – 107, hep-ex 9908059
The European Physical Journal **C** (2000), in print.
 - A New Measurement of the Rare Decay $K^+ \rightarrow \pi^+ \mu^+ \mu^-$
E865-Collaboration†, H. Ma et al.
hep-ex 9910047
Physical Review Letters **84** (2000), in print.
 - Investigation of Power Corrections Event Shape Variables Measured in Deep-Inelastic Scattering
H1-Collaboration**, C. Adloff et al.
DESY 99 – 193, hep-ex 9912052
The European Physical Journal **C** (2000), in print.
 - The H1 Silicon Vertex Detector
D. Pitzl, O. Behnke, M. Biddulph, K. Bösigler, R. Eichler, W. Erdmann, K. Gabathuler, J. Gassner, W.J. Haynes, R. Horisberger, M. Kausch, M. Lindström, H. Niggli, G. Noyes, P. Pollet, S. Steiner, S. Streuli, K. Szeker, and P. Truöl
hep-ex 0002044
submitted to Nuclear Instruments and Methods (2000).
 - Search for Compositeness, Leptoquarks and Large Extra Dimensions in eq Contact Interactions at HERA
H1-Collaboration**, C. Adloff et al.
DESY 00 – 027, hep-ex 0003002
submitted to Physics Letters **B** (2000).
 - Measurement of Di-jet Cross Sections in Photoproduction and Photon Structure H1-Collaboration**, C. Adloff et al.
DESY 00 – 035, hep-ex 000311
submitted to Physics Letters **B** (2000).
 - An Improved Limit on the Rate of the Decay $K^+ \rightarrow \pi^+ \mu^+ e^-$
E865-Collaboration†, R. Appel et al.

hep-ex 00030000
submitted to Physical Review Letters.

† E865-collaboration:

R. Appel^{8,6}, G.S. Atoyan^{2,8}, B. Bassaleck⁵, D.N. Brown⁶, D.R. Bergman⁸, N. Cheung⁶, S. Dhawan⁸, H. Do⁸, J. Egger³, S. Eilerts⁵, C. Felder^{1,6}, H. Fischer⁵, M. Gach⁶, W.D. Herold³, V.V. Isakov^{2,8}, H. Kaspar³, D. Kraus⁶, D. Lazarus¹, L. Leipuner¹, J. Lowe⁵, J. Lozano⁸, H. Ma¹, W. Majid⁸, W. Menzel⁴, S. Pislak^{7,8}, A.A. Poblaguev^{2,8}, A.L. Proskurjakow², P. Rehak¹, P. Robmann⁷, A. Sher⁶, R. Stotzer⁵, J.A. Thompson⁶, P. Truöl^{7,8}, H. Weyer^{4,3}, M.E. Zeller⁸

³ Paul Scherrer Institut, Villigen

⁷ Physik-Institut der Universität Zürich, Zürich

** H1-collaboration (status of March 2000, the actual author list may differ from paper to paper somewhat):

C. Adloff³³, V. Andreev²⁴, B. Andrieu²⁷, V. Arkadov³⁵, A. Astvatsatourov³⁵, I. Ayyaz²⁸, A. Babaev²³, J. Bähr³⁵, P. Baranov²⁴, E. Barrelet²⁸, W. Bartel¹⁰, U. Bassler²⁸, P. Bate²¹, A. Beglarian³⁴, O. Behnke¹⁰, C. Beier¹⁴, A. Belousov²⁴, T. Benisch¹⁰, Ch. Berger¹, G. Bernardi²⁸, T. Berndt¹⁴, J.C. Bizot²⁶, K. Borras⁷, V. Boudry²⁷, W. Braunschweig¹, V. Brisson²⁶, H.-B. Bröker², D.P. Brown²¹, W. Brückner¹², P. Bruel²⁷, D. Bruncko¹⁶, J. Bürger¹⁰, F.W. Büsler¹¹, A. Bunyatyan^{12,34}, H. Burkhardt¹⁴, A. Burrage¹⁸, G. Buschhorn²⁵, A.J. Campbell¹⁰, J. Cao²⁶, T. Carli²⁵, S. Caron¹, E. Chabert²², D. Clarke⁵, B. Clerboux⁴, C. Collard⁴, J.G. Contreras^{7,41}, J.A. Coughlan⁵, M.-C. Cousinou²², B.E. Cox²¹, G. Cozzika⁹, J. Cvach²⁹, J.B. Dainton¹⁸, W.D. Dau¹⁵, K. Daum^{33,39}, M. Davidsson²⁰, B. Delcourt²⁶, N. Delerue²², R. Demirchyan³⁴, A. De Roeck^{10,43}, E.A. De Wolf⁴, C. Diaconu²², P. Dixon¹⁹, V. Dodonov¹², J.D. Dowell³, A. Drutskoi²³, C. Duprel², G. Eckerlin¹⁰, D. Eckstein³⁵, V. Efremenko²³, S. Egli³², R. Eichler³⁶, F. Eisele¹³, E. Eisenhandler¹⁹, M. Ellerbrock¹³, E. Elsen¹⁰, M. Erdmann^{10,40,e}, W. Erdmann³⁶, P.J.W. Faulkner³, L. Favart⁴, A. Fedotov²³, R. Felst¹⁰, J. Ferencei¹⁰, S. Ferron²⁷, M. Fleischer¹⁰, G. Flügge², A. Fomenko²⁴, I. Foresti³⁷, J. Formánek³⁰, J.M. Foster²¹, G. Franke¹⁰, E. Gabathuler¹⁸, K. Gabathuler³², J. Garvey³, J. Gassner³², J. Gayler¹⁰, R. Gerhards¹⁰, S. Ghazaryan³⁴, L. Goerlich⁶, N. Gogitidze²⁴, M. Goldberg²⁸, C. Goodwin³, C. Grab³⁶, H. Grässler², T. Greenshaw¹⁸, G. Grindhammer²⁵, T. Hadig¹, D. Haidt¹⁰, L. Hajduk⁶, W.J. Haynes⁵, B. Heinemann¹⁸, G. Heinzelmann¹¹, R.C.W. Henderson¹⁷, S. Hengstmann³⁷, H. Henschel³⁵, R. Heremans⁴, G. Herrera^{7,41}, I. Herynek²⁹, M. Hilgers³⁶, K.H. Hiller³⁵, J. Hladký²⁹, P. Höting², D. Hoffmann¹⁰, W. Hoprich¹², R. Horisberger³², S. Hurling¹⁰, M. Ibbotson²¹, Ç. İşsever⁷, M. Jacquet²⁶, M. Jaffre²⁶, L. Janauschek²⁵, D.M. Jansen¹², X. Janssen⁴, V. Jemanov¹¹, L. Jönsson²⁰, D.P. Johnson⁴, M.A.S. Jones¹⁸, H. Jung²⁰, H.K. Kästli³⁶, D. Kant¹⁹, M. Kapichine⁸, M. Karlsson²⁰, O. Karschnick¹¹, O. Kaufmann¹³, M. Kausch¹⁰, F. Keil¹⁴, N. Keller³⁷, J. Kennedy¹⁸, I.R. Kenyon³, S. Kermiche²², C. Kiesling²⁵, M. Klein³⁵, C. Kleinwort¹⁰, G. Knies¹⁰, B. Koblitz²⁵, S.D. Kolya²¹, V. Korbel¹⁰, P. Kostka³⁵, S.K. Kotelnikov²⁴, M.W. Krasny²⁸, H. Krehbiel¹⁰, J. Kroseberg³⁷, K. Krüger¹⁰, A. Küpper³³, T. Kuhr¹¹, T. Kurča^{35,16}, R. Kutuev¹², W. Lachnit¹⁰, R. Lahmann¹⁰, D. Lamb³, M.P.J. Landon¹⁹, W. Lange³⁵, T. Laštovička³⁰, E. Lebailly²⁶, A. Lebedev²⁴, B. Leibner¹, R. Lemrani¹⁰, V. Lendermann⁷, S. Levonian¹⁰, M. Lindstroem²⁰, E. Lobodzinska^{10,6}, B. Lobodzinski^{6,10}, N. Loktionova²⁴, V. Lubimov²³, S. Lüders³⁶, D. Lüke^{7,10}, L. Lytkin¹², N. Magnussen³³, H. Mahlke-Krüger¹⁰, N. Malden²¹, E. Malinovski²⁴, I. Malinovski²⁴, R. Maraček²⁵,

P. Marage⁴, J. Marks¹³, R. Marshall²¹, H.-U. Martyn¹, J. Martyniak⁶, S.J. Maxfield¹⁸, A. Mehta¹⁸, K. Meier¹⁴, P. Merkel¹⁰, F. Metlica¹², H. Meyer³³, J. Meyer¹⁰, P.-O. Meyer², S. Mikocki⁶, D. Milstead¹⁸, T. Mkrtchyan³⁴, R. Mohr²⁵, S. Mohrdieck¹¹, M.N. Mondragon⁷, F. Moreau²⁷, A. Morozov⁸, J.V. Morris⁵, K. Müller¹³, P. Murín^{16,42}, V. Nagovizin²³, B. Naroska¹¹, J. Naumann⁷, Th. Naumann³⁵, G. Nellen²⁵, P.R. Newman³, T.C. Nicholls⁵, F. Niebergall¹¹, C. Niebuhr¹⁰, O. Nix¹⁴, G. Nowak⁶, T. Nunnemann¹², J.E. Olsson¹⁰, D. Ozerov²³, V. Panassik⁸, C. Pascaud²⁶, G.D. Patel¹⁸, E. Perez⁹, J.P. Phillips¹⁸, D. Pitzl¹⁰, R. Pöschl⁷, I. Potachnikova¹², B. Povh¹², K. Rabbertz¹, G. Rädcl⁹, J. Rauschenberger¹¹, P. Reimer²⁹, B. Reisert²⁵, D. Reyna¹⁰, S. Riess¹¹, E. Rizvi³, P. Robmann³⁷, R. Roosen⁴, A. Rostovtsev²³, C. Royon⁹, S. Rusakov²⁴, K. Rybicki⁶, D.P.C. Sankey⁵, J. Scheins¹, F.-P. Schilling¹³, P. Schleper¹³, D. Schmidt³³, D. Schmidt¹⁰, S. Schmitt¹⁰, L. Schoeffel⁹, A. Schöning³⁶, T. Schörner²⁵, V. Schröder¹⁰, H.-C. Schultz-Coulon¹⁰, K. Sedlák²⁹, F. Sefkow³⁷, V. Shekelyan²⁵, I. Sheviakov²⁴, L.N. Shtarkov²⁴, G. Siegmon¹⁵, P. Sievers¹³, Y. Sirois²⁷, T. Sloan¹⁷, P. Smirnov²⁴, V. Solochenko²³, Y. Soloviev²⁴, V. Spaskov⁸, A. Specka²⁷, H. Spitzer¹¹, R. Stamen⁷, J. Steinhart¹¹, B. Stella³¹, A. Stellberger¹⁴, J. Stiewe¹⁴, U. Straumann³⁷, W. Struczinski², M. Swart¹⁴, M. Taševský²⁹, V. Tchernyshov²³, S. Tchetchelnitski²³, G. Thompson¹⁹, P.D. Thompson³, N. Tobien¹⁰, D. Traynor¹⁹, P. Truöl³⁷, G. Tsipolitis³⁶, J. Turnau⁶, J.E. Turney¹⁹, E. Tzamariudaki²⁵, S. Udluft²⁵, A. Usik²⁴, S. Valkár³⁰, A. Valkárová³⁰, C. Vallée²², P. Van Mechelen⁴, Y. Vazdik²⁴, S. von Dombrowski³⁷, K. Wacker⁷, R. Wallny³⁷, T. Walter³⁷, B. Waugh²¹, G. Weber¹¹, M. Weber¹⁴, D. Wegener⁷, A. Wegner²⁵, T. Wengler¹³, M. Werner¹³, G. White¹⁷, S. Wiesand³³, T. Wilksen¹⁰, M. Winde³⁵, G.-G. Winter¹⁰, C. Wissing⁷, M. Wobisch², H. Wollatz¹⁰, E. Wünsch¹⁰, A.C. Wyatt²¹, J. Žáček³⁰, J. Zálešák³⁰, Z. Zhang²⁶, A. Zhokin²³, F. Zomer²⁶, J. Zsembery⁹ and M. zur Nedden¹⁰

³² Paul Scherrer Institut, Villigen

³⁶ Institut für Teilchenphysik, ETH, Zürich

³⁷ Physik-Institut der Universität Zürich, Zürich